ECOLE POLYTECHNIQUE

CENTRE DE MATHÉMATIQUES APPLIQUÉES

UMR CNRS 7641

91128 PALAISEAU CEDEX (FRANCE). Tél: 01 69 33 41 50. Fax: 01 69 33 30 11
http://www.cmap.polytechnique.fr/

Numerical Localizations of 3D Imperfections from an Asymptotic Formula for Perturbations in the Electric Fields

M. Asch and S.M. Mefire

R.I. 606 *December 2006*

Numerical Localizations of 3D Imperfections from an Asymptotic Formula for Perturbations in the Electric Fields *

M. Asch [1] **and S.M. Mefire** [2]

[1] LAMFA, Université de Picardie, CNRS,
33, rue Saint-Leu, 80039 Amiens, France.

[2] CMAP, Ecole Polytechnique, CNRS,
Route de Saclay, 91128 Palaiseau, France.

Contents

*This work was partly supported by ACI NIM (171) from the French Ministry of Education and Scientific Research.

Abstract. This work deals with the numerical localization of small electromagnetic inhomogeneities. The underlying inverse problem considers, in a three-dimensional bounded domain, the time-harmonic Maxwell equations formulated in electric field. Typically, the domain contains a finite number of unknown inhomogeneities of small volume and the inverse problem attempts to localize these inhomogeneities from a finite number of boundary measurements. Our localization approach is based on a framework, recently introduced, that proposes the use of an asymptotic expansion for the perturbations in the tangential boundary trace of the curl of the electric field. We present three numerical localization procedures resulting from the combination of this asymptotic expansion with each of the following inversion algorithms: the Current Projection method, the MUltiple SIgnal Classification (MUSIC) algorithm, and an inverse Fourier method. We perform a numerical study of the asymptotic expansion and compare the numerical results obtained from the three localization procedures in different settings.

Keywords. inverse problems, Maxwell equations, electric fields, three-dimensional inhomogeneities, Electrical Impedance Tomography, Current Projection method, MUSIC algorithm, FFT, edge elements, numerical boundary measurements

MS Codes. 35R30, 65N21, 65N30, 78A25

1 Introduction

The localization of inhomogeneities contained in a bounded domain is of great importance since it has several practical applications: identification of cancer tumors, detection of anti-personnel mines, localization of cracks, ... Usually, when we seek to localize an inhomogeneity contained in a domain, we are concerned with an inverse problem for retrieving the geometry of the inhomogeneity or for imaging the physical parameter that characterizes the heterogeneity of the domain.

Recently, several works have been devoted to the numerical analysis of the localization of inhomogeneities (cf. e.g. [3], [5], [6], [10], [24]), in particular in the field of Electrical Impedance Tomography. The localization model proposed by D.J. Cedio-Fengya, S. Moskow & M.S. Vogelius [10] consists of identifying inhomogeneities of small volume by combining an asymptotic formula with an inversion algorithm. Typically, in [10], the conductivity problem is set in a bounded domain containing a finite number of unknown inhomogeneities of small volume. The inversion algorithm makes use of the asymptotic formula (for perturbations in the voltage potential), and is based on a minimization procedure of least-squares type for the calculation of the geometrical parameters of the inhomogeneities (namely the centers and diameters when these are balls for example). Another reconstruction approach of these small conductivity inhomogeneities, also based on a nonlinear minimization procedure, is the one that consists of imaging the electric conductivity in the domain (cf. e.g. [3]). Regarding the same conductivity problem, H. Ammari, S. Moskow & M.S. Vogelius proposed in [5] a localization process of small inhomogeneities, where the asymptotic formula of [10] is considered for measuring boundary voltage perturbations initiated by electric currents applied on the boundary of the domain. Limited current-to-voltage pairs on the boundary are then used as data of the inversion algorithm which consists, here, of solving a linear system for locating a single inhomogeneity, or of calculating a discrete inverse Fourier transform of a sample of measurements in the case of the localization of multiple inhomogeneities. The

inversion algorithm in [5] is then, in contrast to the one of [10], non-iterative and based on one of two linear methods: the Current Projection method (for locating a single inhomogeneity) or the inverse Fourier method (for locating multiple inhomogeneities).

D. Volkov formulates in [24] an algorithm based also on the inverse Fourier method for locating small dielectric inhomogeneities in a bi-dimensional bounded domain, from an asymptotic expansion (introduced elsewhere in [5]) for the study of the perturbations in the electric field satisfying the Helmholtz equation. The development of this algorithm is also described in [24] for the identification of three-dimensional dielectric inhomogeneities of small volume, from the far field pattern at a fixed frequency.

In the context of localization in an unbounded domain, H. Ammari, E. Iakovleva & D. Lesselier have developed in [1] an algorithm for locating small bi-dimensional inclusions buried in a half-space from the scattering amplitude at a fixed frequency. In [1], the continuous problem is set with the help of the bi-dimensional Helmholtz equation, an asymptotic expansion of the scattering amplitude is presented, and the inversion algorithm is essentially a method for characterizing the range of a self-adjoint operator. This is a linear method, called MUSIC (MUltiple SIgnal Classification), generally used in signal processing theory, and known for estimating the individual frequencies of multiple-harmonic signals [23].

We refer to [3], [4], [8], [12], [14], [17], [19], [21], [22] for other numerical methods, as well as for tools, aimed at solving the reconstruction problem of conductivity inhomogeneities, elastic inhomogeneities, and dielectric inhomogeneities, in different settings.

More recently, H. Ammari, M.S. Vogelius & D. Volkov [6] have introduced a framework for the localization of *three-dimensional electromagnetic* inhomogeneities. This framework considers the time-harmonic Maxwell equations in a three-dimensional bounded domain Ω containing a finite number m of unknown inhomogeneities of small volume, and proposes to localize these inhomogeneities from an asymptotic expansion of the perturbation in the (tangential) boundary magnetic field. In the presence of well-separated inhomogeneities, and also distant from $\partial\Omega$, the boundary of Ω, the asymptotic expansion states that, for any $z \in \partial\Omega$,

$$\begin{aligned}(H_\alpha - H_0)(z) \times \nu(z) \,-\, 2\int_{\partial\Omega} \mathrm{curl}_z(\Phi^k(x,z)(H_\alpha - H_0)(x) \times \nu(x)) \times \nu(z)\, d\sigma_x \\ =\; 2\alpha^3\omega^2 \sum_{j=1}^{m} \frac{\mu_0}{\mu_j}(\mu_0 - \mu_j) G(z_j, z) \times \nu(z) M^j(\tfrac{\mu_0}{\mu_j}) H_0(z_j) \\ + 2\alpha^3 \sum_{j=1}^{m} (\frac{1}{\varepsilon_j} - \frac{1}{\varepsilon_0})((\mathrm{curl}_x\, G)(z_j, z))^T \times \nu(z) M^j(\tfrac{\varepsilon_0}{\varepsilon_j})(\mathrm{curl}_x\, H_0)(z_j) + \mathrm{O}(\alpha^4)\,.\end{aligned} \tag{1}$$

In (1), α is the common order of magnitude of the diameters of the inhomogeneities, and the points z_j, $1 \le j \le m$, represent the 'centers' of the inhomogeneities. The magnetic field is denoted by H_α in the presence of the inhomogeneities and by H_0 in the absence of any inhomogeneities. The outward unit normal to Ω is represented by ν, and ω is a given frequency. The (constant) background magnetic

permeability and complex permittivity are μ_0 and ε_0 respectively. Also, μ_j and ε_j are the (constant) magnetic permeability and the complex permittivity of the jth inhomogeneity, $k^2 = \omega^2\varepsilon_0\mu_0$, Φ^k is the "free space" Green's function for the Helmholtz operator $\Delta + k^2$. The operators applied to the matrix valued function G act column-by-column, and $G(x,z)$ is the "free space" Green's function for the "background" magnetic problem: $\mathrm{curl}_x\,(\frac{1}{\varepsilon_0}\,\mathrm{curl}_x G(x,z)) - \omega^2\mu_0 G(x,z) = -\delta_z I_3$, with I_3 the 3×3 identity matrix, δ_z the Dirac mass at z. Also in (1), the superscript "T" denotes the transpose, $M^j(\frac{\mu_0}{\mu_j})$ and $M^j(\frac{\varepsilon_0}{\varepsilon_j})$ are the polarization tensors associated with the jth inhomogeneity (symmetric 3×3 matrices). Finally, the notation $\mathrm{O}(\alpha^4)$ means a term that goes to zero like α^4, uniformly in z.

It is already important to mention that in contrast to the large variety and extensive list of papers devoted to the bi-dimensional numerical localization, we do not find in the literature a similar range of references for the three-dimensional numerical localization. Also, in the field of Electrical Impedance Tomography (EIT), where one seeks to recover the unknown inhomogeneities contained in a body from measurements on the body's surface, most references concerned with numerical localization make use of synthetic data (by adding or not random noises) instead of these measurements. We think that the best way to numerically validate a localization procedure, and to check its robustness, consists of using numerical data — each datum corresponds actually to the numerical approximation of a measurement on the body's surface. Our approach will be oriented in this direction.

In this paper, we deal with the numerical localization of electromagnetic inhomogeneities of small volume. We are concerned with an inverse problem that considers, in a three-dimensional bounded domain Ω, the time-harmonic Maxwell equations formulated in electric field. In fact, Ω contains a finite number m of unknown inhomogeneities and the inverse problem consists of localizing numerically these inhomogeneities from a finite number of boundary measurements. This work falls directly in the field of EIT. An underlying application could concern so called "eddy current methods", which are now frequently used for corrosion and other metal defect inspections. A particularly challenging practical application would be the identification of anti-personnel- and other types of mines. In this kind of application it is often not necessary to reconstruct the precise values of the electromagnetic parameters of the inhomogeneities or their shapes, since we are primarily interested in their positions in Ω. Our localization approach will mainly consist of locating the 'centers' of the inhomogeneities and in some situations, when $m = 1$, of providing the center and the diameter of the inhomogeneity at a fixed frequency ω.

The framework developed in [6] is the basis of this localization approach, and we are now concerned with an analogous asymptotic expansion to (1) devoted to the study of perturbations in the tangential boundary trace of the curl of the *electric field* due to the presence of inhomogeneities in Ω. A particular reformulation of this asymptotic expansion leads to an asymptotic formula that allows us to compute boundary measurements of "voltage" type from prescribed boundary currents. The localization approach presented here is a combination of this asymptotic formula and of a suited inversion algorithm since the measurements generated from the formula are used as data of the algorithm aimed at locating

the inhomogeneities. From a practical point of view, these data are experimental measurements and from a simulation point of view, they are numerically computed boundary measurements.

This work is organized in seven sections. In Section 2, we introduce some notation and describe, with the help of the time-harmonic Maxwell equations, the "background" problem in electric field as well as the problem in electric field in the presence of inhomogeneities in Ω. In Section 3, the weak formulations of these problems in electric field are introduced and the asymptotic expansion for the perturbations in the tangential boundary trace of the curl of the electric field is considered. The asymptotic formula for generating boundary measurements of "voltage" type is also presented here. We are interested in Section 4 in a conforming mixed finite element discretization of the weak formulation associated with the problem in electric field in the presence of inhomogeneities. The considered discrete formulation uses Nédélec's edge elements and allows us to compute the electric field, initiated by a boundary current, for evaluating numerically the corresponding boundary measurement. Since a finite number of numerical boundary measurements is needed in the inversion procedure, the (direct) computation of the discrete electric field will be required a finite number of times, and consequently, a finite number of boundary currents will be applied. In Section 5, we describe three inversion algorithms that will be used distinctly in the numerical simulations: the Current Projection method, the MUSIC algorithm and the inverse Fourier method. In association with the asymptotic formula that allows us to generate boundary measurements, each one of these inversion algorithms defines a numerical localization procedure. Any one of the three numerical procedures can be employed for locating a single inhomogeneity, but only the two based on the MUSIC algorithm and the inverse Fourier method can be used for locating multiple inhomogeneities. Section 6 presents numerical results obtained from extensive simulations. Before describing the results concerning the numerical localization of inhomogeneities, we inspect numerically the asymptotic expansion for the perturbations in the tangential boundary trace of the curl of the electric field. This numerical inspection is performed in the case of a single inhomogeneity contained in the domain and with respect to the parameter $\tau = \alpha\omega$, $\tau < 1$, that links the order of magnitude of the diameter of the inhomogeneity α and the frequency ω. We find that the aforementioned asymptotic expansion and consequently the asymptotic formula that allows us to compute the boundary measurements is numerically valid only within a restricted range of values of τ. In the case of multiple inhomogeneities contained in the domain, the same remark comes from numerical simulations of their localization: in order to achieve accurate localizations, the asymptotic formula for the computation of boundary measurements must also be considered here within a restricted range of values of τ, where α represents now the common order of magnitude of the diameters of the inhomogeneities. The numerical results obtained with each one of the three localization procedures in different settings are described in this section. We are thus concerned with a numerical comparison of the results of the three procedures when Ω contains a single inhomogeneity and with a comparison of the results for the two last procedures in the case of multiple inhomogeneities. Finally, some conclusions and perspectives are reported in Section 7.

2 Some Notation and the Problem in Electric Field

2.1 Some Notation

Let us consider a bounded open subset Ω of $\mathbb{R}^3$, with a smooth boundary $\partial\Omega$. For simplicity we take $\partial\Omega$ to be C^∞, but this regularity condition could be considerably weakened. The domain Ω contains here a finite number m of inhomogeneities, each one of the form $z_j+\alpha B_j$, where $B_j \subset \mathbb{R}^3$ is a bounded, smooth (C^∞) domain containing the origin. The total collection of inhomogeneities thus takes the form $I_\alpha = \bigcup_{j=1}^{m}(z_j+\alpha B_j)$. The points $z_j \in \Omega$, $1 \le j \le m$, that determine the locations of the inhomogeneities are assumed to satisfy:

$$\begin{cases} 0 < d_0 \le |z_j - z_k| & \forall\, j \neq k, \\ 0 < d_0 \le \operatorname{dist}(z_j, \partial\Omega) & \forall\, j\,. \end{cases} \tag{2}$$

The parameter $\alpha > 0$, the common order of magnitude of the diameters of the inhomogeneities, is sufficiently small in such a way that these inhomogeneities are disjoint and their distance to $\mathbb{R}^3 \setminus \Omega$ is larger than $d_0/2$. As a consequence of the assumption (2), it follows that: $m \le 6|\Omega|/\pi d_0^3$.

Hereafter, we call each one of these small inhomogeneities, an *imperfection*.

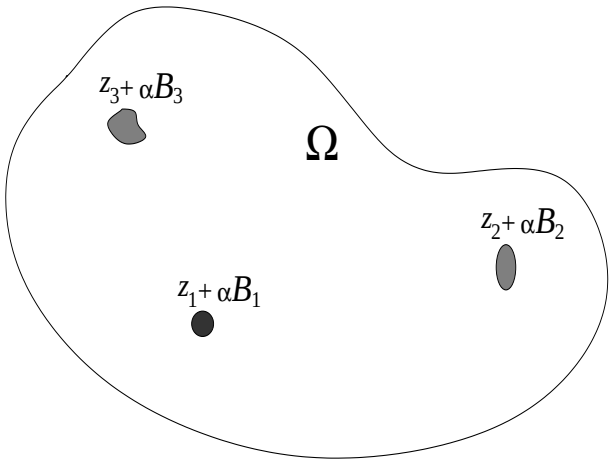

Figure 1: An example of a domain containing imperfections.

2.2 Problem in Electric Field

If we denote by μ the magnetic permeability and by $\varepsilon^{\rm re}$ the (real) electric permittivity of the domain Ω containing different materials, the time-dependent linear Maxwell equations in Ω take the form: $\forall\, x \in \Omega$, $t > 0$,

$$\operatorname{curl}\mathbf{E}(x,t) \;=\; -\mu(x)\frac{\partial \mathbf{H}}{\partial t}(x,t)\,, \quad \operatorname{curl}\mathbf{H}(x,t) \;=\; \mathbf{J_f}(x,t) + \varepsilon^{\rm re}(x)\frac{\partial \mathbf{E}}{\partial t}(x,t)\,,$$

where $\mathbf{E} \in \mathbb{R}^3$ is the electric field, and $\mathbf{H} \in \mathbb{R}^3$ is the magnetic field. In these equations, $\mathbf{J_f}$ is the free current related to the field $\mathbf{E}$ by $\mathbf{J_f} = \sigma\mathbf{E}$, where σ represents the conductivity of the medium.

When we study the time-harmonic solutions to these equations, we consider special solutions of the form

$$\mathbf{E}(x,t) \,=\, \mathrm{Re}\{E(x)\mathrm{e}^{-\mathrm{i}\omega t}\} \quad \text{and} \quad \mathbf{H}(x,t) \,=\, \mathrm{Re}\{H(x)\mathrm{e}^{-\mathrm{i}\omega t}\}\,, \quad x \in \Omega,\; t > 0,$$

where $\omega > 0$ denotes the given frequency, and the $\mathbb{C}^3$-valued fields E, H are such that: $\forall\, x \in \Omega$,

$$\mathrm{curl}\, E(x) \;=\; \mathrm{i}\omega\mu(x)H(x)\,, \quad \mathrm{curl}\, H(x) \;=\; -\mathrm{i}\omega\varepsilon(x)E(x)\,. \tag{3}$$

Here, $\varepsilon(x) = \varepsilon^{\mathrm{re}}(x) + \mathrm{i}\frac{\sigma(x)}{\omega}$ represents the complex permittivity. By dividing the first equation of (3) by μ and taking the curl, we obtain the following equation for E:

$$\mathrm{curl}(\frac{1}{\mu}\,\mathrm{curl}\, E) \,-\, \omega^2\varepsilon E \,=\, 0 \quad \text{in} \quad \Omega\,. \tag{4}$$

We shall prescribe non-trivial boundary conditions for $E \times \nu$, on the boundary $\partial\Omega$, in order to arrive at particular non-trivial solutions to (3). The outward unit normal to Ω is denoted by ν.

Let $\mu_0 > 0$, $\varepsilon_0^{\mathrm{re}} > 0$, and $\sigma_0 \geq 0$ denote the permeability, the (real) permittivity, and the conductivity of the background medium, with $\varepsilon_0 = \varepsilon_0^{\mathrm{re}} + \mathrm{i}\frac{\sigma_0}{\omega}$ the background complex permittivity. Let also $\mu_j > 0$, $\varepsilon_j^{\mathrm{re}} > 0$, $\sigma_j \geq 0$ and $\varepsilon_j = \varepsilon_j^{\mathrm{re}} + \mathrm{i}\frac{\sigma_j}{\omega}$ denote the permeability, the (real) permittivity, the conductivity, and the complex permittivity of the jth imperfection $z_j + \alpha B_j$. For simplicity, we shall assume here that all these parameters are constants. Introduce thus the piecewise constant magnetic permeability μ_α and the piecewise constant complex permittivity ε_α: $\forall\, x \in \Omega$,

$$\mu_\alpha(x) \;=\; \begin{cases} \mu_0, & \text{if} \quad x \in \Omega \setminus \overline{I_\alpha}\,, \\ \mu_j, & \text{if} \quad x \in z_j + \alpha B_j,\;\; 1 \leq j \leq m\,, \end{cases} \qquad \varepsilon_\alpha(x) \;=\; \begin{cases} \varepsilon_0, & \text{if} \quad x \in \Omega \setminus \overline{I_\alpha}\,, \\ \varepsilon_j, & \text{if} \quad x \in z_j + \alpha B_j,\;\; 1 \leq j \leq m\,. \end{cases}$$

If we allow the degenerate case $\alpha = 0$, then the function $\mu_\alpha(x)$ equals the constant μ_0 and the function $\varepsilon(x)$ equals the constant ε_0.

The electric field denoted E_α, in the presence of imperfections, is the solution to:

$$\begin{cases} \mathrm{curl}(\frac{1}{\mu_\alpha}\,\mathrm{curl}\, E_\alpha) - \omega^2\varepsilon_\alpha E_\alpha \;=\; 0 \quad \text{in} \quad \Omega\,, \\ \qquad\qquad\qquad\qquad E_\alpha \times \nu \;=\; g \quad \text{on} \quad \partial\Omega\,, \end{cases} \tag{5}$$

with g a given datum on $\partial\Omega$. When the outward unit normal to $\partial(z_j + \alpha B_j)$, the boundary of $z_j + \alpha B_j$, is also denoted by ν, and the superscripts $+$, $-$ indicate the limiting values as $\partial(z_j + \alpha B_j)$ is approached from outside $z_j + \alpha B_j$ and from inside $z_j + \alpha B_j$ respectively, the equations of (5) can be reformulated as follows:

$$\begin{cases} \mathrm{curl}(\frac{1}{\mu_0}\,\mathrm{curl}\, E_\alpha) - \omega^2\varepsilon_0 E_\alpha \;=\; 0 \quad \text{in} \quad \Omega \setminus \overline{I_\alpha}\,, \\ \mathrm{curl}(\frac{1}{\mu_j}\,\mathrm{curl}\, E_\alpha) - \omega^2\varepsilon_j E_\alpha \;=\; 0 \quad \text{in} \quad z_j + \alpha B_j, \qquad \text{for} \quad 1 \leq j \leq m\,, \\ E_\alpha^+ \times \nu - E_\alpha^- \times \nu \;=\; 0 \quad \text{on} \quad \partial(z_j + \alpha B_j), \quad \text{for} \quad 1 \leq j \leq m\,, \\ \frac{1}{\mu_0}(\mathrm{curl}\, E_\alpha)^+ \times \nu - \frac{1}{\mu_j}(\mathrm{curl}\, E_\alpha)^- \times \nu \;=\; 0 \quad \text{on} \quad \partial(z_j + \alpha B_j), \quad \text{for} \quad 1 \leq j \leq m\,, \\ \varepsilon_0 E_\alpha^+ \cdot \nu - \varepsilon_j E_\alpha^- \cdot \nu \;=\; 0 \quad \text{on} \quad \partial(z_j + \alpha B_j), \quad \text{for} \quad 1 \leq j \leq m\,, \\ E_\alpha \times \nu \;=\; g \quad \text{on} \quad \partial\Omega\,. \end{cases}$$

The electric field denoted E_0, in the absence of all imperfections, satisfies:

$$\left\{\begin{array}{rcl} \operatorname{curl}(\frac{1}{\mu_0}\operatorname{curl} E_0) - \omega^2\varepsilon_0 E_0 &=& 0 \quad \text{in} \quad \Omega\,, \\ E_0 \times \nu &=& g \quad \text{on} \quad \partial\Omega\,. \end{array}\right. \tag{6}$$

3 Formulation in Electric Field and Asymptotic Formula for Perturbations in the Electric Field

We consider in this section the weak problems associated with (5) and (6) respectively, and an asymptotic formula for perturbations in the electric field in the presence of imperfections.

3.1 Formulation in Electric Field

Let

$$H(\operatorname{curl};\,\Omega) \,=\, \{u \in (L^2(\Omega))^3\,;\, \operatorname{curl} u \in (L^2(\Omega))^3\,\}$$

be endowed with its usual Hermitian product denoted here by $(\,.\,,\,.\,)_{H(\operatorname{curl};\,\Omega)}$; the corresponding norm is denoted by $\|\,.\,\|_{H(\operatorname{curl};\,\Omega)}$. By representing the surface divergence by $\operatorname{div}_{\partial\Omega}$, let us consider the space

$$TH^{-\frac{1}{2}}(\operatorname{div};\,\partial\Omega) \,=\, \{q \in (H^{-\frac{1}{2}}(\partial\Omega))^3\,;\, \operatorname{div}_{\partial\Omega} q \in H^{-\frac{1}{2}}(\partial\Omega),\; q\cdot\nu = 0 \;\text{ on }\; \partial\Omega\},$$

with its usual norm denoted here by $\|\,.\,\|_{TH^{-\frac{1}{2}}(\operatorname{div};\,\partial\Omega)}$.

The vector fields E_α and E_0, satisfying (5) and (6) respectively, will be sought in $H(\operatorname{curl};\,\Omega)$, and the datum g will be taken in $TH^{-\frac{1}{2}}(\operatorname{div};\,\partial\Omega)$. For such a datum g, let us consider $u_g \in H(\operatorname{curl};\,\Omega)$ such that (see e.g. [7]):

$$\left\{\begin{array}{rcl} u_g \times \nu &=& g \quad \text{on} \quad \partial\Omega\,, \\ \|u_g\|_{H(\operatorname{curl};\,\Omega)} &\leq& C_\Omega \|g\|_{TH^{-\frac{1}{2}}(\operatorname{div};\,\partial\Omega)}\,, \end{array}\right. \tag{7}$$

where $C_\Omega > 0$ is a constant depending only on Ω. With the extension field u_g, the determination of the vector field E_α satisfying (5) is reduced to the problem that consists of finding $\mathcal{E}_\alpha$ such that:

$$\left\{\begin{array}{rcll} \operatorname{curl}(\frac{1}{\mu_\alpha}\operatorname{curl}\mathcal{E}_\alpha) - \omega^2\varepsilon_\alpha\mathcal{E}_\alpha &=& -\operatorname{curl}(\frac{1}{\mu_\alpha}\operatorname{curl} u_g) + \omega^2\varepsilon_\alpha u_g & \text{in} \quad \Omega\,, \\ \mathcal{E}_\alpha \times \nu &=& 0 & \text{on} \quad \partial\Omega\,. \end{array}\right. \tag{8}$$

Also with the same extension field, the determination of E_0 satisfying (6) is reduced to the one that consists of finding $\mathcal{E}_0$ such that:

$$\left\{\begin{array}{rcll} \operatorname{curl}(\frac{1}{\mu_0}\operatorname{curl}\mathcal{E}_0) - \omega^2\varepsilon_0\mathcal{E}_0 &=& -\operatorname{curl}(\frac{1}{\mu_0}\operatorname{curl} u_g) + \omega^2\varepsilon_0 u_g & \text{in} \quad \Omega\,, \\ \mathcal{E}_0 \times \nu &=& 0 & \text{on} \quad \partial\Omega\,. \end{array}\right. \tag{9}$$

Of course, knowing u_g, while $\mathcal{E}_\alpha$ and $\mathcal{E}_0$ are in accordance with (8) and (9) respectively, we determine the physical fields:

$$E_\alpha \,:=\, \mathcal{E}_\alpha + u_g\,, \quad E_0 \,:=\, \mathcal{E}_0 + u_g\,. \tag{10}$$

These vector fields $\mathcal{E}_\alpha$ and $\mathcal{E}_0$ will be sought in

$$\mathcal{H} \,=\, \{u \in H(\mathrm{curl};\, \Omega)\,;\; u \times \nu = 0 \;\text{ on }\; \partial\Omega\,\}\,.$$

For g given in $TH^{-\frac{1}{2}}(\mathrm{div}\,;\, \partial\Omega)$, and therefore u_g taken as in (7), the weak formulation associated with (9) consists of finding $\mathcal{E}_0 \in \mathcal{H}$ such that:

$$\begin{array}{c} \int_\Omega \frac{1}{\mu_0}\,\mathrm{curl}\,\mathcal{E}_0 \cdot \overline{\mathrm{curl}\,v}\,dx - \omega^2 \int_\Omega \varepsilon_0 \mathcal{E}_0 \cdot \overline{v}\,dx \,= \\ -\int_\Omega \frac{1}{\mu_0}\,\mathrm{curl}\,u_g \cdot \overline{\mathrm{curl}\,v}\,dx + \omega^2 \int_\Omega \varepsilon_0 u_g \cdot \overline{v}\,dx \;\;\forall\, v \in \mathcal{H}\,. \end{array} \tag{11}$$

The weak formulation associated with (8) is defined in the same way.

Find $\mathcal{E}_\alpha \in \mathcal{H}$ satisfying:

$$\begin{array}{c} \int_\Omega \frac{1}{\mu_\alpha}\,\mathrm{curl}\,\mathcal{E}_\alpha \cdot \overline{\mathrm{curl}\,v}\,dx - \omega^2 \int_\Omega \varepsilon_\alpha \mathcal{E}_\alpha \cdot \overline{v}\,dx \,= \\ -\int_\Omega \frac{1}{\mu_\alpha}\,\mathrm{curl}\,u_g \cdot \overline{\mathrm{curl}\,v}\,dx + \omega^2 \int_\Omega \varepsilon_\alpha u_g \cdot \overline{v}\,dx \;\;\forall\, v \in \mathcal{H}\,. \end{array} \tag{12}$$

Remark 3.1 *In the present framework, the essential hypothesis is that:* $k^2 = \omega^2\mu_0\varepsilon_0$ *is taken such that* (11) *has a unique solution.*

The existence and uniqueness of the solution of (12) will be specified in the next subsection (see Theorem 3.1).

3.2 Asymptotic Formula for Perturbations in the Electric Field

We consider in this part an asymptotic formula introduced by H. Ammari, M.S. Vogelius & D. Volkov [6] for the study of perturbations in the electric field due to the presence of imperfections. Let us first introduce some additional notation and definitions.

Let $\{\gamma_n\}_{0\le n\le m}$ be a set of complex constants with $\mathrm{Re}(\gamma_n) > 0$, for $0 \le n \le m$. Typically, $\{\gamma_n\}_{0\le n\le m}$ will be related to either the set $\{\mu_n\}_{0\le n\le m}$ or the set $\{\varepsilon_n\}_{0\le n\le m}$. For any fixed $1 \le j_0 \le m$, let γ denote the function defined as: $\forall\, x \in \mathbb{R}^3$,

$$\gamma(x) \;=\; \begin{cases} \gamma_0, & \text{if} \quad x \in \mathbb{R}^3 \setminus \overline{B_{j_0}}\,, \\ \gamma_{j_0}, & \text{if} \quad x \in B_{j_0}\,. \end{cases}$$

Let $1 \le l \le 3$. We denote by ϕ_l the solution to the problem:

$$\begin{cases} \mathrm{div}\,(\gamma(x)\;\mathrm{grad}\,\phi_l(x)) \;=\; 0 \quad \text{for} \quad x \in \mathbb{R}^3\,, \\ \qquad\qquad\qquad \phi_l(x) - x_l \to 0 \quad \text{as} \quad |x| \to \infty\,. \end{cases}$$

As mentioned in [6], the existence and uniqueness of ϕ_l can be established (in the real as well as in the complex case) by using single layer potentials with suitably chosen densities ([13], [15]). When the outward unit normal to ∂B_{j_0}, the boundary of B_{j_0}, is also denoted by ν, and the superscripts $+$, $-$

indicate the limiting values as ∂B_{j_0} is approached from outside B_{j_0}, and from inside B_{j_0} respectively, this problem in scalar potential may also be reformulated as follows:

$$\left\{\begin{array}{rcll} \mathrm{div}\,(\gamma_0\,\mathrm{grad}\,\phi_l) &=& 0 & \text{in} \quad \mathbb{R}^3 \setminus \overline{B_{j_0}}\,, \\ \mathrm{div}\,(\gamma_{j_0}\,\mathrm{grad}\,\phi_l) &=& 0 & \text{in} \quad B_{j_0}\,, \\ \phi_l^+ - \phi_l^- &=& 0 & \text{on} \quad \partial B_{j_0}\,, \\ \frac{\gamma_0}{\gamma_{j_0}}(\frac{\partial \phi_l}{\partial \nu})^+ - (\frac{\partial \phi_l}{\partial \nu})^- &=& 0 & \text{on} \quad \partial B_{j_0}\,, \\ \phi_l(x) - x_l \to 0 & & & \text{as} \quad |x| \to \infty\,. \end{array}\right. \tag{13}$$

The function ϕ_l depends thus only on γ_0 and γ_{j_0} through the ratio $c = \frac{\gamma_0}{\gamma_{j_0}}$. Here, the essential assumption is that the constant c cannot be zero or a negative real number. With this aspect ratio, we define (as in [6]) the polarization tensor, $M^{j_0}(c)$, of the inhomogeneity B_{j_0} as follows: $\forall\ 1 \leq i, l \leq 3$,

$$M_{il}^{j_0}(c) \;=\; c^{-1} \int_{B_{j_0}} \frac{\partial \phi_l}{\partial x_i}\, dx\,. \tag{14}$$

Following [6], the tensor $M^{j_0}(c)$ is symmetric, and is furthermore positive definite if $c \in \mathbb{R}_+^\star$.

Remark 3.2 *In the case where B_{j_0} is a ball, its polarization tensor M^{j_0} is analytically known (see e.g. [16]):*

$$M^{j_0}(c) \;=\; \frac{3}{2c+1}\,\mathrm{vol}(B_{j_0})I_3\,,$$

where I_3 is the 3×3 identity matrix.

Let us introduce, for $x \neq z \in \mathbb{R}^3$, the scalar function

$$\Phi^k(x,z) \;=\; \frac{\mathrm{e}^{\mathrm{i}k|x-z|}}{4\pi|x-z|}\,,$$

with the constant k defined as in Remark 3.1. Of course, Φ^k is a "free space" Green's function for the Helmholtz operator $\Delta + k^2$, i.e., it satisfies:

$$(\Delta + k^2)\Phi^k(\cdot, z) \;=\; -\delta_z \quad \text{in} \quad \mathbb{R}^3\,.$$

Let us now define the matrix valued function $G(x,z)$, for $x \neq z \in \mathbb{R}^3$, as

$$G(x,z) \;=\; -\mu_0(\Phi^k(x,z)\,I_3 + \frac{1}{k^2} D_x^2 \Phi^k(x,z))\,,$$

where D_x^2 denotes the Hessian, and $G(x,z)$ is a "free space" Green's function for the "background" electric problem:

$$\mathrm{curl}_x\,(\frac{1}{\mu_0}\,\mathrm{curl}_x\,G(x,z)) - \omega^2\epsilon_0 G(x,z) \;=\; -\delta_z I_3\,.$$

The operator curl_x applies here to matrices, column-by-column.

Let us now reconsider the physical fields E_α and E_0 defined through the vector fields $\mathcal{E}_\alpha$, $\mathcal{E}_0$ from (10). Although these vector fields, as well as u_g given in (7), have been defined only in a weak sense

on $\partial\Omega$, elliptic regularity results ensure that u_g, $\mathcal{E}_\alpha$, $\mathcal{E}_0$ are infinitely smooth vector fields (when g is infinitely smooth) and therefore the term $(\frac{1}{\mu_\alpha}\operatorname{curl} E_\alpha - \frac{1}{\mu_0}\operatorname{curl} E_0)|_{\partial\Omega}$ is infinitely smooth.

The framework of this paper is the main result proposed in [6]. We recall below this result which establishes an asymptotic formula allowing to study the perturbation $(\frac{1}{\mu_\alpha}\operatorname{curl} E_\alpha - \frac{1}{\mu_0}\operatorname{curl} E_0)\times\nu|_{\partial\Omega}$, in the tangential boundary trace of the curl of the electric field due to the presence of imperfections.

Theorem 3.1 *Let* (2) *be satisfied, and* $k^2 = \omega^2\mu_0\varepsilon_0$ *be taken such that* (11) *has a unique solution. There exists* $\alpha_0 > 0$ *such that, given an arbitrary* $g \in TH^{-\frac{1}{2}}(\operatorname{div}\,;\,\partial\Omega)$, *and any* $0 < \alpha < \alpha_0$, *the boundary value problem* (5) *has a unique (weak) solution. The constant* α_0 *depends on* $\{B_j\}_{1\le j\le m}$, Ω, $\{\mu_j\}_{0\le j\le m}$, $\{\varepsilon_j\}_{0\le j\le m}$, ω, *and* d_0, *but is otherwise independent of the points* z_j, $1 \le j \le m$. *Let* E_α *denote the unique (weak) solution to* (5), *and let* E_0 *be the unique (weak) solution to the boundary value problem* (6) *corresponding to the same* $g \in TH^{-\frac{1}{2}}(\operatorname{div}\,;\,\partial\Omega)$. *For any* $z \in \partial\Omega$, *we then have:*

$$
\begin{aligned}
&(\tfrac{1}{\mu_\alpha}\operatorname{curl} E_\alpha - \tfrac{1}{\mu_0}\operatorname{curl} E_0)(z)\times\nu(z)\\
-2\int_{\partial\Omega}&\operatorname{curl}_z(\Phi^k(x,z)(\tfrac{1}{\mu_\alpha}\operatorname{curl} E_\alpha - \tfrac{1}{\mu_0}\operatorname{curl} E_0)(x)\times\nu(x))\times\nu(z)\,d\sigma_x \;=\\
&2\alpha^3\omega^2\sum_{j=1}^{m}(\tfrac{\mu_0}{\mu_j}-1)G(z_j,z)\times\nu(z)M^j(\tfrac{\mu_0}{\mu_j})(\operatorname{curl} E_0)(z_j) +\\
&2\alpha^3\omega^2\varepsilon_0\sum_{j=1}^{m}(\tfrac{1}{\varepsilon_j}-\tfrac{1}{\varepsilon_0})((\operatorname{curl}_x G)(z_j,z))^T\times\nu(z)M^j(\tfrac{\varepsilon_0}{\varepsilon_j})E_0(z_j) + \mathrm{O}(\alpha^4)\,.
\end{aligned}
\tag{15}
$$

The term $\mathrm{O}(\alpha^4)$ *is bounded by* $C\,\alpha^4$, *uniformly in* z. *The positive constant* C *depends on* $\{B_j\}_{1\le j\le m}$, Ω, $\{\mu_j\}_{0\le j\le m}$, $\{\varepsilon_j\}_{0\le j\le m}$, ω, $\|g\|_{TH^{-\frac{1}{2}}(\operatorname{div}\,;\,\partial\Omega)}$, *and* d_0, *but is otherwise independent of the points* z_j, $1 \le j \le m$.

It can now be specified in particular that the consideration of k^2 such that the weak formulation (11) has a unique solution is also a hypothesis leading to the existence and uniqueness of the solution of the weak formulation (12).

In (15) and hereafter, the superscript "T" denotes the transpose. The following result is a consequence of Theorem 3.1 and is presented in [6] as a basis for some approximate inversion techniques.

Corollary 3.1 *Let us consider the assumptions of Theorem* 3.1, *and denote by* w *any smooth vector-valued function such that:*

$$
\operatorname{curl}(\operatorname{curl} w) - k^2 w \;=\; 0 \quad \textit{in} \quad W\,,
\tag{16}
$$

where W *is an open neighborhood of* Ω. *There exists a constant* $\alpha_0 > 0$ *depending on* $\{B_j\}_{1\le j\le m}$, Ω, $\{\mu_j\}_{0\le j\le m}$, $\{\varepsilon_j\}_{0\le j\le m}$, ω, *and* d_0, *but independent of* w, *of the points* z_j, $1 \le j \le m$, *and such that for a given* $g \in TH^{-\frac{1}{2}}(\operatorname{div}\,;\,\partial\Omega)$ *and any* $0 < \alpha < \alpha_0$, *the physical fields* E_α *and* E_0 *satisfy:*

$$
\begin{aligned}
\int_{\partial\Omega}&\operatorname{curl} E_\alpha\times\nu\cdot w\,d\sigma - \int_{\partial\Omega}\operatorname{curl} w\times\nu\cdot(\nu\times(E_\alpha\times\nu))\,d\sigma \;=\\
&\alpha^3\sum_{j=1}^{m}\omega^2\varepsilon_0\mu_0(\tfrac{\varepsilon_0}{\varepsilon_j}-1)\left[M^j(\tfrac{\varepsilon_0}{\varepsilon_j})E_0(z_j)\right]\cdot w(z_j) +\\
&\alpha^3\sum_{j=1}^{m}(\tfrac{\mu_0}{\mu_j}-1)\left[M^j(\tfrac{\mu_0}{\mu_j})\operatorname{curl} E_0(z_j)\right]\cdot\operatorname{curl} w(z_j) + \mathrm{O}(\alpha^4)\,.
\end{aligned}
\tag{17}
$$

This statement presents of course a version of the boundary perturbation in the curl of the electric field and appears well suited to applications since as we shall see in Section 5, it allows us, with the aid of inversion processes, to localize the imperfections from the consideration of some special test fields w.

4 Numerical Approximations

We are concerned in this part with the discretization of the formulation (12).

4.1 Introduction

For simplifying the presentation, we assume, in this section and in the following ones, that each imperfection present in the domain is a polyhedron. For the numerical localizations, we will use the asymptotic formula (17) and therefore the discrete field associated with the solution of the formulation (12). The discretization of this formulation is achieved with a finite element method based on a mesh obtained by a usual process of triangulation of the domain. Typically, the conforming finite element triangulation $\mathcal{T}_\alpha$ of the domain Ω is made up of tetrahedra in such a way that each inhomogeneity corresponds to a distinct collection of tetrahedra of $\mathcal{T}_\alpha$. More precisely, the collection of tetrahedra associated with an inhomogeneity covers entirely the geometry of the inhomogeneity. With such a conforming mesh of Ω, we are able to introduce a discrete formulation whose matrix assembly is easily performed by decomposing each heterogeneous integral term of the formulation into a sum of homogeneous integral terms.

For a tetrahedron K, let us denote by ϱ_K the diameter of the largest sphere included in K, and by h_K the diameter of K. The aspect-ratio of $\mathcal{T}_\alpha$ is defined as follows: $h_{\mathcal{T}_\alpha} = \sup_{K\in\mathcal{T}_\alpha} h_K$. Let us call $\{\mathcal{T}_\alpha^n\}_{n\geq 1}$ a sequence of triangulations of the domain Ω, where $\mathcal{T}_\alpha^n$ is described as $\mathcal{T}_\alpha$ above, for each n. As usual, we assume that this sequence is regular in the sense that there exists a constant $c > 0$ such that:

$$\forall\, n, \quad \sup_{K\in\mathcal{T}_\alpha^n} \frac{h_K}{\varrho_K} \leq c\,,$$

and moreover,

$$\lim_{n\longrightarrow\infty} h_{\mathcal{T}_\alpha^n} = 0\,.$$

It is important to notice the dependence of $h_{\mathcal{T}_\alpha^n}$ on α in the sense that we need to have a triangulation $\mathcal{T}_\alpha^n$ of Ω as fine as the triangulation of the smallest imperfection. In the sequel, we denote $\mathcal{T}_\alpha$ instead of $\mathcal{T}_\alpha^n$ and h instead of $h_{\mathcal{T}_\alpha^n}$ when no confusion is possible.

4.2 Discrete Formulation

Let P_d be the space of polynomials of degree less than or equal to d, and $\widetilde{P}_d$ be the space of homogeneous polynomials of degree d, with d a positive integer.

Consider the following vectorial subspaces (see Nédélec [20]):

$$S^1 = \{u \in (\widetilde{P}_1)^3 \,;\; u \cdot x = 0\}\,, \quad R^1 = (P_0)^3 \oplus S^1.$$

We associate with $\mathcal{H}$ the discrete space

$$\mathcal{H}_h \,=\, \{u_h \in H(\mathrm{curl};\,\Omega)\,;\; \mathrm{Re}(u_h)|_K, \mathrm{Im}(u_h)|_K \in R^1 \;\; \forall\, K \in \mathcal{T}_\alpha\,,\; u_h \times \nu = 0 \;\text{ on }\; \partial\Omega\}.$$

A vector field $\mathcal{E}_h$ of the space $\mathcal{H}_h$ is written in each tetrahedron K as (see e.g. [18]):

$$\mathcal{E}_h \,=\, \sum_{e=1}^{6} \mathcal{E}_h^e \,(\lambda_i \nabla\, \lambda_j - \lambda_j \nabla\, \lambda_i)\,, \tag{18}$$

where

- e is one of the six edges of K with vertices s^i, s^j,
- $\mathcal{E}_h^e$ is the degree of freedom associated with e,
- λ_i is the barycentric coordinate associated with the vertex s^i, and
- $\lambda_i \nabla\, \lambda_j - \lambda_j \nabla\, \lambda_i$ is the shape function associated with this edge e (oriented from s^i to s^j).

Typically, $\mathcal{H}_h$ is a Hilbert space when endowed with the norm of $\mathcal{H}$.

Let us now consider the discrete formulation associated with (12), defined as follows.

Find $\mathcal{E}_h \in \mathcal{H}_h$ such that:

$$\begin{array}{c} \int_\Omega \frac{1}{\mu_\alpha}\, \mathrm{curl}\, \mathcal{E}_h \cdot \overline{\mathrm{curl}\, v_h}\, dx - \omega^2 \int_\Omega \varepsilon_\alpha \mathcal{E}_h \cdot \overline{v_h}\, dx \;= \\ -\int_\Omega \frac{1}{\mu_\alpha}\, \mathrm{curl}\, u_g \cdot \overline{\mathrm{curl}\, v_h}\, dx + \omega^2 \int_\Omega \varepsilon_\alpha u_g \cdot \overline{v_h}\, dx \;\; \forall\, v_h \in \mathcal{H}_h\,. \end{array} \tag{19}$$

Due to the conforming finite element method applied here, the proof of the existence and uniqueness of the solution of (12), given in [6], implies also the existence and uniqueness of the solution of the associated discrete formulation (19).

5 Numerical Localization Procedures

We describe here three procedures for the localization of the imperfections. Each procedure results from the combination of the asymptotic formula (17) with one of the following inversion algorithms: the Current Projection method, the MUSIC algorithm, or an inverse Fourier method.

5.1 Current Projection Method

This is a localization method which can be used only in the case where the domain contains a single imperfection. Our aim in this case is to determine the center of the imperfection and to estimate its size. Let us first describe how we make use of the formula (17) in the present framework. If we denote by $p = (p_1, p_2, p_3)^T$ the center of the imperfection, by M the "rescaled" polarization tensor

$(\frac{\mu_0}{\mu_1} - 1)M^1(\frac{\mu_0}{\mu_1})$, by N the "rescaled" polarization tensor $(\frac{\varepsilon_0}{\varepsilon_1} - 1)M^1(\frac{\varepsilon_0}{\varepsilon_1})$ of this imperfection, and neglect the asymptotically small remainder term in (17), it follows that:

$$\begin{aligned} \Gamma \ := \ \int_{\partial\Omega} \operatorname{curl} E_\alpha \times \nu \cdot w \, d\sigma - \int_{\partial\Omega} \operatorname{curl} w \times \nu \cdot (\nu \times g) \, d\sigma \ \approx \\ \alpha^3 k^2 \, (N \, E_0(p)) \cdot w(p) \ + \ \alpha^3 \, (M \ \operatorname{curl} E_0(p)) \cdot \operatorname{curl} w(p) \, , \end{aligned} \tag{20}$$

with w any smooth vector-valued function satisfying

$$\operatorname{curl}(\operatorname{curl} w) - k^2 w \ = \ 0 \quad \text{in} \quad W \, ,$$

where W is an open neighborhood of Ω.

Let us recall that following (10), we have $E_\alpha = \mathcal{E}_\alpha + u_g$, where u_g is expressed in (7) and $\mathcal{E}_\alpha$ is the solution to (8). The datum g in (7), that defines u_g, is considered from a physical point of view as a current applied on $\partial\Omega$. The discrete field $\mathcal{E}_h$ associated with $\mathcal{E}_\alpha$ is the solution of the discrete formulation (19), and the discrete electric field associated with E_α is defined as: $E_\alpha^h := \mathcal{E}_h + u_g$.

We apply different currents for g that correspond to the following background vector potentials:

$$E_0^{(1)}(x_1, x_2, x_3) \ = \ \begin{pmatrix} 0 \\ 0 \\ \mathrm{e}^{\mathrm{i}kx_2} \end{pmatrix} \, , \quad E_0^{(2)}(x_1, x_2, x_3) \ = \ \begin{pmatrix} \mathrm{e}^{\mathrm{i}kx_3} \\ 0 \\ 0 \end{pmatrix} \, , \quad E_0^{(3)}(x_1, x_2, x_3) \ = \ \begin{pmatrix} 0 \\ \mathrm{e}^{\mathrm{i}kx_1} \\ 0 \end{pmatrix} \, .$$

For the current $g^{(1)} = E_0^{(1)} \times \nu$, we put $g := g^{(1)}$ in (7) and compute by (19) the corresponding discrete electric field denoted here by $E_{\alpha,(1)}^h$. Next, we consider the test vector fields

$$w^{(1,1)}(x_1, x_2, x_3) \ = \ \begin{pmatrix} 0 \\ 0 \\ \mathrm{e}^{-\mathrm{i}kx_2} \end{pmatrix} \, , \quad w^{(2,1)}(x_1, x_2, x_3) \ = \ \begin{pmatrix} \mathrm{e}^{-\mathrm{i}kx_2} \\ 0 \\ 0 \end{pmatrix} \, , \quad w^{(3,1)}(x_1, x_2, x_3) \ = \ \begin{pmatrix} 0 \\ 0 \\ \mathrm{e}^{\mathrm{i}kx_2} \end{pmatrix} \, ,$$

in order to evaluate from the left-hand side of (20) the terms $\Gamma_{(j,1)}$, $1 \leq j \leq 3$, defined as:

$$\Gamma_{(j,1)} \ := \ \int_{\partial\Omega} \operatorname{curl} E_{\alpha,(1)}^h \times \nu \cdot w^{(j,1)} \, d\sigma - \int_{\partial\Omega} \operatorname{curl} w^{(j,1)} \times \nu \cdot (\nu \times g^{(1)}) \, d\sigma \, . \tag{21}$$

Also, for the current $g^{(2)} = E_0^{(2)} \times \nu$, we compute by (19) the corresponding discrete electric field denoted $E_{\alpha,(2)}^h$, after putting $g := g^{(2)}$ in (7). With the test vector fields

$$w^{(1,2)}(x_1, x_2, x_3) \ = \ \begin{pmatrix} \mathrm{e}^{-\mathrm{i}kx_3} \\ 0 \\ 0 \end{pmatrix} \, , \quad w^{(2,2)}(x_1, x_2, x_3) \ = \ \begin{pmatrix} 0 \\ \mathrm{e}^{-\mathrm{i}kx_3} \\ 0 \end{pmatrix} \, , \quad w^{(3,2)}(x_1, x_2, x_3) \ = \ \begin{pmatrix} \mathrm{e}^{\mathrm{i}kx_3} \\ 0 \\ 0 \end{pmatrix} \, ,$$

we then evaluate from the left-hand side of (20) the terms $\Gamma_{(j,2)}$, $1 \leq j \leq 3$, defined as follows:

$$\Gamma_{(j,2)} \ := \ \int_{\partial\Omega} \operatorname{curl} E_{\alpha,(2)}^h \times \nu \cdot w^{(j,2)} \, d\sigma - \int_{\partial\Omega} \operatorname{curl} w^{(j,2)} \times \nu \cdot (\nu \times g^{(2)}) \, d\sigma \, . \tag{22}$$

In the same way, for the last current $g^{(3)} = E_0^{(3)} \times \nu$, we compute by (19) the corresponding discrete electric field denoted by $E^h_{\alpha,(3)}$, after taking $g := g^{(3)}$ in (7). Now, we use as the test vector fields

$$w^{(1,3)}(x_1,x_2,x_3) = \begin{pmatrix} 0 \\ \mathrm{e}^{-\mathrm{i}kx_1} \\ 0 \end{pmatrix}, \quad w^{(2,3)}(x_1,x_2,x_3) = \begin{pmatrix} 0 \\ 0 \\ \mathrm{e}^{-\mathrm{i}kx_1} \end{pmatrix}, \quad w^{(3,3)}(x_1,x_2,x_3) = \begin{pmatrix} 0 \\ \mathrm{e}^{\mathrm{i}kx_1} \\ 0 \end{pmatrix},$$

for evaluating from the left-hand side of (20) the terms $\Gamma_{(j,3)}$, $1 \leq j \leq 3$, defined as follows:

$$\Gamma_{(j,3)} := \int_{\partial\Omega} \mathrm{curl}\, E^h_{\alpha,(3)} \times \nu \cdot w^{(j,3)}\, d\sigma - \int_{\partial\Omega} \mathrm{curl}\, w^{(j,3)} \times \nu \cdot (\nu \times g^{(3)})\, d\sigma\,. \tag{23}$$

Each $\Gamma_{(j,i)}$, $1 \leq i,j \leq 3$, is called the *numerical boundary measurement*. By using the formula (20), it follows from (21), (22), and (23) that:

$$\left\{ \begin{array}{rcl} \Gamma_{(1,1)} & \approx & \alpha^3k^2N_{33} + \alpha^3k^2M_{11}\,, \\ \Gamma_{(2,1)} & \approx & \alpha^3k^2N_{13} - \alpha^3k^2M_{31}\,, \\ \Gamma_{(3,1)} & \approx & (\alpha^3k^2N_{33} - \alpha^3k^2M_{11})\mathrm{e}^{2\mathrm{i}kp_2}\,, \\ \Gamma_{(1,2)} & \approx & \alpha^3k^2N_{11} + \alpha^3k^2M_{22}\,, \\ \Gamma_{(2,2)} & \approx & \alpha^3k^2N_{21} - \alpha^3k^2M_{12}\,, \\ \Gamma_{(3,2)} & \approx & (\alpha^3k^2N_{11} - \alpha^3k^2M_{22})\mathrm{e}^{2\mathrm{i}kp_3}\,, \\ \Gamma_{(1,3)} & \approx & \alpha^3k^2N_{22} + \alpha^3k^2M_{33}\,, \\ \Gamma_{(2,3)} & \approx & \alpha^3k^2N_{32} - \alpha^3k^2M_{23}\,, \\ \Gamma_{(3,3)} & \approx & (\alpha^3k^2N_{22} - \alpha^3k^2M_{33})\mathrm{e}^{2\mathrm{i}kp_1}\,, \end{array} \right. \tag{24}$$

where the terms M_{ij} and N_{ij}, $1 \leq i,j \leq 3$, are respectively the coefficients of M and N. The relations in (24) allow us to derive an approximation of the rescaled tensor α^3k^2M or α^3k^2N depending on whether $\varepsilon_1 = \varepsilon_0$ or $\mu_1 = \mu_0$. In fact, the coefficients $(\alpha^3k^2M)_{ij}$ or $(\alpha^3k^2N)_{ij}$, $1 \leq i,j \leq 3$, are obtained from the measurements $\Gamma_{(1,i)}$, $\Gamma_{(2,i)}$, $1 \leq i \leq 3$.

Once an approximation of the tensor α^3k^2M or α^3k^2N is determined, we can localize the center of the imperfection by using the measurements $\Gamma_{(3,i)}$, $1 \leq i \leq 3$. This will always be possible for certain values of k and when the polarization tensor $M^1(\frac{\mu_0}{\mu_1})$, or $M^1(\frac{\varepsilon_0}{\varepsilon_1})$ respectively, is positive definite, namely when $\mu_0 > 0$, $\mu_1 > 0$, $\varepsilon_0 > 0$, and $\varepsilon_1 > 0$.

By considering therefore three boundary currents, and nine test fields, we determine both an approximation of the rescaled tensor (α^3k^2M when $\varepsilon_1 = \varepsilon_0$, or α^3k^2N when $\mu_1 = \mu_0$) and an approximation of the center of the imperfection.

The measurements in (24) do not allow us however to determine the approximations of the rescaled tensors α^3k^2M and α^3k^2N in the general case, where both $\mu_1 \neq \mu_0$ and $\varepsilon_1 \neq \varepsilon_0$.

When the polarization tensors $M^1(\frac{\mu_0}{\mu_1})$ and $M^1(\frac{\varepsilon_0}{\varepsilon_1})$ are known, an approximation of the size of the imperfection can be determined from one of the measurements $\Gamma_{(1,i)}$, $1 \leq i \leq 3$, even if $\mu_1 \neq \mu_0$ and $\varepsilon_1 \neq \varepsilon_0$, with of course $\mu_0 > 0$, $\mu_1 > 0$, $\varepsilon_0 > 0$, $\varepsilon_1 > 0$.

5.2 MUSIC Algorithm

The MUSIC algorithm is essentially a method for characterizing the range of a self-adjoint operator. In signal processing problems, this method is generally used for estimating the individual frequencies of multiple-harmonic signals [23]. Let us present briefly the approach following [3], [11]. Consider a self-adjoint operator A with eigenvalues $\lambda_1 \geq \lambda_2 \geq ...$, associated with eigenvectors v_1, v_2, ..., respectively. Assume that the eigenvalues λ_{n+1}, λ_{n+2}, ... are all zero, so that the vectors v_{n+1}, v_{n+2}, ... span the null space of A. Alternatively, λ_{n+1}, λ_{n+2}, ... could be very small, below the noise level of the system represented by A; we say in this case that v_{n+1}, v_{n+2}, ... span the noise subspace of A. The projection onto the noise subspace is explicitly given by $P_{\rm noise} = \sum_{i>n} v_i \overline{v_i}^T$, where the bar denotes the complex conjugate. The (essential) range of A is spanned by the vectors v_1, v_2, ..., v_n. The main idea of MUSIC is that: since A is self-adjoint, we know that the noise subspace is orthogonal to the (essential) range, and therefore a vector g is in the range of A if and only if its projection onto the noise subspace is zero. Thus, the MUSIC characterization of the range of A is that: g is in the range of A when $\|P_{\rm noise} g\| = 0$, i.e. if and only if $\frac{1}{\|P_{\rm noise} g\|} = +\infty$, where $\|\,.\,\|$ denotes a given vector norm.

If A is not self-adjoint, instead of the eigenvalue decomposition, the singular-value decomposition is needed. Of course, MUSIC makes use of the eigenvalue structure of a matrix also called the Multi-Static Response (MSR) matrix, or else it uses a singular-value decomposition.

Let us now specify how MUSIC is applied for localizing the imperfections in our context, where we distinguish the following three cases: electric imperfections, magnetic imperfections, and electromagnetic imperfections. We already mention that, as opposed to the method of the previous subsection, the MUSIC algorithm will allow us to determine the locations of several imperfections. By neglecting the asymptotically small remainder term in (17), we get:

$$\begin{aligned} \int_{\partial\Omega} \mathrm{curl}\, E_\alpha \times \nu \cdot w \, d\sigma - \int_{\partial\Omega} \mathrm{curl}\, w \times \nu \cdot (\nu \times g)\, d\sigma \;\approx \\ \alpha^3 \sum_{j=1}^{m} k^2 (\tfrac{\varepsilon_0}{\varepsilon_j} - 1) \left[M^j(\tfrac{\varepsilon_0}{\varepsilon_j}) E_0(z_j) \right] \cdot w(z_j) + \\ \alpha^3 \sum_{j=1}^{m} (\tfrac{\mu_0}{\mu_j} - 1) \left[M^j(\tfrac{\mu_0}{\mu_j}) \,\mathrm{curl}\, E_0(z_j) \right] \cdot \mathrm{curl}\, w(z_j)\,, \end{aligned} \tag{25}$$

where E_α is determined through the solution $\mathcal{E}_\alpha$ of (8), and g is defined as in (7).

For a clear presentation, suppose that Ω is the unit ball. Let $(\theta_1, ..., \theta_n) \in (S^2)^n$ be n directions of incidence, and denote by $(\hat{x}_1, ..., \hat{x}_n)$, n directions of observation, where $\hat{x}_l \cdot \theta_l = 0$, i.e. $\hat{x}_l = \theta_l^\perp$ for $l = 1, ..., n$. Here, the essential assumption is that $n \geq m$.

Let us apply different currents for g that correspond to the background vector potentials $E_{0,(l)}(x) = \theta_l^\perp e^{ik\theta_l \cdot x}$, $1 \leq l \leq n$. From each applied current $g^{(l)} = E_{0,(l)} \times \nu$, $1 \leq l \leq n$, we take $g := g^{(l)}$ in (7) and compute through (19) the corresponding discrete electric field denoted by $E^h_{\alpha,(l)}$. Taking now as the test vector field $w^{(l')}(x) = \theta_{l'}^\perp e^{ik\theta_{l'} \cdot x}$, $1 \leq l' \leq n$, we evaluate from the left-hand side of (25) the

term defined as follows,

$$A_{ll'} \;:=\; \int_{\partial\Omega} \mathrm{curl}\, E^h_{\alpha,(l)} \times \nu \cdot w^{(l')}\, d\sigma - \int_{\partial\Omega} \mathrm{curl}\, w^{(l')} \times \nu \cdot (\nu \times g^{(l)})\, d\sigma\,,$$

that denotes a numerical boundary measurement. In this way we build numerically the matrix $A := (A_{ll'})_{1\leq l,l'\leq n}$. With these particular choices of background vector potentials and test vector fields, we get from the right-hand side of (25):

$$\alpha^3 \sum_{j=1}^{m} \left[k^2(\frac{\varepsilon_0}{\varepsilon_j} - 1) \left(M^j(\frac{\varepsilon_0}{\varepsilon_j})\, \theta_l^\perp \right) \cdot \theta_{l'}^\perp \;-\; k^2(\frac{\mu_0}{\mu_j} - 1) \left(M^j(\frac{\mu_0}{\mu_j})(\theta_l \times \theta_l^\perp) \right) \cdot (\theta_{l'} \times \theta_{l'}^\perp) \right] \mathrm{e}^{\mathrm{i}k(\theta_l+\theta_{l'})\cdot z_j}\,.$$

5.2.1 Electric Imperfections

This is the case where it is assumed that Ω contains m imperfections which are uniquely electric: $\varepsilon_j \neq \varepsilon_0$, $\mu_j = \mu_0$, for all $j = 1, ..., m$.

If we replace the approximation in (25) by an equality, we may write the coefficients of A as follows: for $1 \leq l, l' \leq n$,

$$A_{ll'} \;=\; \alpha^3 \sum_{j=1}^{m} k^2(\frac{\varepsilon_0}{\varepsilon_j} - 1) \left(M^j(\frac{\varepsilon_0}{\varepsilon_j})\, \theta_l^\perp \right) \cdot \theta_{l'}^\perp \mathrm{e}^{\mathrm{i}k(\theta_l+\theta_{l'})\cdot z_j}\,.$$

Let us consider some constant vector $c \in \mathbb{R}^3$ such that $c \cdot \theta_l^\perp \neq 0$, for all $l = 1, ..., n$, and set $A^\star = \overline{A}^T$. Define for $z \in \Omega$,

$$g_{z,c} \;=\; (c \cdot \theta_1^\perp \mathrm{e}^{\mathrm{i}k\theta_1\cdot z},\, ...,\, c \cdot \theta_n^\perp \mathrm{e}^{\mathrm{i}k\theta_n\cdot z})^T\,.$$

Referring now to [1], it can be shown that there exists $n_0 \in \mathbb{N}$ such that for any $n \geq n_0$,

$$g_{z,c} \in \mathrm{Range}(AA^\star) \text{ if and only if } z \in \{z_1, ..., z_m\}.$$

The singular-value decomposition of A will allow the localization of the imperfections. In fact (see [1], [2]), an application of this decomposition is the determination of the number of imperfections, since the number of significant singular-values of A yields the number of detectable imperfections. Typically, if there exist $3m$ significant singular-values of A, then there are m detectable imperfections. If all the singular-values of A are zero or close to zero (when A does not have any significant singular-value), then there are no detectable imperfections in the domain.

In the case where there are detectable imperfections in the domain, we can make use of the singular-vectors of A to locate them. If we call $V_S = [u_1, u_2, ..., u_{n^\star}]$ the matrix block built with significant left singular-vectors of A, where $n^\star$ is the number of these vectors, then $V_S \overline{V_S}^T$ defines the projection onto the signal space of A and we consider $P = I - V_S \overline{V_S}^T$, where I is the $n \times n$ identity matrix, with $n > 3m$. For any point $z \in \Omega$, let us define: $W_c(z) := \dfrac{1}{\|P g_{z,c}\|_2}$, where the 2-norm $\|\,.\,\|_2$ is applied here to a vector of n components. The point z coincides with the location of an imperfection if and only if $P g_{z,c} = 0$. In this way, we can form an image of the imperfections by plotting W_c at each point z of Ω. Then, the resulting plot will have large peaks at the locations of the imperfections.

5.2.2 Magnetic Imperfections

In this case, the domain Ω contains m imperfections which are uniquely magnetic: $\mu_j \neq \mu_0$, $\varepsilon_j = \varepsilon_0$, for all $j = 1, ..., m$.

The localization process of these imperfections is similar to the one described above, and we consider here the previous notation. For $1 \leq l, l' \leq n$, and replacing the approximation in (25) by the equality, the terms of the matrix A now become:

$$A_{ll'} \;=\; -\alpha^3 \sum_{j=1}^{m} k^2 (\frac{\mu_0}{\mu_j} - 1) \left(M^j (\frac{\mu_0}{\mu_j}) (\theta_l \times \theta_l^{\perp}) \right) \cdot (\theta_{l'} \times \theta_{l'}^{\perp}) \mathrm{e}^{\mathrm{i} k (\theta_l + \theta_{l'}) \cdot z_j} \; .$$

Considering $c \in \mathbb{R}^3$ such that $c \cdot (\theta_l^{\perp} \times \theta_l) \neq 0$, for all $l = 1, ..., n$, define for $z \in \Omega$,

$$g_{z,c} \;=\; (c \cdot (\theta_1 \times \theta_1^{\perp}) \mathrm{e}^{\mathrm{i} k \theta_1 \cdot z}, \; ..., \; c \cdot (\theta_n \times \theta_n^{\perp}) \mathrm{e}^{\mathrm{i} k \theta_n \cdot z})^T \; .$$

Also as in Subsection 5.2.1, we refer here to [1], [2]. If there exist $3m$ significant singular-values of A, then there are m detectable imperfections, and if all the singular-values of A are zero or close to zero, then there are no detectable imperfections. An image of detected imperfections is formed by plotting $W_c(z) = \dfrac{1}{\|P g_{z,c}\|_2}$ at each point z of Ω, where $P = I - V_S \overline{V_S}^T$ with $V_S = [u_1, u_2, ..., u_{n^\star}]$ the matrix block built with significant left singular-vectors of A; $n^\star$ being the number of these vectors. Here also, $n > 3m$, I is the $n \times n$ identity matrix and the 2-norm $\| \, . \, \|_2$ is applied to a vector of n components.

5.2.3 Electromagnetic Imperfections

The domain Ω contains here m electromagnetic imperfections: $\varepsilon_j \neq \varepsilon_0$, $\mu_j \neq \mu_0$, for all $j = 1, ..., m$.

The localization process is similar to the one previously presented and we use here the same notation. For $1 \leq l, l' \leq n$, and replacing the approximation in (25) by the equality, the terms of the matrix A are

$$\begin{aligned} A_{ll'} \;&=\; \alpha^3 \sum_{j=1}^{m} \Big[k^2 (\tfrac{\varepsilon_0}{\varepsilon_j} - 1) \left(M^j (\tfrac{\varepsilon_0}{\varepsilon_j}) \, \theta_l^{\perp} \right) \cdot \theta_{l'}^{\perp} \\ &-\; k^2 (\tfrac{\mu_0}{\mu_j} - 1) \left(M^j (\tfrac{\mu_0}{\mu_j}) (\theta_l \times \theta_l^{\perp}) \right) \cdot (\theta_{l'} \times \theta_{l'}^{\perp}) \Big] \, \mathrm{e}^{\mathrm{i} k (\theta_l + \theta_{l'}) \cdot z_j} \; . \end{aligned}$$

Let us consider some constant $c \in \mathbb{R}^3$ such that $c \cdot \theta_l^{\perp} \neq 0$, and $c \cdot (\theta_l^{\perp} \times \theta_l) \neq 0$, for all $l = 1, ..., n$. Define for $z \in \Omega$,

$$g_{z,c} \;=\; \left(\begin{pmatrix} c \cdot \theta_1^{\perp} \\ c \cdot (\theta_1 \times \theta_1^{\perp}) \end{pmatrix} \mathrm{e}^{\mathrm{i} k \theta_1 \cdot z}, \; ..., \; \begin{pmatrix} c \cdot \theta_n^{\perp} \\ c \cdot (\theta_n \times \theta_n^{\perp}) \end{pmatrix} \mathrm{e}^{\mathrm{i} k \theta_n \cdot z} \right)^T \; .$$

We also refer here to [1], [2]. If there exist $5m$ significant singular-values of A, then there are m detectable imperfections, and if all the singular-values of A are zero or close to zero, then there are no detectable imperfections. An image of detected imperfections is formed by plotting $W_c(z) = \dfrac{1}{\|P g_{z,c}\|_2}$ at each point z of Ω, where P is built from significant left singular-vectors of A as previously, $n > 5m$ now, and the 2-norm $\| \, . \, \|_2$ is applied to an $n \times 2$ matrix.

5.3 Inverse Fourier Method

We are concerned in this part with a variational method to determine the locations of the imperfections from boundary measurements. As mentioned in [3], this method is based on the original idea of Calderón [9] which was to reduce the localization problem to the calculation of an inverse Fourier transform.

First of all, let us reconsider the asymptotic formula (17) as

$$\begin{aligned}\Gamma \;:=\; \int_{\partial\Omega} \operatorname{curl} E_\alpha \times \nu \cdot w \, d\sigma - \int_{\partial\Omega} \operatorname{curl} w \times \nu \cdot (\nu \times g)\, d\sigma \;= \\ \alpha^3 \sum_{j=1}^{m} k^2 (\tfrac{\varepsilon_0}{\varepsilon_j} - 1) \left[M^j (\tfrac{\varepsilon_0}{\varepsilon_j}) E_0(z_j) \right] \cdot w(z_j) + \\ \alpha^3 \sum_{j=1}^{m} (\tfrac{\mu_0}{\mu_j} - 1) \left[M^j (\tfrac{\mu_0}{\mu_j}) \operatorname{curl} E_0(z_j) \right] \cdot \operatorname{curl} w(z_j) + \mathrm{O}(\alpha^4)\,,\end{aligned} \tag{26}$$

where $g = E_\alpha \times \nu$ and k is the wave number.

For an arbitrary $\eta \in \mathbb{R}^3$, let us define β and ζ in $\mathbb{R}^3$ such that:

$$\begin{cases} \|\beta\|^2 \;=\; 1, \quad \beta \cdot \eta = 0, \\ \|\zeta\|^2 \;=\; 1, \quad \zeta \cdot \eta \;=\; \zeta \cdot \beta \;=\; 0\,, \end{cases}$$

with $\|\,.\,\|$ denoting the usual norm associated with the Hermitian product on $\mathbb{C}^3$. Let $p \;=\; \eta + \gamma\beta$ such that $p \cdot p \;=\; k^2$, i.e., γ is a complex number such that: $\gamma^2 \;=\; k^2 - \|\eta\|^2$. We assume that we are in possession of the boundary current for the electric field E_α, whose corresponding background potential is given by

$$E_0(x) \;=\; \mathrm{e}^{\mathrm{i}p\cdot x}\zeta\,.$$

In fact, in (26), we set $g(x) = (\mathrm{e}^{\mathrm{i}p\cdot x}\zeta) \times \nu(x)$ and use as the test vector field,

$$w(x) \;=\; \mathrm{e}^{\mathrm{i}q\cdot x}\zeta\,,$$

where $q \;=\; \eta - \gamma\beta$. Namely, as well as E_0, the vector field w is in accordance with (16). With these considerations of g and w, we get from (26) that

$$\begin{aligned}\Gamma \;=\; \alpha^3 \sum_{j=1}^{m} \Big(k^2 (\tfrac{\varepsilon_0}{\varepsilon_j} - 1) \left[M^j (\tfrac{\varepsilon_0}{\varepsilon_j}) \mathrm{e}^{\mathrm{i}p\cdot z_j}\zeta \right] \cdot \mathrm{e}^{\mathrm{i}q\cdot z_j}\zeta + \\ (\tfrac{\mu_0}{\mu_j} - 1) \left[M^j (\tfrac{\mu_0}{\mu_j}) (\mathrm{i}\mathrm{e}^{\mathrm{i}p\cdot z_j} p \times \zeta) \right] \cdot (\mathrm{i}\mathrm{e}^{\mathrm{i}q\cdot z_j} q \times \zeta) \Big) + \mathrm{O}(\alpha^4)\,.\end{aligned} \tag{27}$$

Let us now view the measurement as a function of η:

$$\begin{aligned}\Gamma(\eta) \;\approx\; \alpha^3 \sum_{j=1}^{m} \Big(k^2 (\tfrac{\varepsilon_0}{\varepsilon_j} - 1) \left[M^j (\tfrac{\varepsilon_0}{\varepsilon_j}) \zeta \right] \cdot \zeta - \\ (\tfrac{\mu_0}{\mu_j} - 1) \left[M^j (\tfrac{\mu_0}{\mu_j}) ((\eta + \gamma\beta) \times \zeta) \right] \cdot ((\eta - \gamma\beta) \times \zeta) \Big) \mathrm{e}^{\mathrm{i}2\eta\cdot z_j}\,.\end{aligned}$$

Following Remark 3.2, when all the imperfections are balls, the tensors $M^j(c)$ are of the form $m^j(c)I_3$, where $m^j(c)$ is a scalar depending on c. In this case, we get

$$\Gamma(\eta) \;\approx\; \alpha^3 \sum_{j=1}^{m} \left[k^2 (\frac{\varepsilon_0}{\varepsilon_j} - 1) m^j (\frac{\varepsilon_0}{\varepsilon_j}) \;-\; (\frac{\mu_0}{\mu_j} - 1) m^j (\frac{\mu_0}{\mu_j}) (2\|\eta\|^2 - k^2) \right] \mathrm{e}^{\mathrm{i} 2\eta \cdot z_j} \,. \tag{28}$$

Recall that the function $\mathrm{e}^{\mathrm{i} 2\eta \cdot z_j}$ (up to a multiplicative constant) is exactly the Fourier transform of the Dirac delta δ_{-2z_j} (a point mass located at $-2z_j$). Since $\|\eta\|^2$ is a polynomial in the coordinates η_i, $1 \leq i \leq 3$, of η, we have in the right-hand side of (28) multiplications by powers of η_i in Fourier space that correspond to differentiations of the delta functions. In this particular case, the expression in the right-hand side of (28) is therefore the Fourier transform of a linear combination of derivatives of order less than or equal to 2 of delta functions centered at the points $-2z_j$, $1 \leq j \leq m$. More precisely, the inverse Fourier transform of $\Gamma(\eta)$ is expressed as:

$$\check{\Gamma}(x) \approx \alpha^3 \sum_{j=1}^{m} L_j(\delta_{-2z_j})(x) \,,$$

where L_j is a second order differential operator with constant coefficients depending on $m^j(\frac{\varepsilon_0}{\varepsilon_j})$ and $m^j(\frac{\mu_0}{\mu_j})$. In this approach, a numerical Fourier inversion of a sample of measurements should efficiently pin down the z_j's. This approach has been successfully used in the context of the localization of conductivity imperfections (see [5]). The principle of the inverse Fourier method that will be described here is similar to the one presented by D. Volkov in [24] in the context of a localization of imperfections from an inverse problem based on the bi-dimensional Helmholtz equation.

When some of the imperfections are not balls, we may rewrite (27) as below, where the measurement Γ is viewed again as a function of η:

$$\Gamma(\eta) \;\approx\; \alpha^3 \sum_{j=1}^{m} \left(k^2 (\frac{\varepsilon_0}{\varepsilon_j} - 1) T_{\varepsilon_0, \varepsilon_j}(\eta) \;-\; (\frac{\mu_0}{\mu_j} - 1) T_{\mu_0, \mu_j}(\eta) \right) \mathrm{e}^{\mathrm{i} 2\eta \cdot z_j} \,, \tag{29}$$

with $T_{\varepsilon_0,\varepsilon_j}(\eta) = (M^j(\frac{\varepsilon_0}{\varepsilon_j})\zeta) \cdot \zeta$ and $T_{\mu_0,\mu_j}(\eta) = (M^j(\frac{\mu_0}{\mu_j})((\eta + \gamma\beta) \times \zeta)) \cdot ((\eta - \gamma\beta) \times \zeta)$. The expression in the right-hand side of (29) is in fact the Fourier transform of an operator of a more complicated kind acting on delta functions centered at the points $-2z_j$, $1 \leq j \leq m$. The present localization principle consists of sampling the values of $\Gamma(\eta)$ at some discrete set of points and then evaluating the corresponding discrete inverse Fourier transform. After a rescaling (by $-\frac{1}{2}$), the support of this inverse Fourier transform will provide the locations of the imperfections.

Typically, for each point η of the sampling, we consider $g(x) = (\mathrm{e}^{\mathrm{i}(\eta + \gamma\beta) \cdot x} \zeta) \times \nu(x)$ as the boundary current in (7) and compute through (19) the corresponding discrete electric field, denoted here by E_α^h. After determining the discrete field, $\mathrm{curl} E_\alpha^h \times \nu$, we evaluate numerically the measurement $\Gamma(\eta)$ by using of course $w(x) = \mathrm{e}^{\mathrm{i}(\eta - \gamma\beta) \cdot x} \zeta$ as the test field in $\int_{\partial\Omega} \mathrm{curl}\, E_\alpha \times \nu \cdot w \, d\sigma - \int_{\partial\Omega} \mathrm{curl}\, w \times \nu \cdot (\nu \times g) \, d\sigma$, and by replacing E_α by E_α^h in this difference of terms representing in fact the left-hand side of (27).

Let us now specify, following [24], a possible way to relate the continuous Fourier transform of a function that does not decrease rapidly to its discrete FFT. Namely, we describe a way to choose a step size for sampling with respect to η in the numerical simulations.

First of all, let us assume that all the centers $z_j = (z_j^1, z_j^2, z_j^3)^T$ of the imperfections $(1 \leq j \leq m)$ lie in a domain $[-K, K]^3$, where the bound K is known. To simplify the presentation, let us consider the formula (28) and rewrite simply its right-hand side as:

$$\sum_{j=1}^{m} C_j \, \mathrm{e}^{2\mathrm{i}(\eta_1 z_j^1 + \eta_2 z_j^2 + \eta_3 z_j^3)} \,, \tag{30}$$

where the complex constants C_j are unknown. As previously mentioned, for each $\eta = (\eta_1, \eta_2, \eta_3)^T$, we are able to evaluate the measurement $\Gamma(\eta)$ and therefore we assume that (30) is known for $(\eta_1, \eta_2, \eta_3)^T \in [-\eta_{\max}, \eta_{\max}]^3$, on a regular grid made up of n^3 points. We are then in possession of the sequence of data:

$$\sum_{j=1}^{m} C_j \, \mathrm{e}^{2\mathrm{i}((-\eta_{\max}+(l_1-1)\rho)z_j^1 + (-\eta_{\max}+(l_2-1)\rho)z_j^2 + (-\eta_{\max}+(l_3-1)\rho)z_j^3)} \,, \quad 1 \leq l_1, l_2, l_3 \leq n \,,$$

where $\rho = \dfrac{2\eta_{\max}}{n}$. After applying the inverse FFT to this sequence, we get

$$\begin{aligned} \frac{1}{n^3} \sum_{j=1}^{m} C_j \sum_{1 \leq l_1, l_2, l_3 \leq n} & \mathrm{e}^{2\mathrm{i}((-\eta_{\max}+(l_1-1)\rho)z_j^1 + (-\eta_{\max}+(l_2-1)\rho)z_j^2 + (-\eta_{\max}+(l_3-1)\rho)z_j^3)} \\ & \times \mathrm{e}^{2\mathrm{i}\pi(\frac{(l_1-1)}{n}(s_1-1) + \frac{(l_2-1)}{n}(s_2-1) + \frac{(l_3-1)}{n}(s_3-1))} \,, \end{aligned} \tag{31}$$

with $1 \leq s_1, s_2, s_3 \leq n$. Let us now consider the module of the term in (31), reduced as follows:

$$\left| \sum_{j=1}^{m} \frac{1}{n^3} 8 C_j \frac{\sin(2\eta_{\max} z_j^1) \sin(2\eta_{\max} z_j^2) \sin(2\eta_{\max} z_j^3)}{(\mathrm{e}^{2\pi(\frac{\rho z_j^1}{\pi} + \frac{s_1-1}{n})\mathrm{i}} - 1)(\mathrm{e}^{2\pi(\frac{\rho z_j^2}{\pi} + \frac{s_2-1}{n})\mathrm{i}} - 1)(\mathrm{e}^{2\pi(\frac{\rho z_j^3}{\pi} + \frac{s_3-1}{n})\mathrm{i}} - 1)} \right| . \tag{32}$$

Then, as n becomes large, the quantity in (32) is small unless one of the terms $\dfrac{\rho z_j^1}{\pi} + \dfrac{s_1 - 1}{n}$, $\dfrac{\rho z_j^2}{\pi} + \dfrac{s_2 - 1}{n}$, and $\dfrac{\rho z_j^3}{\pi} + \dfrac{s_3 - 1}{n}$ is close to an integer. By enforcing (for example)

$$\frac{K\rho}{\pi} \lesssim \frac{1}{3} \,, \tag{33}$$

each one of the previous terms shall only approach the integers 0 or 1, in the case where n becomes large ($n \geq 3$). It has been assumed here of course that $|z_j^r| \leq K$, for $1 \leq r \leq 3$ and $1 \leq j \leq m$. The relation (33) provides a practical way to choose the step size ρ and also gives a link between $\eta_{\max}$, K and n. In fact, we have $\rho = \dfrac{2\eta_{\max}}{n}$ and take from (33),

$$\rho \approx \frac{1}{K} \,. \tag{34}$$

In this approach, we shall fix ρ according to (34) and consider simultaneously increasing values of n and of $\eta_{\max}$ for more accuracy. This is a localization method whose centers z_j, $1 \leq j \leq m$, are localized from the sequence of the modules of the terms in (31).

Let us examine the resulting order of resolution of the method. Assuming $1 \leq r \leq 3$, $1 \leq j \leq m$ and $n \geq 3$ fixed, the case where $\dfrac{\rho z_j^r}{\pi} + \dfrac{s_r - 1}{n}$ approaches 1 or 0 corresponds in fact to the existence

of $s_r^\star$, $1 \leq s_r^\star \leq n$, such that $z_j^r \approx \pi K - \frac{\pi}{\rho}\frac{s_r^\star - 1}{n} = \pi K - \frac{\pi}{2\eta_{\max}}(s_r^\star - 1)$, or respectively to the existence of $s_r^{\star\star}$, $1 \leq s_r^{\star\star} \leq n$, such that $z_j^r \approx -\frac{\pi}{\rho}\frac{s_r^{\star\star} - 1}{n} = -\frac{\pi}{2\eta_{\max}}(s_r^{\star\star} - 1)$. Now, depending on the sign of z_j^r, we are concerned with a domain of interest and more precisely with the points of which one of the coordinates is (theoretically) near to $\pi K - \frac{\pi}{2\eta_{\max}}(s-1)$ or to $-\frac{\pi}{2\eta_{\max}}(s-1)$, where $1 \leq s \leq n$. The present procedure provides therefore a sampling of the "physical" domain in association with the considered sampling for $[-\eta_{\max}, \eta_{\max}]^3$. We need, in summary, of the order of n^3 sampled values of $\Gamma(\eta_1, \eta_2, \eta_3)$ to locate, with at best (theoretically) a resolution of order $\frac{\pi}{2\eta_{\max}}$, a collection of imperfections that lie inside a cube of side $2K$, where the step size $\rho = \frac{2\eta_{\max}}{n}$ for sampling is in accordance with (34).

5.4 A Common Description of the Localization Procedures

Each one of the localization procedures previously introduced can be summarized in four stages:

i) consideration of a finite number of electric currents to apply on the boundary of the domain;

ii) computation of the discrete electric field (associated with E_α) through the discrete formulation (19), for each applied boundary current;

iii) computation of the numerical boundary measurement arising from the asymptotic formula (17), for each applied boundary current and each used test field;

iv) application of the considered inversion process.

In the first stage, incident waves illuminate the domain following a well-chosen setting. The second stage concerns the computation of the discrete electric field by the finite element method. Here, the discrete system resulting from the formulation (19) is solved with the help of a GMRES algorithm preconditioned by an incomplete **LU** factorization. Stage *iii*) makes use of both the asymptotic formula (17) and the discrete electric field, as well as particular test fields. Of course, for each incident wave illuminating the domain, we define an "observation point" on the boundary of the domain (that corresponds in fact to a direction of observation) from which the vector field used as a test field in (17) is generated. Stage *iv*) is the one that provides the location(s) of the imperfection(s) in the domain. The centers of the imperfections are localized after some calculations (required by the inversion process) and graphical post-processing.

6 Numerical Simulations

Making use of the procedures described in Section 5, we present in this part the numerical results of the effective localization of the imperfections in various contexts.

6.1 Computational Configurations

The domain Ω is here a polyhedron having the shape of the unit ball. Two distinct configurations are considered: the case where Ω contains a single imperfection and when it contains multiple imperfections. For the first configuration, the single imperfection is a polyhedron having the shape of a ball of center $p = (p_1, p_2, p_3)^T \in \Omega$ and of radius α. We represent then the discretization of $\overline{\Omega}$ by

- $\mathcal{T}_\alpha^1$ when $p = (0.23, -0.31, 0.15)^T$, with $\alpha = 0.2$;
- $\mathcal{T}_\alpha^2$ when $p = (0.23, -0.31, 0.15)^T$, with $\alpha = 0.17$.

In the second configuration, Ω contains more than one imperfection and each imperfection is a polyhedron having the shape of a ball or of an ellipsoid. The discretization of $\overline{\Omega}$ is thus represented by:

- $\mathcal{T}_\alpha^3$ when Ω contains two ball-like shaped imperfections of centers $(0.23, -0.31, 0.15)^T$, $(-0.17, 0.43, -0.11)^T$, and of the same 'radius' $\alpha = 0.2$;
- $\mathcal{T}_\alpha^4$ when Ω contains three ball-like shaped imperfections of centers $(0.23, -0.31, 0.15)^T$, $(-0.17, -0.43, -0.11)^T$, $(-0.5, 0.25, 0.1)^T$, with respective 'radii' 0.18, 0.16 and 0.17. In this case, we denote by α the maximal radius and by $\alpha_{\min}$ the minimal radius: $\alpha = 0.18$, $\alpha_{\min} = 0.16$;
- $\mathcal{T}_\alpha^5$ when Ω contains three imperfections one of which has the shape of a ball of radius 0.16 and of center $(0.23, -0.31, 0.15)^T$. The second one has the shape of an ellipsoid centered at $(-0.17, -0.43, -0.11)^T$ with semi-axes of lengths 0.16, 0.16, 0.18 in the directions Ox, Oy, Oz respectively. The last imperfection is also ellipsoid-shaped, but centered at $(-0.5, 0.25, 0.1)^T$ with the 'semi-axes' (on Oxy) rotated about Oz by an angle of $\frac{\pi}{4}$. The lengths of the 'semi-axes' of this imperfection are 0.16, 0.17 and 0.19. Now, α is the maximal value of the semi-axes lengths and the 'radius' of the first imperfection, and $\alpha_{\min}$ is the minimal value of these quantities: $\alpha = 0.19$, $\alpha_{\min} = 0.16$.

Each one of these discretizations is of course associated with a conforming mesh made up of tetrahedra that takes implicitly into account the geometry of each imperfection; the resulting mesh size h is here systematically smaller than the lowest of the 'radii' or 'semi-axes lengths' of the imperfections ($h < \alpha_{\min}$). In the following table, we give some characteristics of the mesh in each one of these settings.

	NK	NIE	NIV	nf	ne	h
$\mathcal{T}_\alpha^1$	45101	49906	6643	3678	5517	0.17725
$\mathcal{T}_\alpha^2$	54368	60753	8215	3662	5493	0.15717
$\mathcal{T}_\alpha^3$	55847	62386	8425	3774	5661	0.15718
$\mathcal{T}_\alpha^4$	64765	72662	9872	3952	5928	0.14810
$\mathcal{T}_\alpha^5$	74093	83334	11363	4246	6369	0.14534

We have denoted by NK, NIE, NIV the number of tetrahedra, internal edges and internal vertices respectively. Also, nf, ne are respectively the number of boundary faces and boundary edges.

6.2 Numerical Study of Electric Perturbations

Before devoting our attention to the numerical localization of the imperfections, we first inspect numerically the asymptotic formula (15) that allows us to study the perturbation $(\frac{1}{\mu_\alpha}\operatorname{curl} E_\alpha - \frac{1}{\mu_0}\operatorname{curl} E_0)\times \nu|_{\partial\Omega}$, in the tangential boundary trace of the curl of the electric field.

In what follows, all our numerical results will be described with respect to the parameter

$$\tau := \alpha\,\omega\,, \tag{35}$$

which has here a physical sense (since linked to the frequency ω) contrary to α. If the domain Ω was a ball of radius r, the parameter in (35) would be defined as: $\tau = \alpha\omega/r$.

When Ω contains a single imperfection centered at $p = (p_1, p_2, p_3)^T$, the formula (15) is rewritten as follows: for any $z \in \partial\Omega$,

$$\begin{gathered}(\frac{1}{\mu_\alpha}\operatorname{curl} E_\alpha - \frac{1}{\mu_0}\operatorname{curl} E_0)(z)\times\nu(z)\\ -2\int_{\partial\Omega}\operatorname{curl}_z(\Phi^k(x,z)(\frac{1}{\mu_\alpha}\operatorname{curl} E_\alpha - \frac{1}{\mu_0}\operatorname{curl} E_0)(x)\times\nu(x))\times\nu(z)\,d\sigma_x \;=\\ 2\,\tau^2\alpha(\frac{\mu_0}{\mu_1}-1)G(p,z)\times\nu(z)M^1(\frac{\mu_0}{\mu_1})(\operatorname{curl} E_0)(p)\\ +2\,\tau^2\alpha\varepsilon_0(\frac{1}{\varepsilon_1}-\frac{1}{\varepsilon_0})((\operatorname{curl}_x G)(p,z))^T\times\nu(z)M^1(\frac{\varepsilon_0}{\varepsilon_1})E_0(p)+\mathrm{O}(\alpha^4)\,.\end{gathered}$$

In order to inspect numerically this formula, we consider the functional defined as follows: for any $z \in \partial\Omega$,

$$\begin{gathered}R_\tau(z) := (\frac{1}{\mu_\alpha}\operatorname{curl} E^h_\alpha - \frac{1}{\mu_0}\operatorname{curl} E_0)(z)\times\nu(z)\\ -2\int_{\partial\Omega}\operatorname{curl}_z(\Phi^k(x,z)(\frac{1}{\mu_\alpha}\operatorname{curl} E^h_\alpha - \frac{1}{\mu_0}\operatorname{curl} E_0)(x)\times\nu(x))\times\nu(z)\,d\sigma_x\\ -2\,\tau^2\alpha(\frac{\mu_0}{\mu_1}-1)G(p,z)\times\nu(z)M^1(\frac{\mu_0}{\mu_1})(\operatorname{curl} E_0)(p)\\ -2\,\tau^2\alpha\varepsilon_0(\frac{1}{\varepsilon_1}-\frac{1}{\varepsilon_0})((\operatorname{curl}_x G)(p,z))^T\times\nu(z)M^1(\frac{\varepsilon_0}{\varepsilon_1})E_0(p)\,.\end{gathered} \tag{36}$$

From a boundary current $g = E_0\times\nu$ associated with the background vector potential E_0 such that

$$\left\{\begin{array}{l} E_0(x) \;=\; \mathrm{e}^{\mathrm{i}kx\cdot v}v^\perp,\\ x\in\overline{\Omega},\; v \;=\; (\cos(\psi)\sin(\phi),\sin(\psi)\sin(\phi),\cos(\phi))^T,\end{array}\right. \tag{37}$$

with $\psi \in [0, 2\pi]$ and $\phi \in [0, \pi]$ fixed, we compute through (19) the corresponding discrete electric field E^h_α, in the domain $\overline{\Omega}$ whose discretization is here $\mathcal{T}^1_\alpha$ or $\mathcal{T}^2_\alpha$. The evaluation of R_τ, at a finite number, L, of points on $\partial\Omega$, requires the calculation of the integral term in (36) as well as the approximations of the polarization tensors $M^1(\frac{\mu_0}{\mu_1})$ and $M^1(\frac{\varepsilon_0}{\varepsilon_1})$. We compute this integral term with a numerical integration method of order 2. For evaluating numerically $M^1(\frac{\mu_0}{\mu_1})$ or $M^1(\frac{\varepsilon_0}{\varepsilon_1})$, we first consider a weak formulation in scalar potential making use of a boundary integral operator, and associated with (13). After discretizing this formulation from a combination of interior nodal finite elements with

boundary finite elements of first-order (see e.g. [18] for the approximation of the mentioned boundary integral operator), we compute the discrete scalar potential associated with (13), and then use it to evaluate numerically the coefficients of the tensor from (14).

Let $\theta_l = (\cos(2\pi\frac{l-1}{L-1})\sin(\pi\frac{l-1}{L-1}), \sin(2\pi\frac{l-1}{L-1})\sin(\pi\frac{l-1}{L-1}), \cos(\pi\frac{l-1}{L-1}))^T$, $1 \leq l \leq L$, be the boundary points where R_τ will be evaluated, and set:

$$R_\tau^\infty \;=\; \max_{1\leq l\leq L} |R_\tau(\theta_l)|_{\mathbb{C}^3}\,,$$

with $|.|_{\mathbb{C}^3}$ the infinity-norm on $\mathbb{C}^3$.

A study of R_τ^∞ with respect to the parameter τ is proposed below. The numerical results represented in Figures 2 - 7 have been obtained with $10^{-4} \leq \tau < 1$, $L = 21$, and $\mu_0 = \varepsilon_0 = 1$.

We summarize in Figures 2 - 3 the results obtained from the discretization $\mathcal{T}_\alpha^1$ and by considering $\psi = 2\pi$, $\phi = \pi$ in (37).

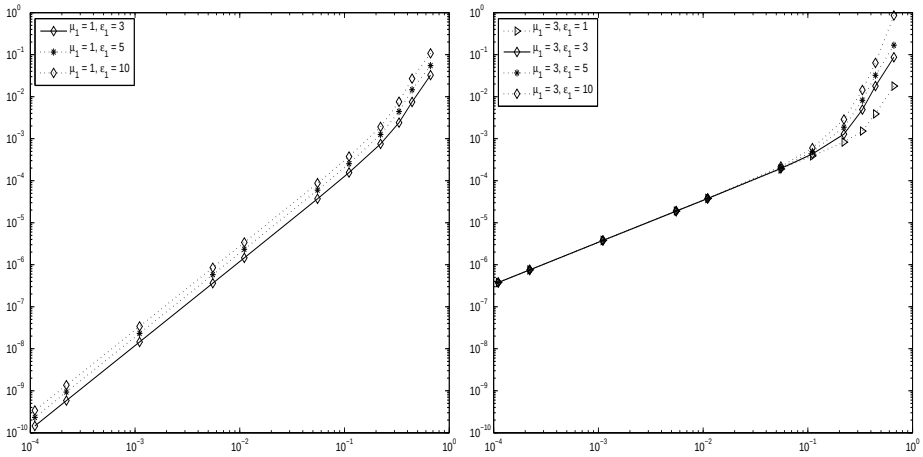

Figure 2: Log-log representation of R_τ^∞ with respect to some values of τ, from the discretization $\mathcal{T}_\alpha^1$ and for $\psi = 2\pi$, $\phi = \pi$ in (37), $\varepsilon_1 = 1, 3, 5, 10$ with $\mu_1 = 1$ (at left) and $\mu_1 = 3$ (at right).

In Figures 4 - 5 we represent the results obtained from the discretization $\mathcal{T}_\alpha^1$ again, but with $\psi = \frac{7\pi}{4}$, $\phi = \frac{\pi}{4}$ in (37). In comparison with the results of Figures 2 - 3, we notice that R_τ^∞ preserves the same variations with respect to τ.

The results represented in Figures 6 - 7 have been obtained by considering $\psi = 2\pi$, $\phi = \pi$ and the discretization $\mathcal{T}_\alpha^2$; these results are more accurate than those of Figures 2 - 3 deriving from $\mathcal{T}_\alpha^1$ with the same choice of values of the parameters μ_1, ε_1, ψ and ϕ.

Similar results to those represented in Figure 6 - 7 have been obtained from simulations, by using again $\mathcal{T}_\alpha^2$, but with $\psi = \frac{7\pi}{4}$, $\phi = \frac{\pi}{4}$, and it follows that these results are more accurate than those of Figures 4 - 5.

We can observe from Figures 2 - 7 the numerical asymptotic behaviour of R_τ^∞ with respect to τ. It appears on the other hand that R_τ^∞ varies with respect to the contrast of the domain, independently of the considered setting. We also notice that the values of R_τ^∞ are more accurate in the case $\mu_1 = \mu_0$,

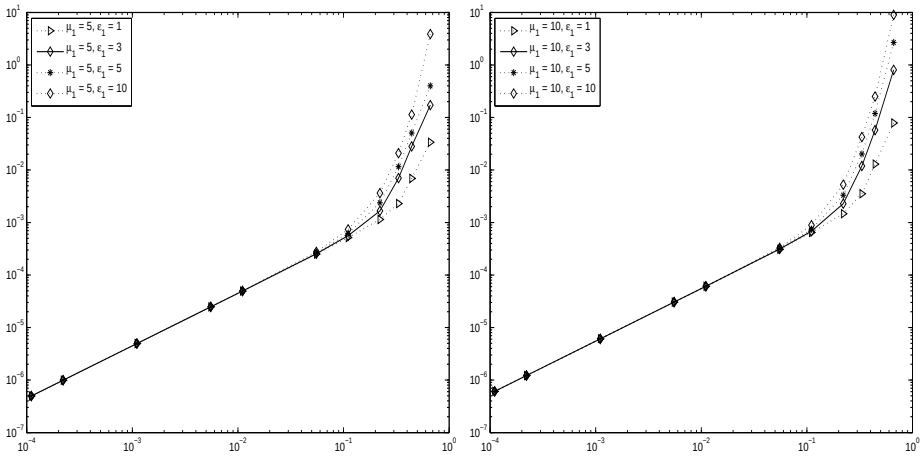

Figure 3: Log-log representation of R_τ^∞ with respect to some values of τ, from the discretization $\mathcal{T}_\alpha^1$ and for $\psi = 2\pi$, $\phi = \pi$ in (37), $\varepsilon_1 = 1, 3, 5, 10$ with $\mu_1 = 5$ (at left) and $\mu_1 = 10$ (at right).

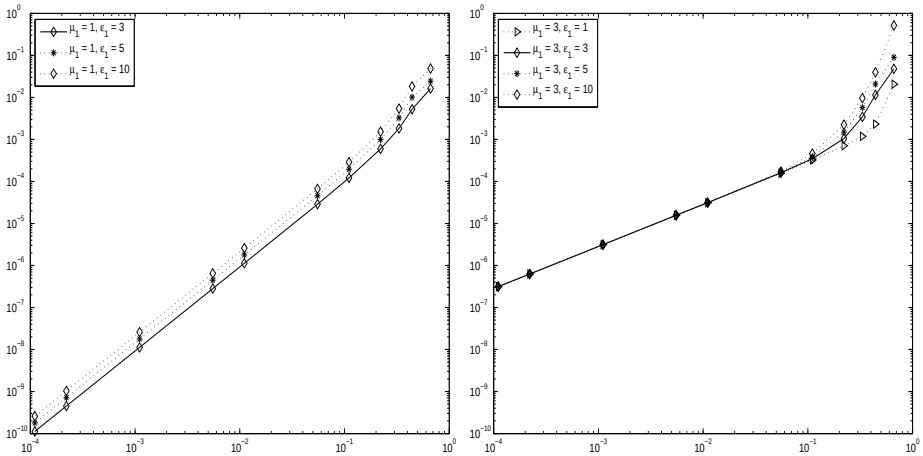

Figure 4: Log-log representation of R_τ^∞ with respect to some values of τ, from the discretization $\mathcal{T}_\alpha^1$ and for $\psi = \frac{7\pi}{4}$, $\phi = \frac{\pi}{4}$ in (37), $\varepsilon_1 = 1, 3, 5, 10$ with $\mu_1 = 1$ (at left) and $\mu_1 = 3$ (at right).

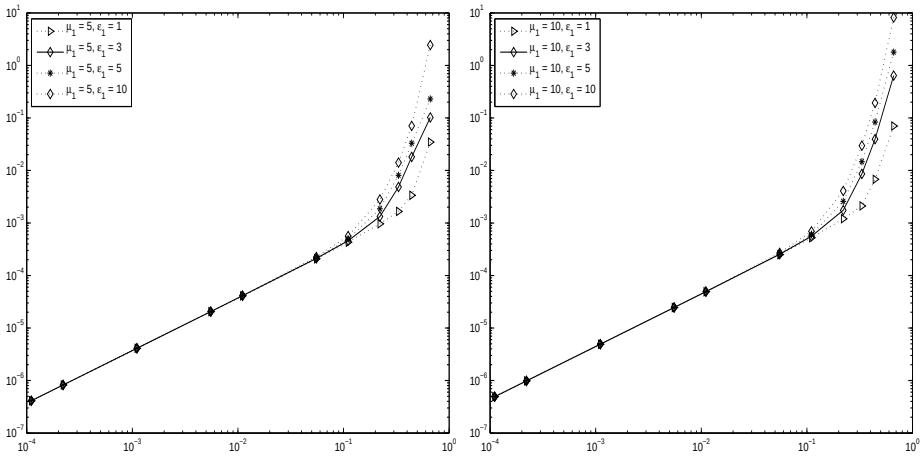

Figure 5: Log-log representation of R_τ^∞ with respect to some values of τ, from the discretization $\mathcal{T}_\alpha^1$ and for $\psi = \frac{7\pi}{4}$, $\phi = \frac{\pi}{4}$ in (37), $\varepsilon_1 = 1, 3, 5, 10$ with $\mu_1 = 5$ (at left) and $\mu_1 = 10$ (at right).

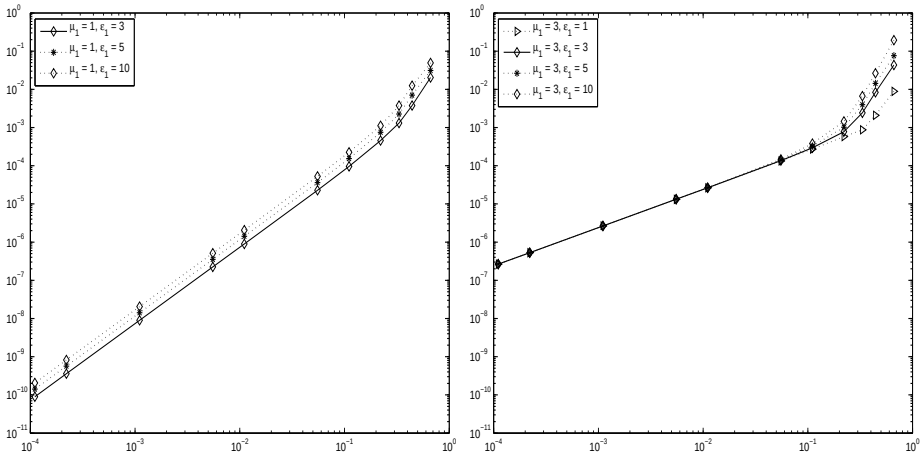

Figure 6: Log-log representation of R_τ^∞ with respect to some values of τ, from the discretization $\mathcal{T}_\alpha^2$ and for $\psi = 2\pi$, $\phi = \pi$ in (37), $\varepsilon_1 = 1, 3, 5, 10$ with $\mu_1 = 1$ (at left) and $\mu_1 = 3$ (at right).

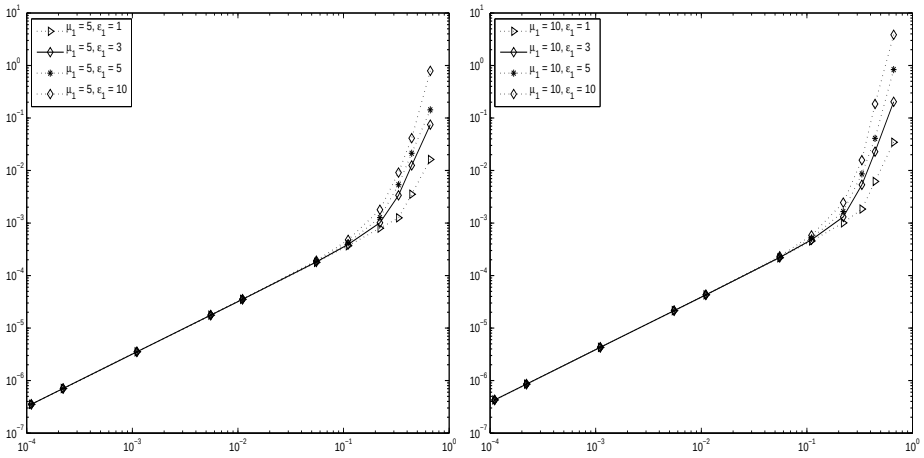

Figure 7: Log-log representation of R_τ^∞ with respect to some values of τ, from the discretization $\mathcal{T}_\alpha^2$ and for $\psi = 2\pi$, $\phi = \pi$ in (37), $\varepsilon_1 = 1, 3, 5, 10$ with $\mu_1 = 5$ (at left) and $\mu_1 = 10$ (at right).

with $\varepsilon_1 \neq \varepsilon_0$, when τ becomes small; this was foreseeable from the choice of the background vector potential made in (37). Our numerical inspection also indicates that (15), and consequently the asymptotic formula (17), must be numerically considered only for a restricted range of values of the parameter $\tau = \alpha\omega$ ($\tau < 1$) in view of the computation of boundary measurements. In fact, the numerical accuracy of (15) is lost for any 'high' frequency ω such that τ is not small ($\tau \lesssim 1$), and since the formula (17) shall become inaccurate, the localization will not be achieved with precision in such a case. The same conclusion about the localization is also reported for any 'low' frequency ω such that τ is too small ($\tau \ll 1$). In this last context, the numerical accuracy of (15) is preserved whereas the values of measurements that will derive from (17) will be too small in such a way that the contrast of the domain will not be reflected by these measurements.

6.3 Numerical Localization from the Procedure based on the Current Projection Method

We now describe the results of the numerical localization of a single imperfection, from the procedure based on the Current Projection method (see Subsection 5.1). Typically, we consider (24) by distinguishing the cases: $\mu_1 = \mu_0$ with $\varepsilon_1 \neq \varepsilon_0$, and $\mu_1 \neq \mu_0$ with $\varepsilon_1 = \varepsilon_0$, after fixing $\mu_0 = \varepsilon_0 = 1$.

As mentioned earlier, the reconstruction of the center of the imperfection will always be possible for certain values of k. More precisely, since the domain Ω represents here the unit ball, this reconstruction will be achieved by using (24) for any frequency such that k is in accordance with Remark 3.1, and $k < \frac{\pi}{2}$ for example. It is already important to notice that this consideration is not in fact in contradiction with the one of the parameter τ that results from the numerical study done in the previous subsection.

Let us respectively denote by $\frac{|\alpha - \alpha_h|}{|\alpha|}$, $\frac{|p - p_h|_{\mathbf{R}^3}}{|p|_{\mathbf{R}^3}}$, where $|.|_{\mathbf{R}^3}$ is the infinity norm on $\mathbb{R}^3$, the relative errors on the radius α and the center p of the imperfection, when α_h, p_h are the radius and the center of the localized imperfection.

Figures 8 - 9 present the results obtained from the discretizations $\mathcal{T}_\alpha^1$ and $\mathcal{T}_\alpha^2$, with $\mu_1 = 1$, $\varepsilon_1 = 3, 5, 10$. We observe asymptotic behaviours of the relative errors on the radius and the center of the imperfection with respect to τ. Similar results have been obtained from simulations, for $\mu_1 = 3, 5, 10$ with $\varepsilon_1 = 1$. It appears that the relative error on the radius obtained from $\mathcal{T}_\alpha^2$ is asymptotically slightly smaller than the one resulting from $\mathcal{T}_\alpha^1$.

Independently of the considered discretization, the relative error on the radius increases with respect to τ, whereas the relative error on the center decreases with respect to τ. It also appears that, for a range of values of τ, the relative error on the center obtained from $\mathcal{T}_\alpha^2$ is slightly smaller than the one resulting from $\mathcal{T}_\alpha^1$. Since the same smallness has been noticed for the relative error on the radius, we can hence expect better reconstructions of the imperfection defined from $\mathcal{T}_\alpha^2$ in comparison to reconstructions of the imperfection defined from $\mathcal{T}_\alpha^1$, at the same frequencies.

The relative errors on the radius and the center vary with respect to the contrast of the domain, independently of the considered setting. It follows in particular that the reconstruction of any imperfection, for which $\mu_1 = 1$ and $|\varepsilon_1|$ has a large value (respectively $\varepsilon_1 = 1$ and μ_1 has a large value),

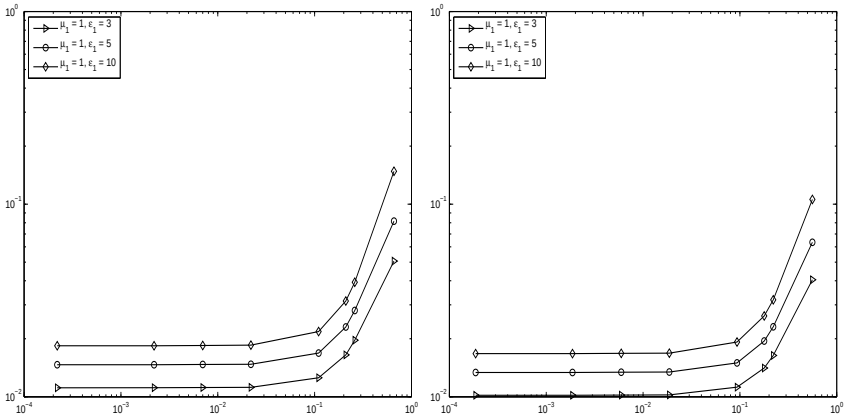

Figure 8: Log-log representation of the relative error on the radius with respect to some values of τ, for $\mu_1 = 1$ with $\varepsilon_1 = 3, 5, 10$, from the discretizations $\mathcal{T}_\alpha^1$ (at left) and $\mathcal{T}_\alpha^2$ (at right).

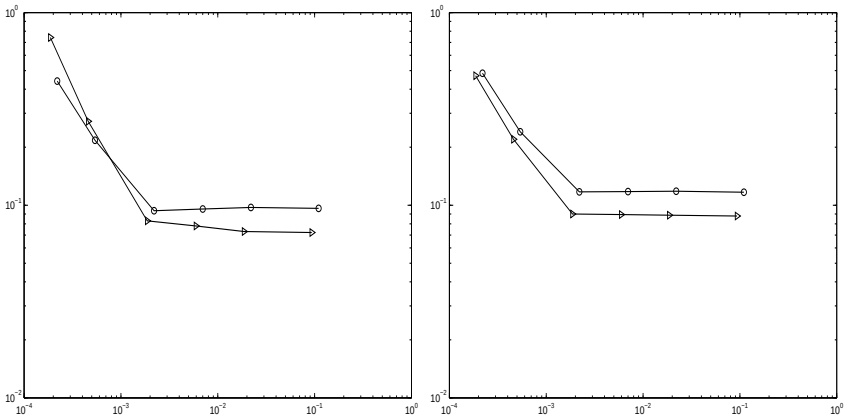

Figure 9: Log-log representation of the relative error on the center with respect to some values of τ, from the discretizations $\mathcal{T}_\alpha^1$ (—o—) and $\mathcal{T}_\alpha^2$ (—▷—), for $\mu_1 = 1$ with $\varepsilon_1 = 3$ (at left) and $\varepsilon_1 = 5$ (at right).

will not be sufficiently accurate.

The behaviours of the relative errors on the radius and the center of the imperfection, with respect to τ, indicate to us moreover that accurate reconstructions of the imperfection cannot be expected in the case of too small or large values of τ.

For $\mu_1 = 1$, $\varepsilon_1 = 3$ we superpose in Figures 10 - 12, for three values of τ, the cross-sections at $x = p_1$, $y = p_2$ and $z = p_3$, of the original imperfection (with center $(p_1, p_2, p_3)^T$) and of the localized imperfection resulting from the discretization $\mathcal{T}_\alpha^1$.

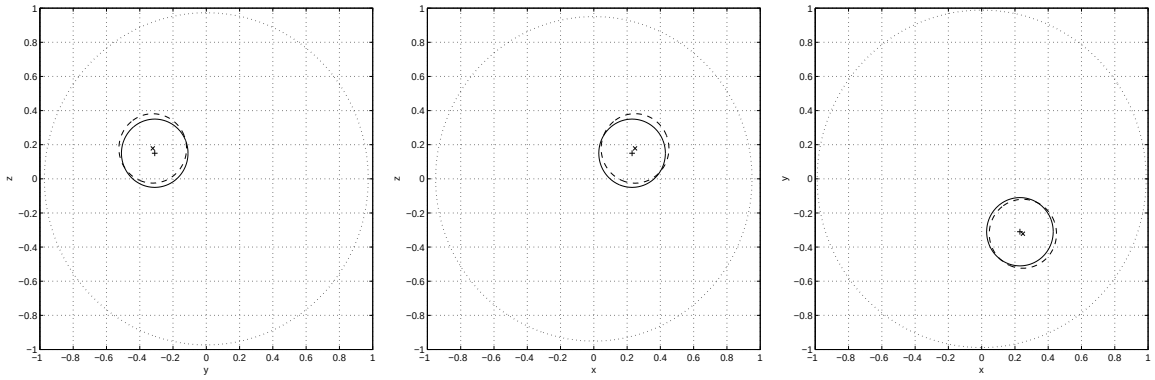

Figure 10: Respective cross-sections at $x = p_1$, $y = p_2$ and $z = p_3$, from the discretization $\mathcal{T}_\alpha^1$ and with $\mu_1 = 1$, $\varepsilon_1 = 3$, $\tau = 2.6\,10^{-1}$. Superposition of the original imperfection (——) whose center is marked by "+", and of the localized imperfection $(- - -)$ with its center marked by "×".

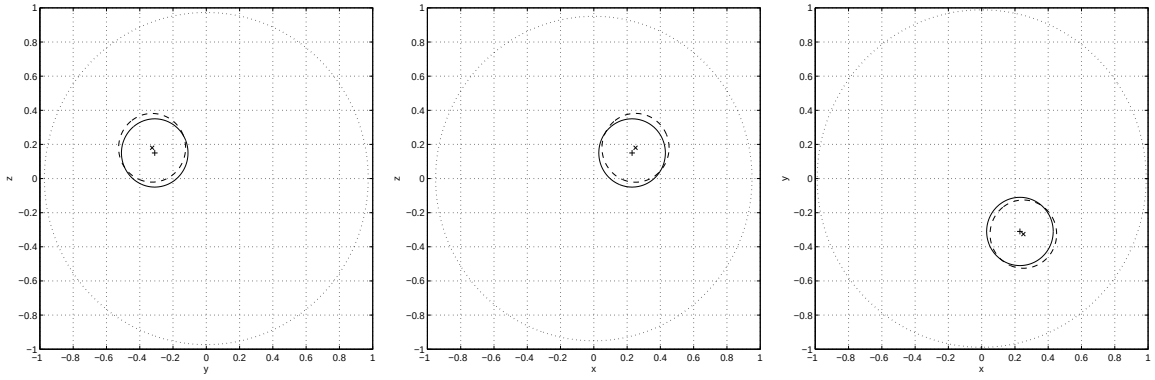

Figure 11: Respective cross-sections at $x = p_1$, $y = p_2$ and $z = p_3$, from the discretization $\mathcal{T}_\alpha^1$ and with $\mu_1 = 1$, $\varepsilon_1 = 3$, $\tau = 2.2\,10^{-2}$. Superposition of the original imperfection (——) whose center is marked by "+", and of the localized imperfection $(- - -)$ with its center marked by "×".

A similar superposition is reproduced in Figures 13 - 15 in the context of the discretization $\mathcal{T}_\alpha^1$ and of the same values of τ (and therefore of the same frequencies) but by considering $\varepsilon_1 = 10$.

In what follows, we use the same frequencies as above, but the values of τ differ from the previous ones as the discretization $\mathcal{T}_\alpha^2$ is now considered. We represent in Figures 16 - 18 the numerical results

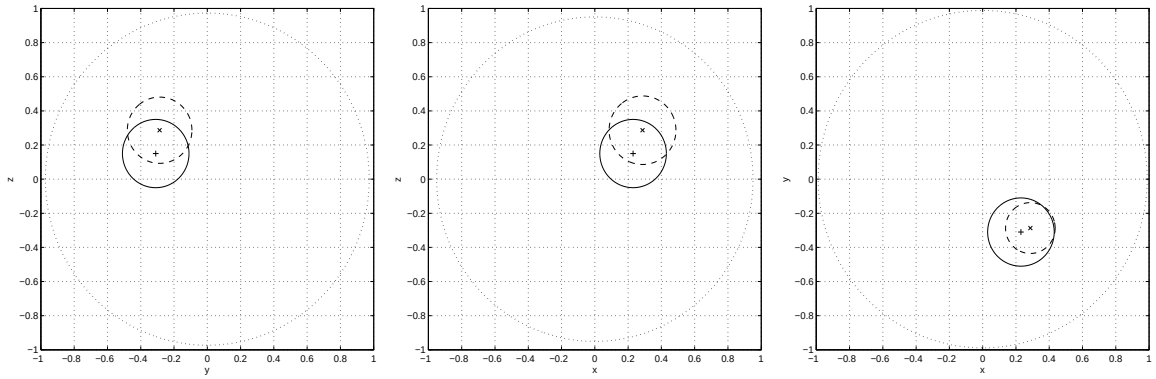

Figure 12: Respective cross-sections at $x = p_1$, $y = p_2$ and $z = p_3$, from the discretization $\mathcal{T}_\alpha^1$ and with $\mu_1 = 1$, $\varepsilon_1 = 3$, $\tau = 2.2\,10^{-4}$. Superposition of the original imperfection (——) whose center is marked by "+", and of the localized imperfection $(- - -)$ with its center marked by "×".

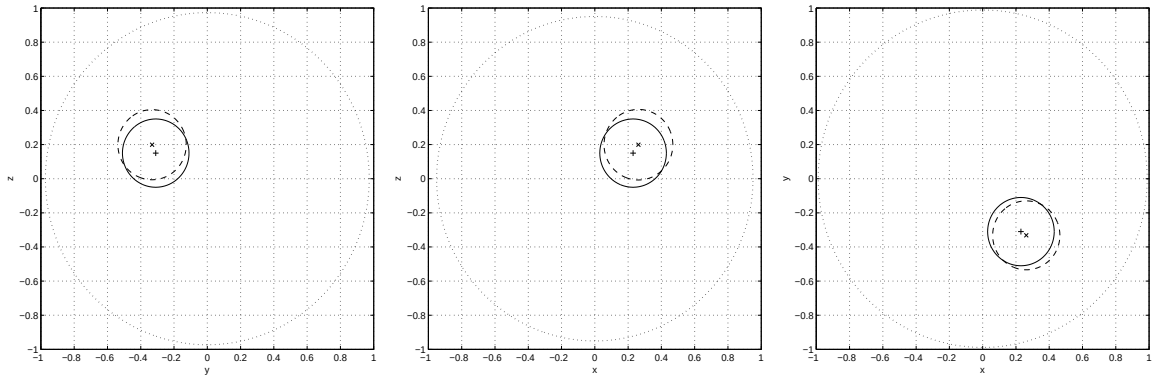

Figure 13: Respective cross-sections at $x = p_1$, $y = p_2$ and $z = p_3$, from the discretization $\mathcal{T}_\alpha^1$ and with $\mu_1 = 1$, $\varepsilon_1 = 10$, $\tau = 2.6\,10^{-1}$. Superposition of the original imperfection (——) whose center is marked by "+", and of the localized imperfection $(- - -)$ with its center marked by "×".

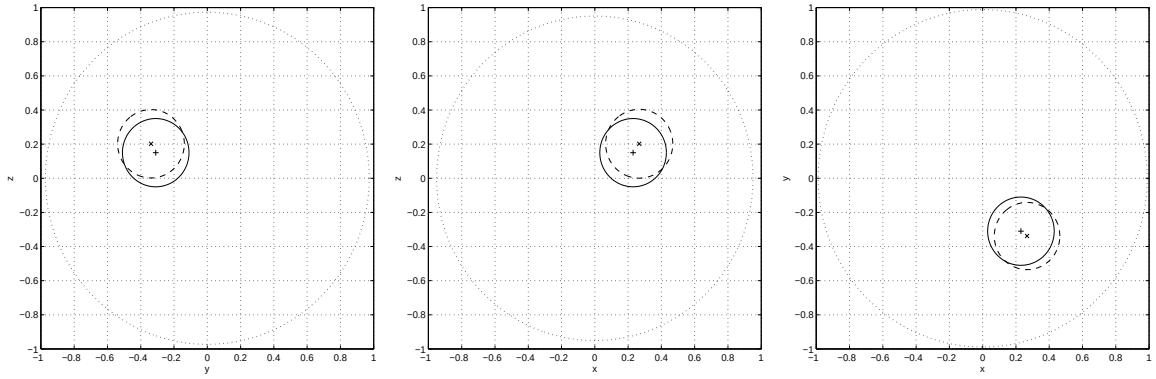

Figure 14: Respective cross-sections at $x = p_1$, $y = p_2$ and $z = p_3$, from the discretization $\mathcal{T}_\alpha^1$ and with $\mu_1 = 1$, $\varepsilon_1 = 10$, $\tau = 2.2\,10^{-2}$. Superposition of the original imperfection (——) whose center is marked by "+", and of the localized imperfection $(- - -)$ with its center marked by "×".

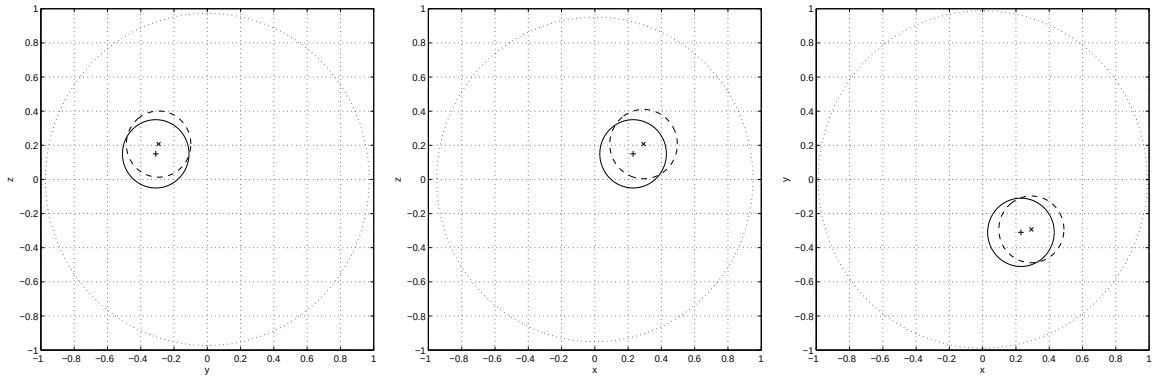

Figure 15: Respective cross-sections at $x = p_1$, $y = p_2$ and $z = p_3$, from the discretization $\mathcal{T}_\alpha^1$ and with $\mu_1 = 1$, $\varepsilon_1 = 10$, $\tau = 2.2\,10^{-4}$. Superposition of the original imperfection (——) whose center is marked by "+", and of the localized imperfection $(- - -)$ with its center marked by "$\times$".

obtained from $\mathcal{T}_\alpha^2$ and with $\mu_1 = 1$, $\varepsilon_1 = 10$. These results concern the localization of a smaller inhomogeneity than previously.

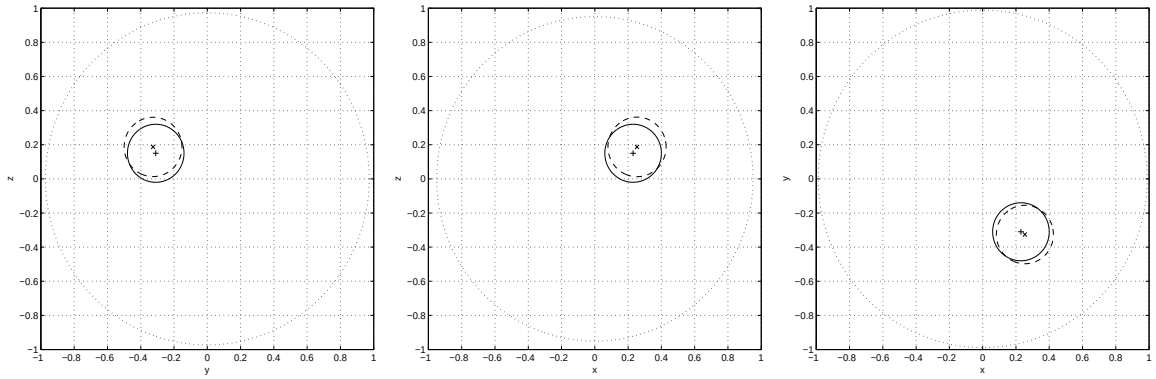

Figure 16: Respective cross-sections at $x = p_1$, $y = p_2$ and $z = p_3$, from the discretization $\mathcal{T}_\alpha^2$ and with $\mu_1 = 1$, $\varepsilon_1 = 10$, $\tau = 2.21\,10^{-1}$. Superposition of the original imperfection (——) whose center is marked by "+", and of the localized imperfection $(- - -)$ with its center marked by "$\times$".

In Figures 19 - 21, we are interested in the localization in the magnetic case. Typically, we take $\mu_1 = 5, 10$, $\varepsilon_1 = 1$, use different values for τ, and consider the discretization $\mathcal{T}_\alpha^2$. The same kind of results as in these figures has been obtained from simulations, with $\mathcal{T}_\alpha^2$ and the same values used for τ as previously, but by taking now $\mu_1 = 3$, $\varepsilon_1 = 1$. As in the case of an electric imperfection, the localization is efficiently achieved here. Also, as expected, for too small or too large values of τ, this localization becomes less accurate.

For a large range of values of the frequency, the reconstructions of the imperfection defined from $\mathcal{T}_\alpha^2$ are better than the ones of the imperfection defined from $\mathcal{T}_\alpha^1$. In fact, the asymptotic formula (15) is numerically more accurate (see e.g. Figures 2 and 6, or Figures 3 and 7) when we use $\mathcal{T}_\alpha^2$ which

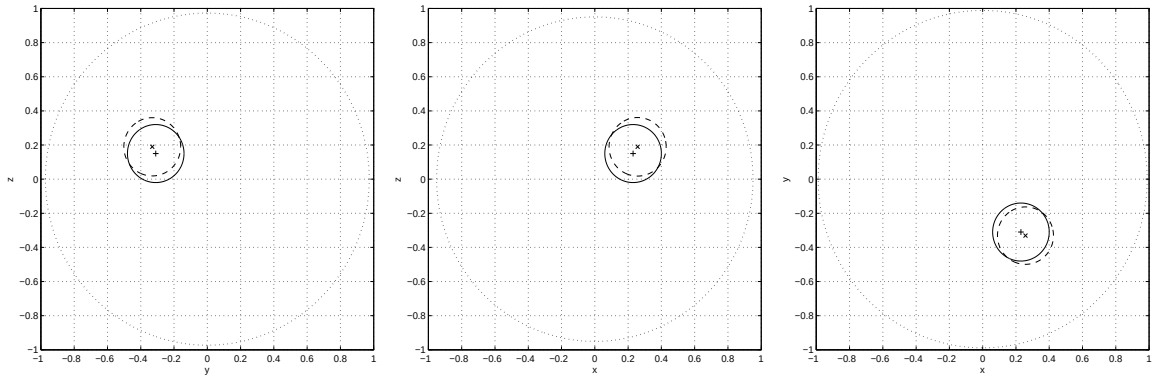

Figure 17: Respective cross-sections at $x = p_1$, $y = p_2$ and $z = p_3$, from the discretization $\mathcal{T}_\alpha^2$ and with $\mu_1 = 1$, $\varepsilon_1 = 10$, $\tau = 1.87\,10^{-2}$. Superposition of the original imperfection (——) whose center is marked by "+", and of the localized imperfection $(- - -)$ with its center marked by "×".

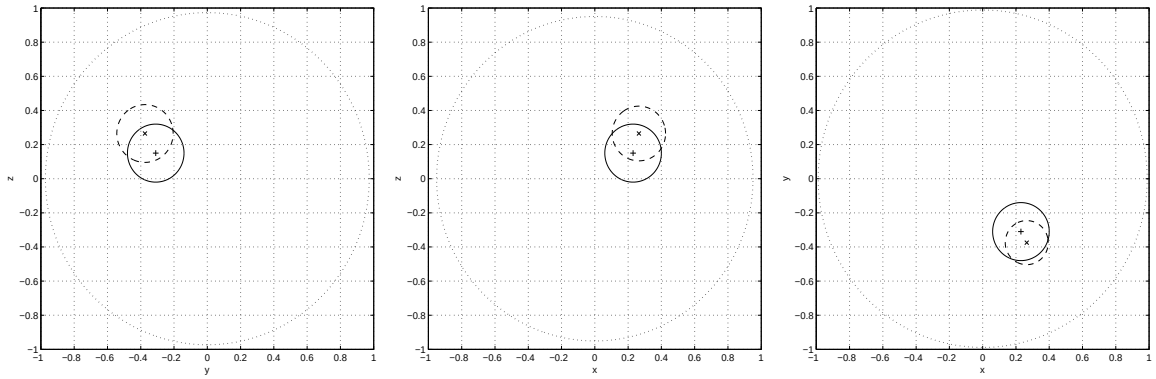

Figure 18: Respective cross-sections at $x = p_1$, $y = p_2$ and $z = p_3$, from the discretization $\mathcal{T}_\alpha^2$ and with $\mu_1 = 1$, $\varepsilon_1 = 10$, $\tau = 1.87\,10^{-4}$. Superposition of the original imperfection (——) whose center is marked by "+", and of the localized imperfection $(- - -)$ with its center marked by "×".

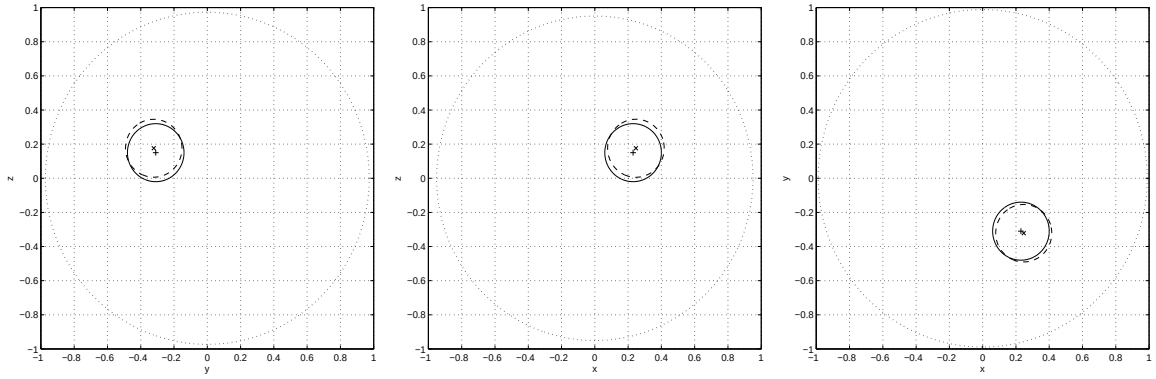

Figure 19: Respective cross-sections at $x = p_1$, $y = p_2$ and $z = p_3$, from the discretization $\mathcal{T}_\alpha^2$ and with $\mu_1 = 5$, $\varepsilon_1 = 1$, $\tau = 2.21\,10^{-1}$. Superposition of the original imperfection (——) whose center is marked by "+", and of the localized imperfection $(- - -)$ with its center marked by "×".

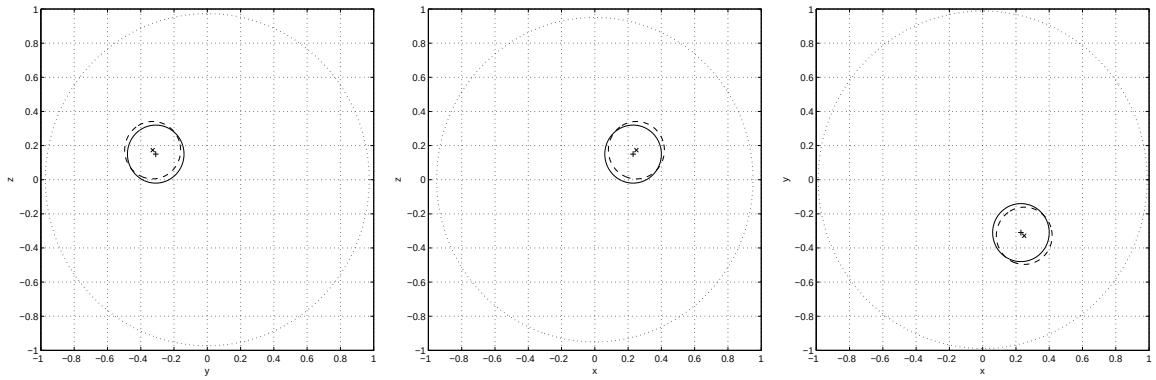

Figure 20: Respective cross-sections at $x = p_1$, $y = p_2$ and $z = p_3$, from the discretization $\mathcal{T}_\alpha^2$ and with $\mu_1 = 5$, $\varepsilon_1 = 1$, $\tau = 9.35\,10^{-2}$. Superposition of the original imperfection (——) whose center is marked by "+", and of the localized imperfection $(- - -)$ with its center marked by "×".

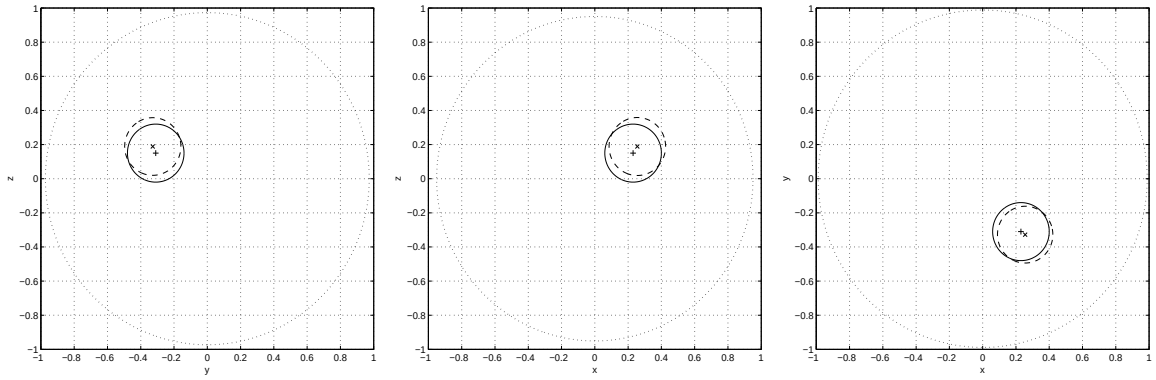

Figure 21: Respective cross-sections at $x = p_1$, $y = p_2$ and $z = p_3$, from the discretization $\mathcal{T}_\alpha^2$ and with $\mu_1 = 10$, $\varepsilon_1 = 1$, $\tau = 2.21\,10^{-1}$. Superposition of the original imperfection (——) whose center is marked by "+", and of the localized imperfection $(- - -)$ with its center marked by "×".

considers an imperfection shaped as the one defined from $\mathcal{T}_\alpha^1$, but having a smaller size.

The case where $\tau \approx 10^{-4}$ appears, following the settings considered here, as a limit case for possible "accurate" reconstructions. It results from simulations elsewhere that, for frequencies that do not lead to such values of τ, the reconstruction of the imperfection seems better in the context of weak contrasts of the domain. More precisely, for $\mu_1 = 1$ (respectively $\varepsilon_1 = 1$), we obtain accurate reconstructions with small values of $|\varepsilon_1|$ (respectively μ_1), at the same chosen frequency, as above (compare e.g. Figures 10 and 13, Figures 11 and 14). This remark was foreseeable from the study achieved in Subsection 6.2. This leads us to think that the asymptotic formula (15) is numerically less accurate in the case of an imperfection for which the value of one of the parameters μ_1 or $|\varepsilon_1|$ is too large, and would not then be suited to an efficient reconstruction of such an imperfection.

6.4 Numerical Localization from the Procedure based on the MUSIC Algorithm

We are concerned in this part with the numerical localization of a finite number m ($m \geq 1$) of imperfections contained in Ω. We present numerical results obtained from extensive simulations that make use of the procedure based on the MUSIC algorithm (see Subsection 5.2). Namely, all the settings introduced in Subsection 6.1 are considered here. Since this procedure requires the visual representation of the functional W_c depending in particular on the parameter c, all our results will be described with respect to c in addition to the parameters τ, μ_α and ε_α. More precisely, as the same procedure enforces an illumination of the domain Ω, these results should be described also with respect to the number n of incident waves used to illuminate Ω. These waves are defined with the help of certain points marked on the boundary of the domain — uniformly distributed on the full boundary and defined as the points θ_l, $1 \leq l \leq n$, in Subsection 6.2. It is now known that n depends on the type of imperfections contained in Ω and on their number m. In a general way and in accordance with Subsection 5.2, we will consider $n = 3m + 2$ incident waves in the case of electric or magnetic imperfections, and $n = 5m + 3$ in the case of the localization of electromagnetic imperfections. In our presentation of results, we will then specify the choice of n only when it differs from $3m + 2$ or $5m + 3$ following the case.

We fix $\mu_0 = \varepsilon_0 = 1$ in this part. In order to compare the numerical results of the previous subsection with those that will be obtained here in the case of the localization of a single imperfection ($m = 1$), we first consider most of the previous values of τ, μ_1 and ε_1, as well as the discretizations $\mathcal{T}_\alpha^1$, $\mathcal{T}_\alpha^2$. Let us recall that the same notation as above, $p = (p_1, p_2, p_3)^T$, is used to indicate the center of this imperfection in each one of its settings.

In Figures 22 - 24 we represent the results of the localization of a single imperfection by considering $\mu_1 = 1$, $\varepsilon_1 = 3$, $\tau = 2.6\,10^{-1}$ and $c = (1.0, 1.0, 3.0)^T$. The choice of the parameter c will always be in accordance with Subsection 5.2, and we already mention that other admissible values for this parameter lead to the same kind of results as here. These results concerning the location of the imperfection derive from the discretization $\mathcal{T}_\alpha^1$ and are similar to those of Figure 10 that were obtained in the previous subsection.

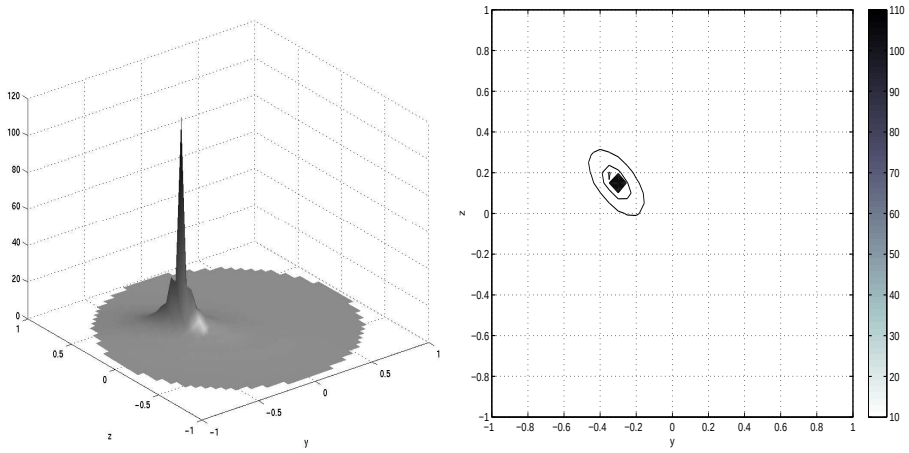

Figure 22: Cross-section of W_c at $x = p_1$ (at left) and corresponding contour-plot (at right), from the discretization $\mathcal{T}_\alpha^1$ and with $\mu_1 = 1$, $\varepsilon_1 = 3$, $\tau = 2.6\,10^{-1}$, $c = (1.0, 1.0, 3.0)^T$.

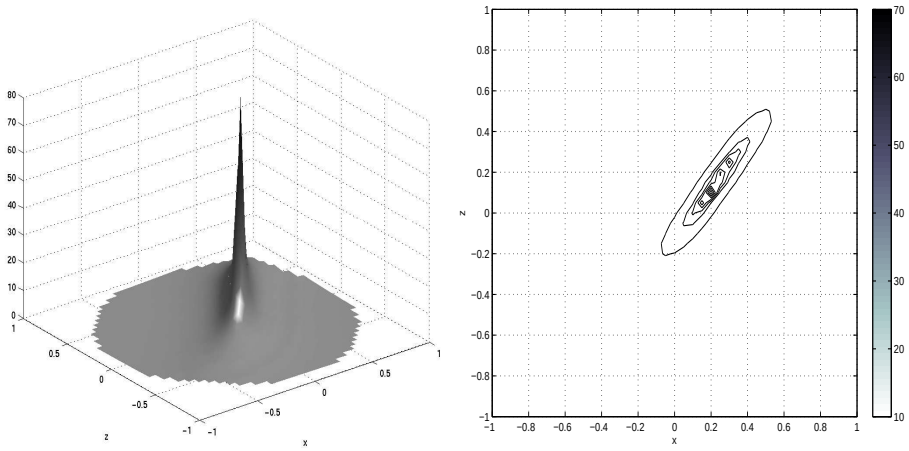

Figure 23: Cross-section of W_c at $y = p_2$ (at left) and corresponding contour-plot (at right), from the discretization $\mathcal{T}_\alpha^1$ and with $\mu_1 = 1$, $\varepsilon_1 = 3$, $\tau = 2.6\,10^{-1}$, $c = (1.0, 1.0, 3.0)^T$.

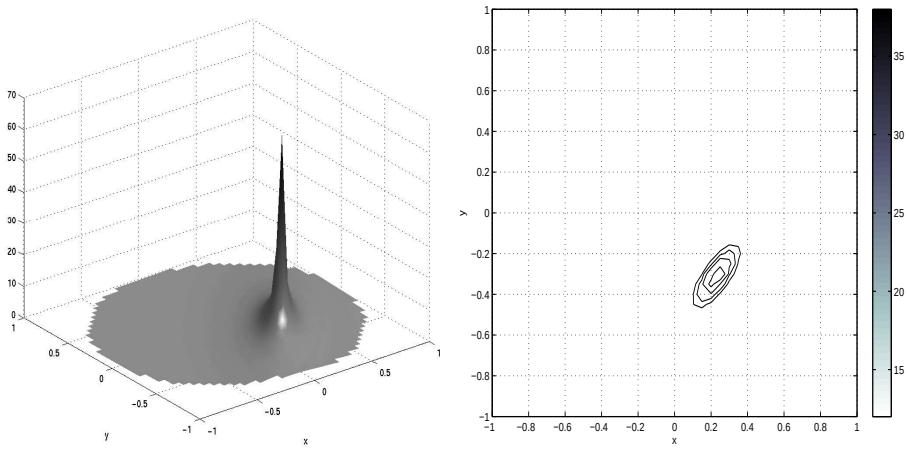

Figure 24: Cross-section of W_c at $z = p_3$ (at left) and corresponding contour-plot (at right), from the discretization $\mathcal{T}_\alpha^1$ and with $\mu_1 = 1$, $\varepsilon_1 = 3$, $\tau = 2.6\,10^{-1}$, $c = (1.0, 1.0, 3.0)^T$.

The results obtained by taking now $\varepsilon_1 = 10$, $\tau = 2.2\,10^{-2}$ are represented in Figure 25, and it also follows in this case that the numerical accuracy of the location of the imperfection is similar to the one of the previous subsection (see Figure 14).

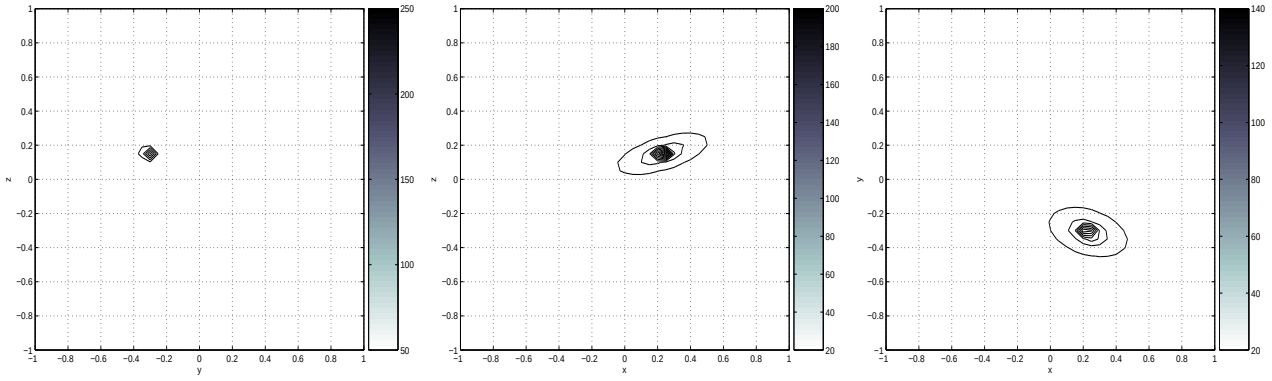

Figure 25: Respective contour-plots of cross-sections of W_c at $x = p_1$, $y = p_2$ and $z = p_3$, from the discretization $\mathcal{T}_\alpha^1$ and with $\mu_1 = 1$, $\varepsilon_1 = 10$, $\tau = 2.2\,10^{-2}$, $c = (-1.0, 5.0, 1.0)^T$.

Contrary to the simulations of the previous subsection where the electromagnetic case has not been taken into account, we consider here the situation where both $\mu_1 \neq \mu_0$ and $\varepsilon_1 \neq \varepsilon_0$.

In Figure 26, we represent the results obtained with $\mu_1 = 5$ and $\varepsilon_1 = 10$, from the discretization $\mathcal{T}_\alpha^1$. The numerical localization of the center of the electromagnetic imperfection is as accurate as for the one of the previous imperfection presented in Figure 25, where the same value of τ is used.

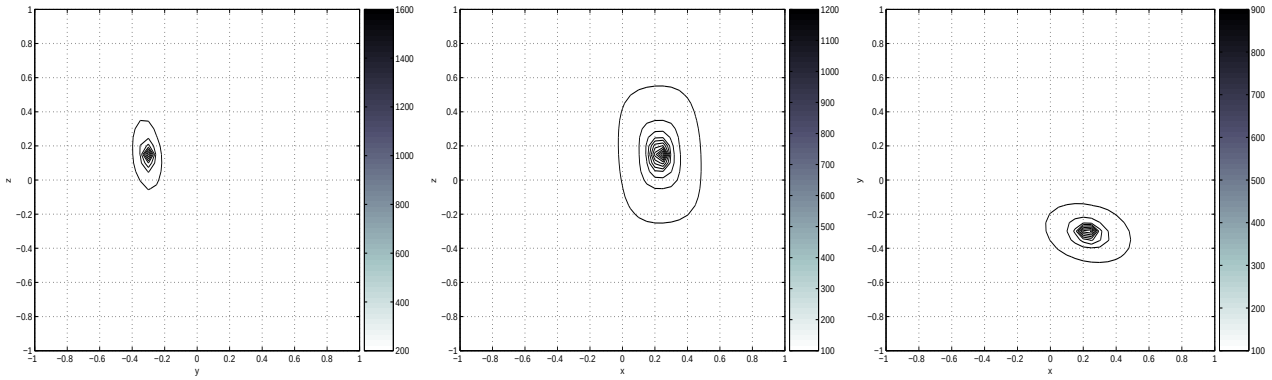

Figure 26: Respective contour-plots of cross-sections of W_c at $x = p_1$, $y = p_2$ and $z = p_3$, from the discretization $\mathcal{T}_\alpha^1$ and with $\mu_1 = 5$, $\varepsilon_1 = 10$, $\tau = 2.2\,10^{-2}$, $c = (1.0, -0.5, 0.5)^T$.

Also, contrary to the simulations of the previous subsection, where a restriction was enforced on the choice of frequencies for reconstructions, the present procedure allows us to achieve localizations in a less restrictive context, namely with 'high' frequencies. The results obtained by considering 'large values' of τ are represented in Figures 27 - 28. It appears, as in Figure 28, that the localization of the center becomes less and less accurate when τ tends to 1; the imperfection appears to split into two parts.

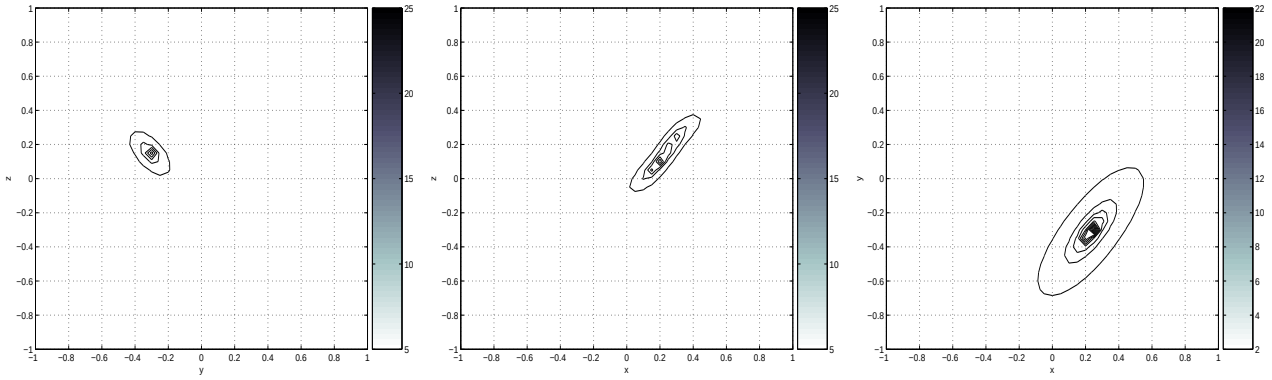

Figure 27: Respective contour-plots of cross-sections of W_c at $x = p_1$, $y = p_2$ and $z = p_3$, from the discretization $\mathcal{T}_\alpha^1$ and with $\mu_1 = 1$, $\varepsilon_1 = 3$, $\tau = 6.6\,10^{-1}$, $c = (1.0, 1.0, 3.0)^T$.

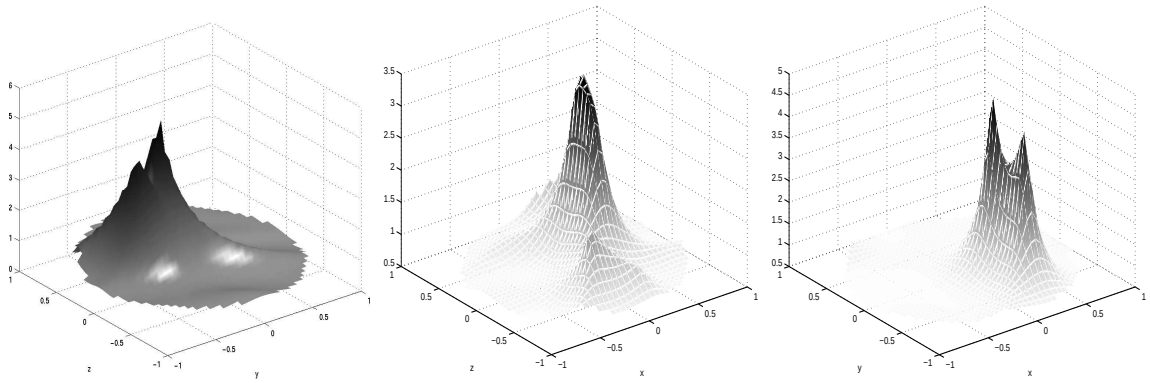

Figure 28: Respective cross-sections of W_c at $x = p_1$, $y = p_2$ and $z = p_3$, from the discretization $\mathcal{T}_\alpha^1$ and with $\mu_1 = 5$, $\varepsilon_1 = 3$, $\tau = 9.6\,10^{-1}$, $c = (1.0, -0.5, 0.5)^T$.

In Figures 29 - 30, we represent the results obtained from the discretization $\mathcal{T}_\alpha^2$, for $\mu_1 = 1,5$ and $\varepsilon_1 = 10$. These results concern the localization of the center of a smaller imperfection than previously.

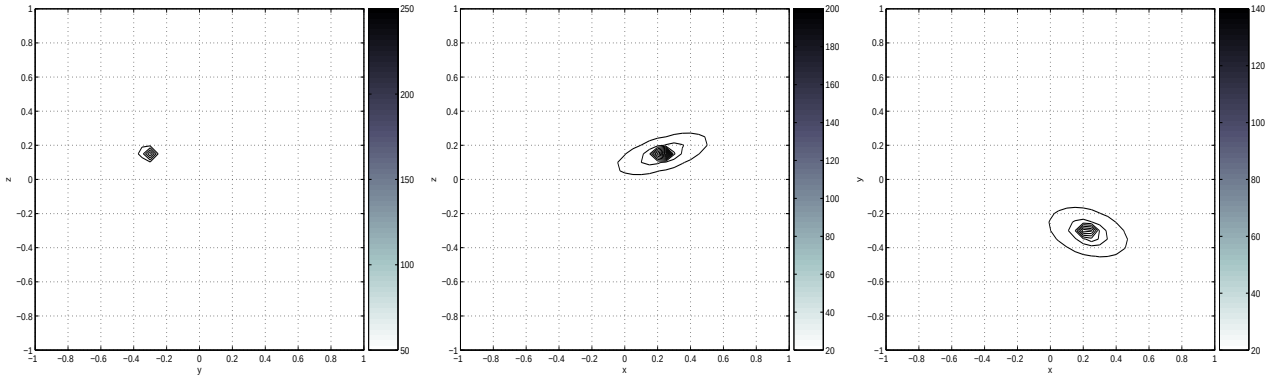

Figure 29: Respective contour-plots of cross-sections of W_c at $x = p_1$, $y = p_2$ and $z = p_3$, from the discretization $\mathcal{T}_\alpha^2$ and with $\mu_1 = 1$, $\varepsilon_1 = 10$, $\tau = 1.87\,10^{-2}$, $c = (-1.0, 5.0, 1.0)^T$.

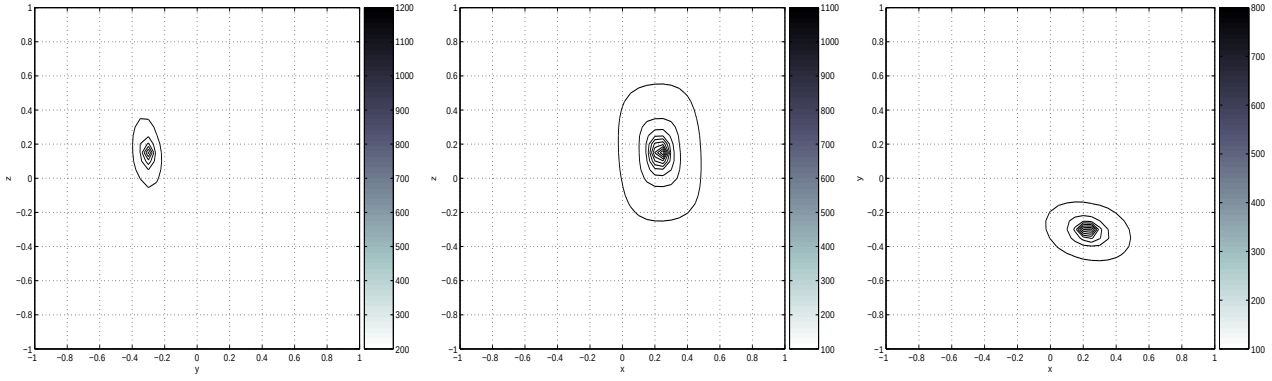

Figure 30: Respective contour-plots of cross-sections of W_c at $x = p_1$, $y = p_2$ and $z = p_3$, from the discretization $\mathcal{T}_\alpha^2$ and with $\mu_1 = 5$, $\varepsilon_1 = 10$, $\tau = 1.87\,10^{-2}$, $c = (1.0, -0.5, 0.5)^T$.

We detail in Figure 31 the distribution of the singular-values of the MSR matrix, in the context of the discretization $\mathcal{T}_\alpha^2$. Independently of the values used there for ε_1, there are 5 significant singular-values for $n = 7$ (or 10) illuminations of the domain.

Let us mention that for too small values of τ, it results from simulations that the numerical localization, considering $\mathcal{T}_\alpha^2$, is disastrous even using a large number of illuminations of the domain.

We now turn to the localization of multiple imperfections in the settings based on the discretizations $\mathcal{T}_\alpha^3$, $\mathcal{T}_\alpha^4$ and $\mathcal{T}_\alpha^5$. Figures 32 - 36 present the results regarding the localization of two imperfections in various aspects.

As in the single imperfection case, it results in fact from simulations that when τ approaches 1 or becomes too small, the localization of the imperfections becomes less and less accurate.

We are concerned in Figures 37 - 42 with the localization of the imperfections when the settings

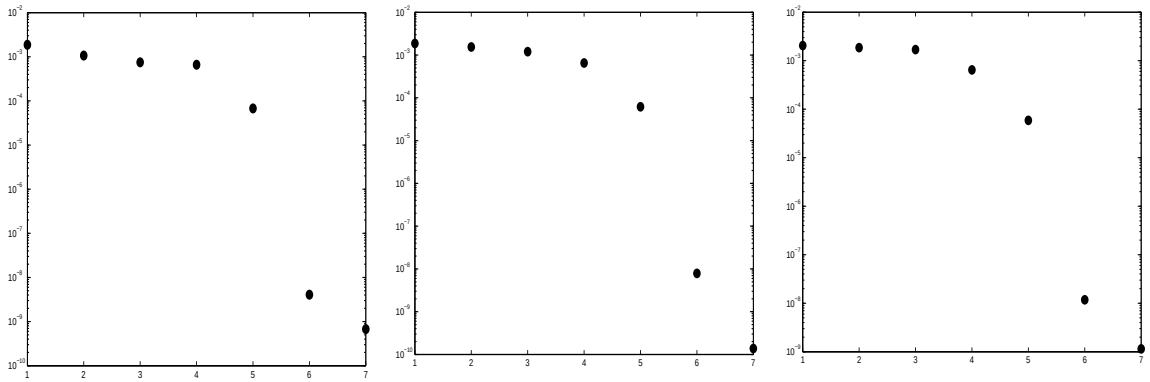

Figure 31: Semi-log representation of the singular-values of the MSR matrix, from the discretization $\mathcal{T}_\alpha^2$ and for $\tau = 1.87\,10^{-2}$, $n = 7$, $\mu_1 = 5$ with $\varepsilon_1 = 3$ (at left), $\varepsilon_1 = 5$ (at middle) and $\varepsilon_1 = 10$ (at right).

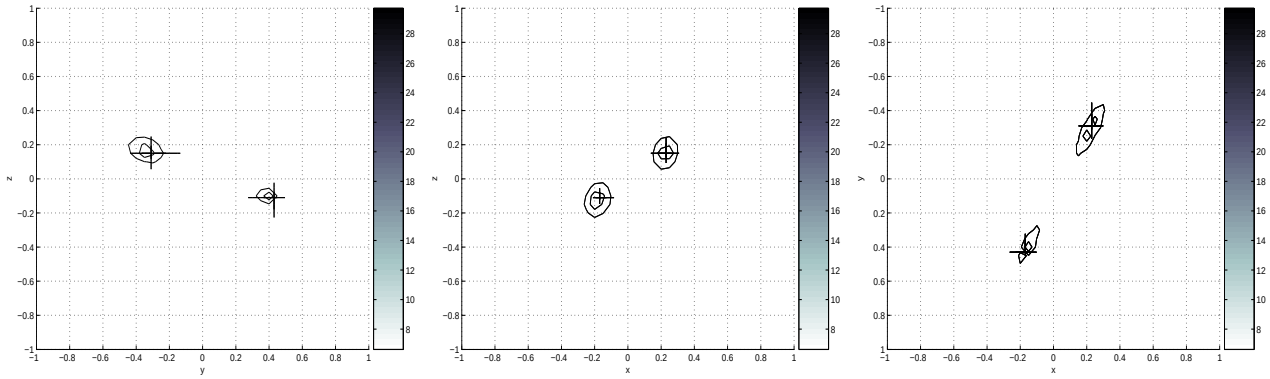

Figure 32: Contour-plot views of W_c from the $x-$direction, the $y-$direction and the $z-$direction respectively, when $\mathcal{T}_\alpha^3$ is used, $\mu_1 = \mu_2 = 1$, $\varepsilon_1 = \varepsilon_2 = 3$, $\tau = 2.6\,10^{-1}$ and $c = (2.0, -1.5, 1.5)^T$.

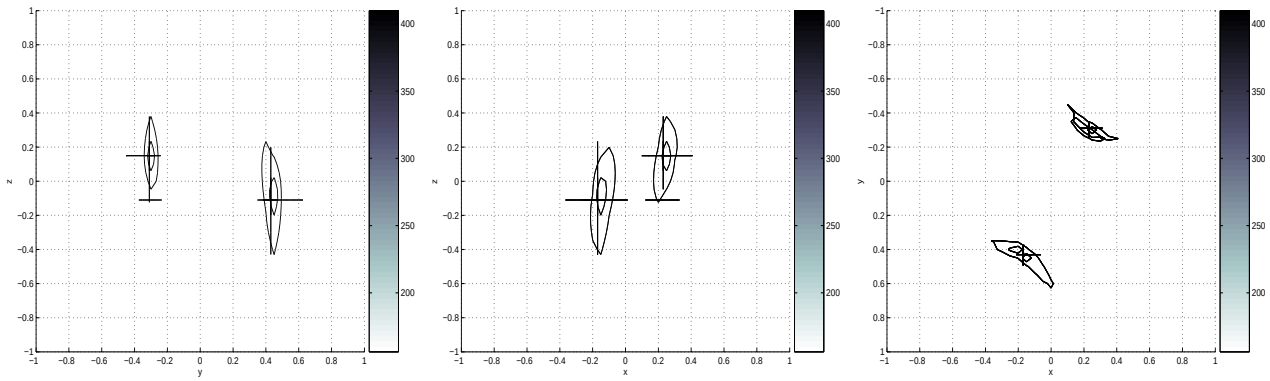

Figure 33: Contour-plot views of W_c from the $x-$direction, the $y-$direction and the $z-$direction respectively, when $\mathcal{T}_\alpha^3$ is used, $\mu_1 = \mu_2 = 5$, $\varepsilon_1 = 5 + 0.5\mathrm{i}, \varepsilon_2 = 5$, $\tau = 2.6\,10^{-1}$ and $c = (3.0, 1.0, -0.5)^T$.

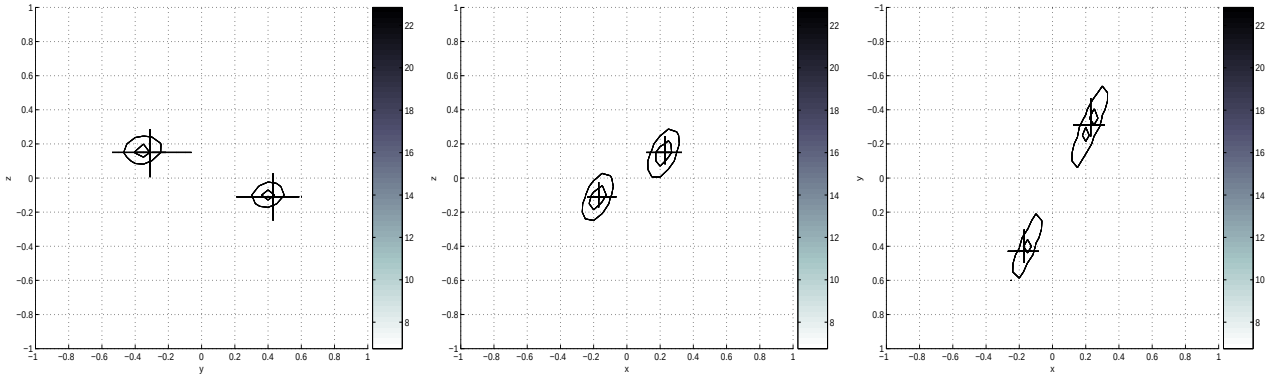

Figure 34: Contour-plot views of W_c from the $x-$direction, the $y-$direction and the $z-$direction respectively, when $\mathcal{T}_\alpha^3$ is used, $\mu_1 = \mu_2 = 1$, $\varepsilon_1 = 10+0.5\mathrm{i}, \varepsilon_2 = 10$, $\tau = 2.6\,10^{-1}$ and $c = (2.0, -1.5, 1.5)^T$.

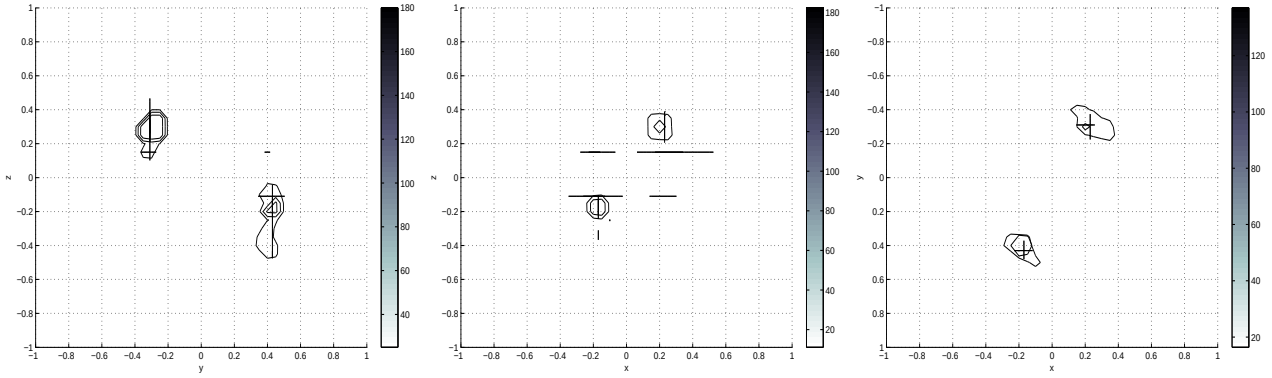

Figure 35: Contour-plot views of W_c from the $x-$direction, the $y-$direction and the $z-$direction respectively, when $\mathcal{T}_\alpha^3$ is used, $\mu_1 = \mu_2 = 5$, $\varepsilon_1 = 5+0.5\mathrm{i}, \varepsilon_2 = 5$, $\tau = 6.6\,10^{-1}$ and $c = (3.0, 1.0, -0.5)^T$.

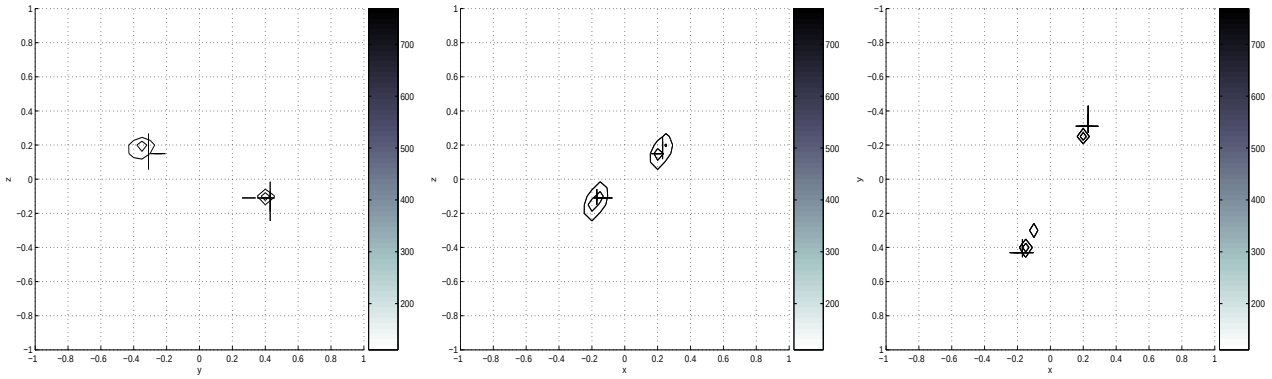

Figure 36: Contour-plot views of W_c from the $x-$direction, the $y-$direction and the $z-$direction respectively, when $\mathcal{T}_\alpha^3$ is used, $\mu_1 = \mu_2 = 1$, $\varepsilon_1 = 10+0.5\mathrm{i}, \varepsilon_2 = 10$, $\tau = 2.2\,10^{-2}$ and $c = (2.0, -1.5, 1.5)^T$.

based on $\mathcal{T}_\alpha^4$ and $\mathcal{T}_\alpha^5$ are considered. Independently of these settings, we use the same frequencies as above to attempt to locate the imperfections.

The results represented in Figures 37 - 38 have been obtained with a unique choice of values of the parameters ω, μ_α and ε_α, but from different settings.

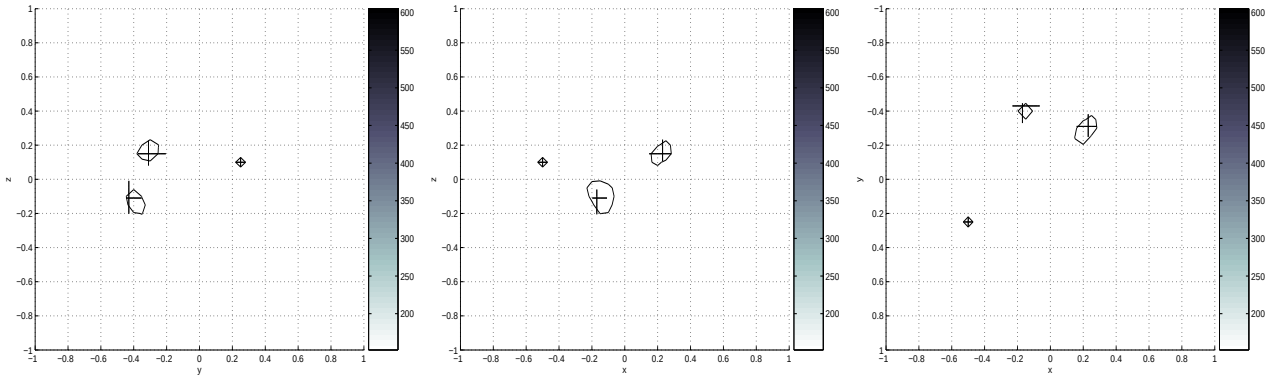

Figure 37: Contour-plot views of W_c from the $x-$direction, the $y-$direction and the $z-$direction respectively, when $\mathcal{T}_\alpha^4$ is used, $\mu_j = 1$, $\varepsilon_j = 3$ $(1 \leq j \leq 3)$, $\tau = 2.34\,10^{-1}$ and $c = (3.0, 2.5, 3.0)^T$.

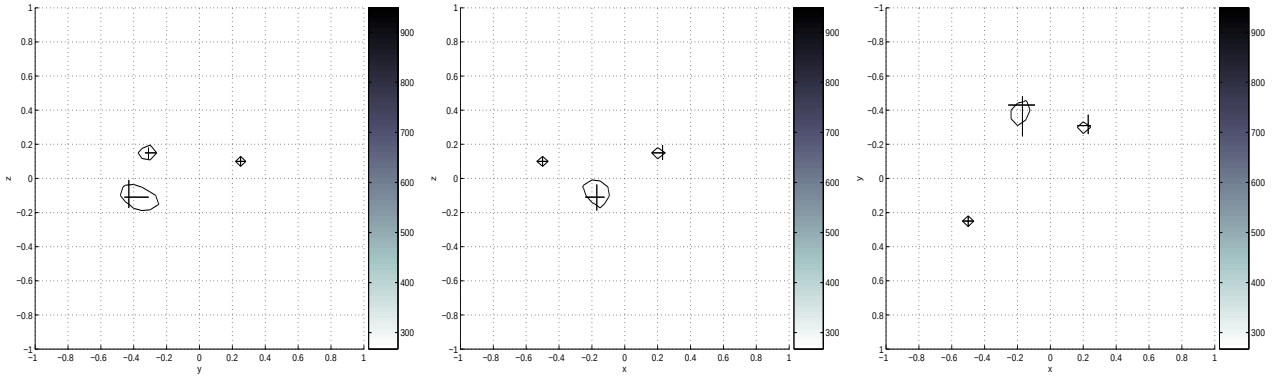

Figure 38: Contour-plot views of W_c from the $x-$direction, the $y-$direction and the $z-$direction respectively, when $\mathcal{T}_\alpha^5$ is used, $\mu_j = 1$, $\varepsilon_j = 3$ $(1 \leq j \leq 3)$, $\tau = 2.47\,10^{-1}$ and $c = (2.0, 0.5, 3.0)^T$.

Keeping the same values of μ_α, ε_α as above, and using now a higher frequency than previously, we obtain the results represented in Figures 39 - 40 which allow us to notice that the localization of the imperfections is again efficiently enough achieved.

In the two last figures of this subsection, we inspect the influence of too small and large values of the parameter τ on the localization regarding the settings $\mathcal{T}_\alpha^4$, $\mathcal{T}_\alpha^5$, as well as the influence of the parameters μ_α and ε_α on this localization. Namely for Figure 41, the parameters μ_α, ε_α are fixed and τ takes different values among which one large and one small, whereas for Figure 42, τ is fixed and μ_α, ε_α vary.

Let us now conclude this subsection by summarizing that the localization of the imperfections from the procedure based on the MUSIC approach is efficiently achieved when too small or large values of τ

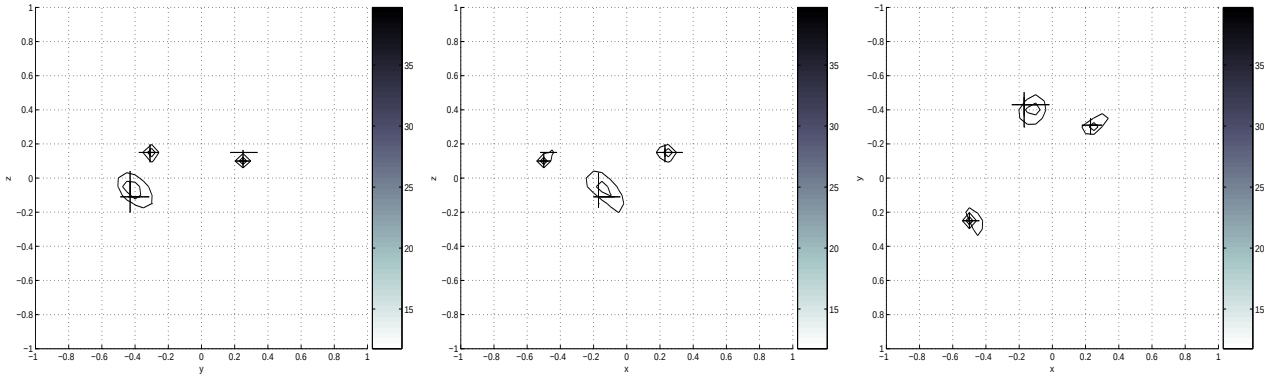

Figure 39: Contour-plot views of W_c from the $x-$direction, the $y-$direction and the $z-$direction respectively, when $\mathcal{T}_\alpha^4$ is used, $\mu_j = 1$, $\varepsilon_j = 3$ $(1 \leq j \leq 3)$, $\tau = 5.94\,10^{-1}$ and $c = (3.0, 2.5, 3.0)^T$.

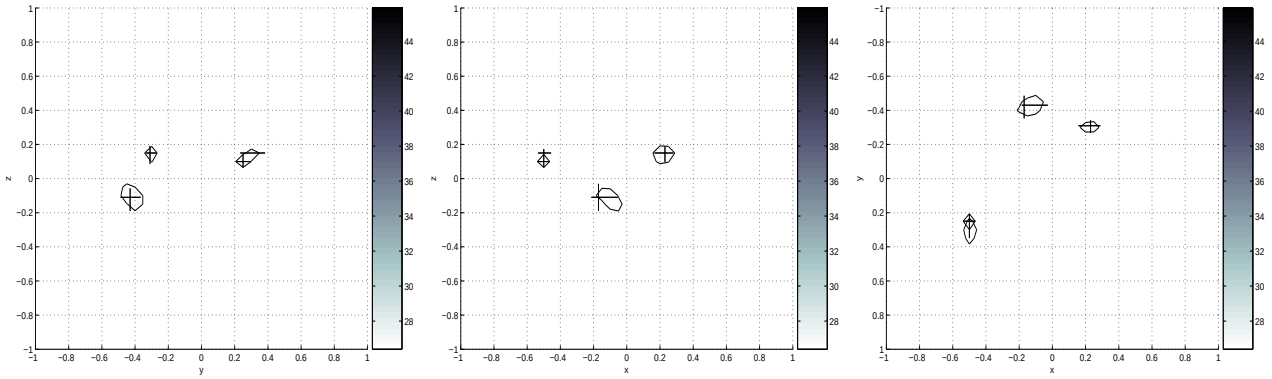

Figure 40: Contour-plot views of W_c from the $x-$direction, the $y-$direction and the $z-$direction respectively, when $\mathcal{T}_\alpha^5$ is used, $\mu_j = 1$, $\varepsilon_j = 3$ $(1 \leq j \leq 3)$, $\tau = 6.27\,10^{-1}$ and $c = (2.0, 0.5, 3.0)^T$.

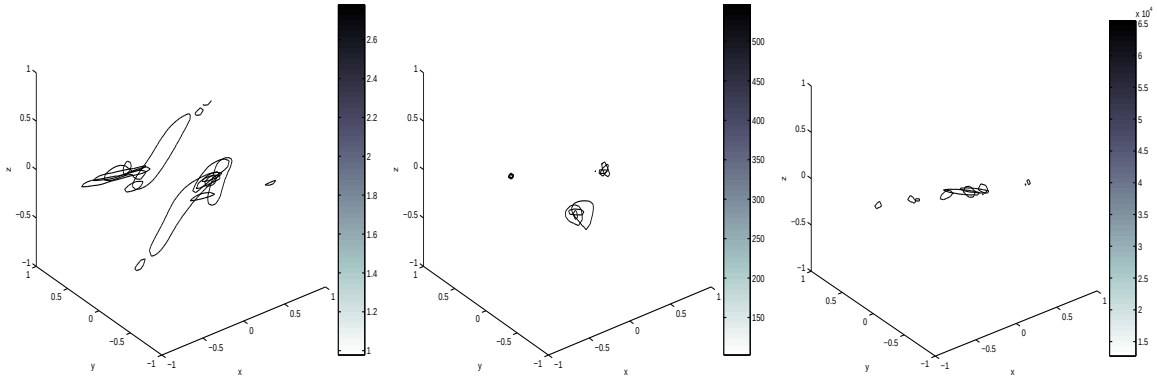

Figure 41: Contour-plot views of W_c when $\mathcal{T}_\alpha^4$ is used, $\mu_j = 1$, $\varepsilon_j = 10$ $(1 \leq j \leq 3)$, $c = (4.0, 2.0, 5.0)^T$, with $\tau = 9.54\,10^{-1}$ at left, $\tau = 2.34\,10^{-1}$ at middle and $\tau = 1.98\,10^{-4}$ at right.

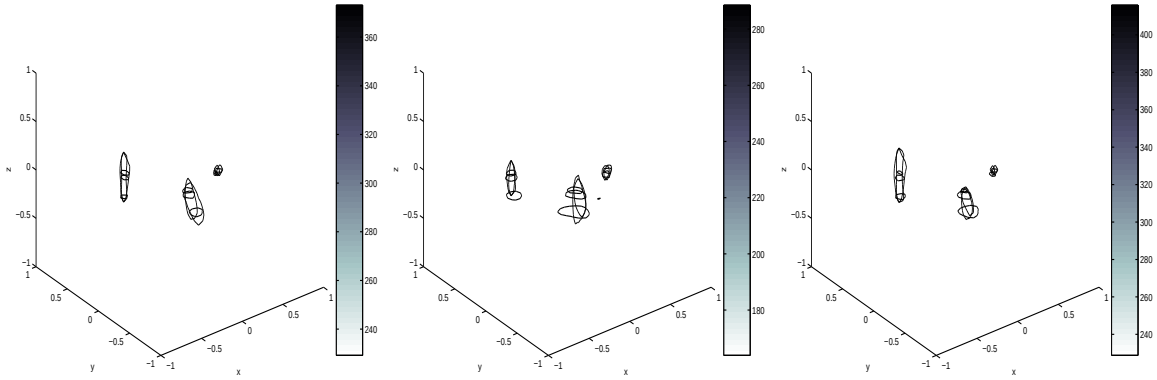

Figure 42: Contour-plot views of W_c when $\mathcal{T}_\alpha^5$ is used, $\tau = 6.27\,10^{-1}$, $c = (-4.0, -1.0, 0.5)^T$, with $\mu_j = 3$, $\varepsilon_j = 10$ at left, $\mu_j = 5$, $\varepsilon_j = 3$ at middle, and $\mu_j = 5$, $\varepsilon_j = 5$ at right, $1 \leq j \leq 3$.

are not considered. It also appears here that the accuracy of the localization varies with respect to the contrast of the domain. In particular, the localization in the case where the domain contains uniquely the imperfections for which $\mu_j = \mu_0$, $\varepsilon_j \neq \varepsilon_0$ $(1 \leq j \leq m)$ is more accurate than the localization in the other cases (this was foreseeable from the study of Subsection 6.2).

6.5 Numerical Localization from the Procedure based on an Inverse Fourier Method

This last subsection also deals with the localization of a finite number m $(m \geq 1)$ of imperfections contained in Ω. We use here the procedure based on an inverse Fourier method (see Subsection 5.3) to perform numerical simulations in each one of the configurations where $m = 1$ or $m > 1$. The present localization procedure enforces an illumination of the domain Ω from a sampling in the Fourier space that provides a corresponding discrete Fourier domain, encapsulated by $[-\eta_{\max}, \eta_{\max}]^3$. Of course, n^3 points constitute this discrete domain, and from each point, an incident wave is generated for illuminating Ω. A boundary measurement associated with this wave is then numerically evaluated through finite element computations, and in total we obtain n^3 numerical sampled measurements that are in fact the data of the procedure. The sequence of modules of the terms that approximate those of (31), following the asymptotic formula, is the outcome of the procedure. The presentation of our results will consist here of representing, after a rescaling by $-\frac{1}{2}$, contour-plots based on this sequence, additionally enriched by a usual linear interpolation process.

According to Subsection 5.3 we should consider large values of $\eta_{\max}$ in the simulations in order to expect accurate localizations. However, a direct application of our procedure with an arbitrarily large value of $\eta_{\max}$ leads to disastrous localizations due to numerical instabilities. Typically, with a large fixed value of $\eta_{\max}$, for each $\eta \in [-\eta_{\max}, \eta_{\max}]^3$ such that $\|\eta\|$ is large and hence the coefficient γ (introduced in Subsection 5.3) has a non-zero imaginary part, the norms of the background potential E_0 and of the test field w used in (26) become too large or too small as compared to their norms for $\|\eta\|$ near 0. The magnitude of the remainder term of (27) then becomes very large in this case of high values of $\|\eta\|$ when compared, for $\|\eta\|$ near 0, to the magnitude of the right-hand side of (29), or to the

magnitude of (30), thus inducing numerical instabilities in the procedure. We already mention that we cannot get rid of these instabilities by a consideration of high wave numbers causing γ to have a zero imaginary part for $\eta \in [-\eta_{\max}, \eta_{\max}]^3$. Of course, such wave numbers correspond to high frequencies, for which the potentials become highly oscillatory, and enforce the use of high values of the parameter τ in the simulations. In fact, the results of simulations of Subsection 6.2 have already showed that the numerical accuracy of the asymptotic formula is bad for such data.

A way to overcome these instabilities is to consider the cutoff process summarized in a two-dimensional situation by D. Volkov in [24]. In this process, a threshold $\eta_\star$ (independent of the centers and shapes of imperfections as well as of μ_j, ε_j, $1 \leq j \leq m$) is introduced such that for $\|\eta\| > \|(\eta_\star, \eta_\star, \eta_\star)^T\|$, the quantity in (30) is set equal to 0. We incorporate this process in our procedure by requiring finer grids for η in order to compensate the induced loss of accuracy. In addition to the physical parameters μ_α, ε_α and τ, all our numerical results will be then described with respect to $\eta_{\max}$, n and $\eta_\star$.

Hereafter, we have two aims: compare the numerical results of Subsections 6.3 and 6.4 with those that will be obtained here in the case of the localization of a single imperfection ($m = 1$) and on the other hand, compare the results of Subsection 6.4 with those that will be described here in the case of the localization of multiple imperfections ($m > 1$). In all cases we fix $\mu_0 = \varepsilon_0 = 1$ and the choices of $\eta_\star$ will result from numerical experiments.

In Figures 43 - 45 we represent the results of the localization of a single imperfection, in each one of the settings defined from $\mathcal{T}_\alpha^1$ and $\mathcal{T}_\alpha^2$, by using most of the values of μ_1, ε_1, τ considered in Subsections 6.3 and 6.4. For each experiment, we fix $\eta_{\max} = 10$ and consider $\rho = 2$ as the step size for sampling, i.e. $n = 10$. We expect then an order of resolution $\frac{\pi}{2\eta_{\max}} \approx 0.157$. This fixed value of $\eta_{\max}$ appears numerically large since, when $\eta_{\max} \geq 8$, we observe in experiments that the magnitude of the remainder term of (27) is very large for each η such that $\|\eta\|$ is near $\eta_{\max}$.

The results of Figure 43 derive from $\mathcal{T}_\alpha^1$ and show that the localization of the imperfection is successfully achieved (and with good numerical accuracy). For the same values of parameters $\eta_{\max}$, n, $\eta_\star$, μ_1 used here, but with $\varepsilon_1 = 10$, $\tau = 2.2\,10^{-2}$, we obtain similar results from simulations based again on $\mathcal{T}_\alpha^1$.

Figure 44 indicates that the localization of a smaller imperfection is also achieved with good numerical accuracy. Similar results have been obtained from simulations, also based on $\mathcal{T}_\alpha^2$, for the same values of parameters $\eta_{\max}$, n, $\eta_\star$ but by taking now $\varepsilon_1 = 10$, $\tau = 1.87\,10^{-2}$.

Figure 45 allows us to notice that the localization of a single imperfection in the electromagnetic case is also efficiently achieved.

Although the results presented above are very accurate — having in mind the order of resolution fixed here by the choice of $\eta_{\max}$, it turns out that for the single imperfection configuration, the present localization procedure is less efficient than the one based on the Current Projection method or than the one deriving from the MUSIC approach. Typically, a very large number of numerical measurements is

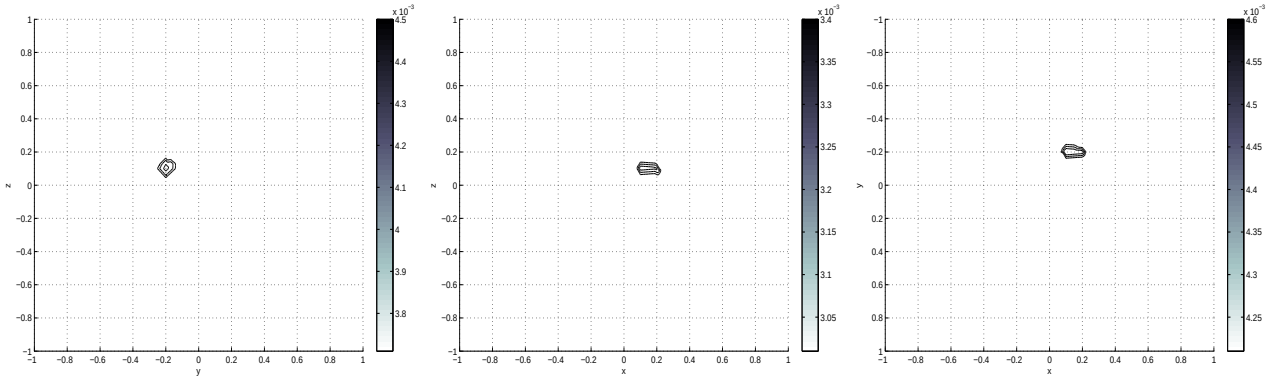

Figure 43: Contour-plot views respectively from the $x-$direction, the $y-$direction and the $z-$direction, based on the enriched sequence, deriving from one of the modules of the terms in (31). Here, $\mathcal{T}_\alpha^1$ is used, $\mu_1 = 1$, $\varepsilon_1 = 3$, $\tau = 2.6\,10^{-1}$, $\eta_{\max} = 10$, $n = 10$ and $\eta_\star = 4$.

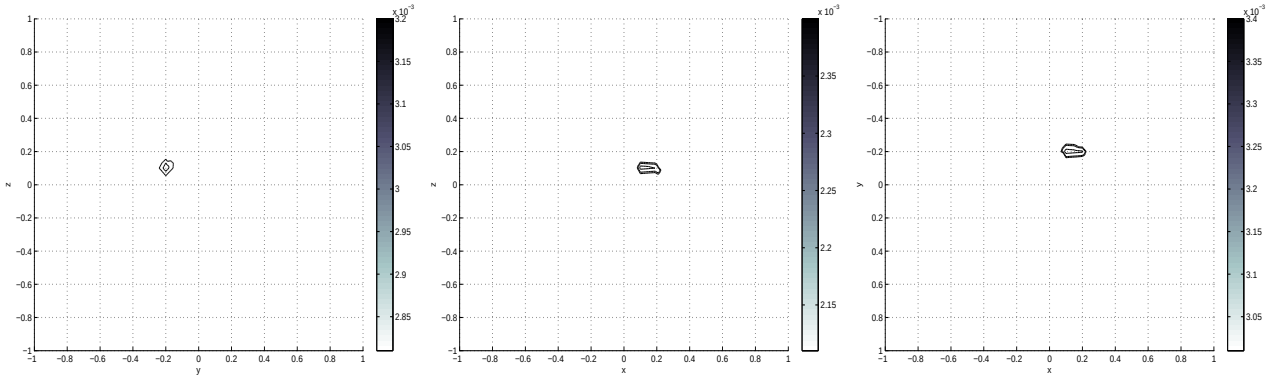

Figure 44: Contour-plot views respectively from the $x-$direction, the $y-$direction and the $z-$direction, based on the enriched sequence, deriving from one of the modules of the terms in (31). Here, $\mathcal{T}_\alpha^2$ is used, $\mu_1 = 1$, $\varepsilon_1 = 3$, $\tau = 2.21\,10^{-1}$, $\eta_{\max} = 10$, $n = 10$ and $\eta_\star = 4$.

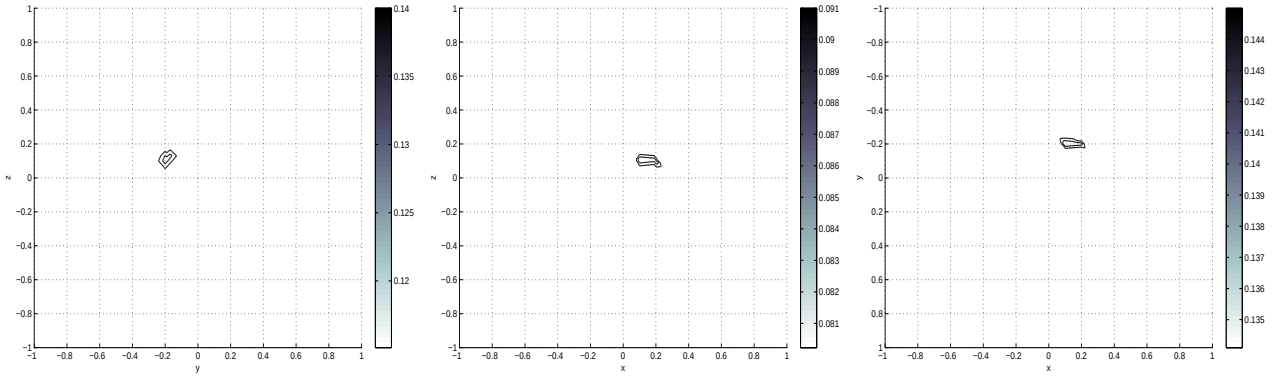

Figure 45: Contour-plot views respectively from the $x-$direction, the $y-$direction and the $z-$direction, based on the enriched sequence, deriving from one of the modules of the terms in (31). Here, $\mathcal{T}_\alpha^2$ is used, $\mu_1 = 5$, $\varepsilon_1 = 10$, $\tau = 1.87\,10^{-2}$, $\eta_{\max} = 10$, $n = 10$ and $\eta_\star = 4$.

required by the present procedure, even for an order of resolution which is not very small. On the other hand, in comparison with the results of Figure 10 (obtained from the Current Projection method) or with those of Figures 22 - 24 (from the MUSIC approach), those presented here in Figure 43, from a same physical context, are less accurate. The same observation is reported in other situations, for example in the electromagnetic case when we compare the results of Figure 30 (from the MUSIC approach) with those presented here by Figure 45.

Let us now inspect the present procedure in the configuration of multiple imperfections. Our experiments are based here on the settings defined from $\mathcal{T}_\alpha^3$, $\mathcal{T}_\alpha^4$ and $\mathcal{T}_\alpha^5$. We keep the same fixed value for $\eta_{\max}$ and expect the same order of resolution as before. Depending on the case, we will consider for sampling $\rho = 2$ or $\frac{5}{4}$ as the step size. Here again, the choices of $\eta_\star$ will result from experiments. We also use most of the values of μ_α, ε_α, τ considered in Subsection 6.4.

In Figures 46 - 48 we represent the results of the localization of two imperfections obtained in different cases, after taking $\rho = 2$. The localization associated with Figure 47 is achieved at the same frequency as for the experiment associated with Figure 46, but concerns electromagnetic imperfections.

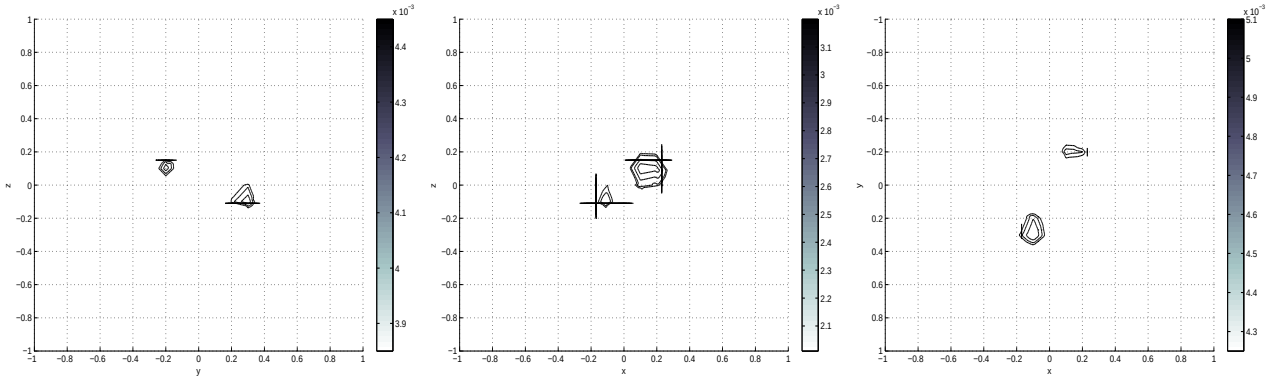

Figure 46: Contour-plot views respectively from the $x-$direction, the $y-$direction and the $z-$direction, based on the enriched sequence, deriving from one of the modules of the terms in (31). Here, $\mathcal{T}_\alpha^3$ is used, $\mu_1 = \mu_2 = 1$, $\varepsilon_1 = \varepsilon_2 = 3$, $\tau = 2.6\,10^{-1}$, $\eta_{\max} = 10$, $n = 10$ and $\eta_\star = 4$.

A localization similar to the one presented by Figure 48 has been obtained from simulations based again on $\mathcal{T}_\alpha^3$, with the same choice of parameters μ_j, ε_j, $\eta_{\max}$, n, but by taking $\eta_\star = 3$ and $\tau = 2.2\,10^{-2}$.

An inspection of these results reveals that the localization based on the setting defined from $\mathcal{T}_\alpha^3$ is successfully achieved, namely with a good numerical accuracy (according to the fixed order of resolution), and by using the same number of measurements as in the single imperfection configuration.

We are hereafter interested in experiments based on the settings $\mathcal{T}_\alpha^4$ and $\mathcal{T}_\alpha^5$. For these experiments, we consider $\rho = \frac{5}{4}$ and are led to use a bigger number of measurements than previously. Figures 49 - 53 present the results of the localization of three imperfections in various aspects.

We deal first with the configuration $\mathcal{T}_\alpha^4$ in the electric case. Namely, the results of Figures 49 - 50 present the localizations achieved at the same frequency and with a unique choice of values of the

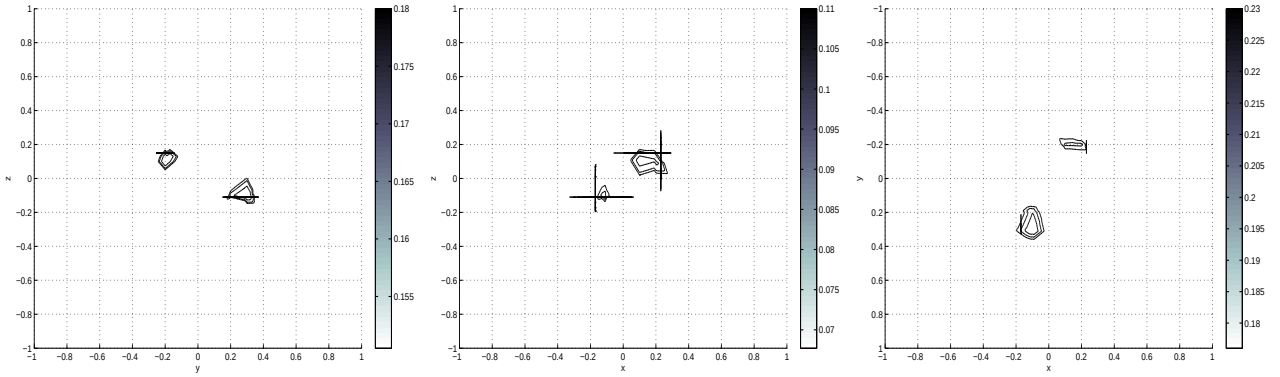

Figure 47: Contour-plot views respectively from the $x-$direction, the $y-$direction and the $z-$direction, based on the enriched sequence, deriving from one of the modules of the terms in (31). Here, $\mathcal{T}_\alpha^3$ is used, $\mu_1 = \mu_2 = 5$, $\varepsilon_1 = 5 + 0.5\mathrm{i}, \varepsilon_2 = 5$, $\tau = 2.6\,10^{-1}$, $\eta_{\max} = 10$, $n = 10$ and $\eta_\star = 4$.

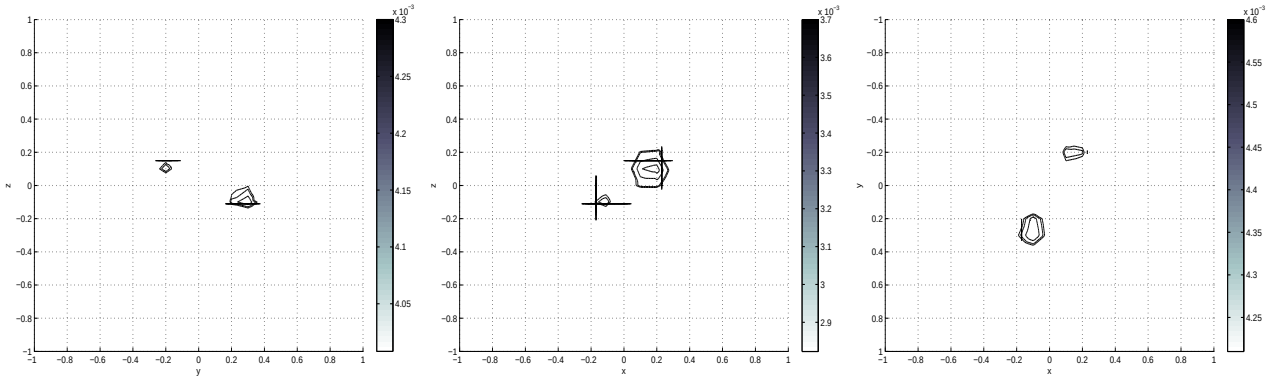

Figure 48: Contour-plot views respectively from the $x-$direction, the $y-$direction and the $z-$direction, based on the enriched sequence, deriving from one of the modules of the terms in (31). Here, $\mathcal{T}_\alpha^3$ is used, $\mu_1 = \mu_2 = 1$, $\varepsilon_1 = 10 + 0.5\mathrm{i}$, $\varepsilon_2 = 10$, $\tau = 2.6\,10^{-1}$, $\eta_{\max} = 10$, $n = 10$ and $\eta_\star = 4$.

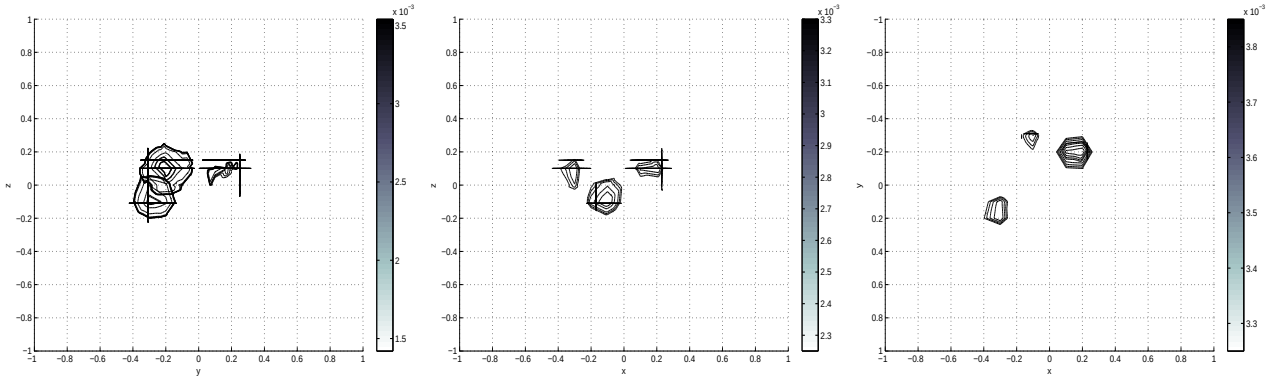

Figure 49: Contour-plot views respectively from the $x-$direction, the $y-$direction and the $z-$direction, based on the enriched sequence, deriving from one of the modules of the terms in (31). Here, $\mathcal{T}_\alpha^4$ is used, $\mu_j = 1$, $\varepsilon_j = 3$ $(1 \leq j \leq 3)$, $\tau = 2.34\,10^{-1}$, $\eta_{\max} = 10$, $n = 16$ and $\eta_\star = 4$.

parameters $\eta_{\max}$, n, $\eta_\star$, but for different values of the electric permittivity.

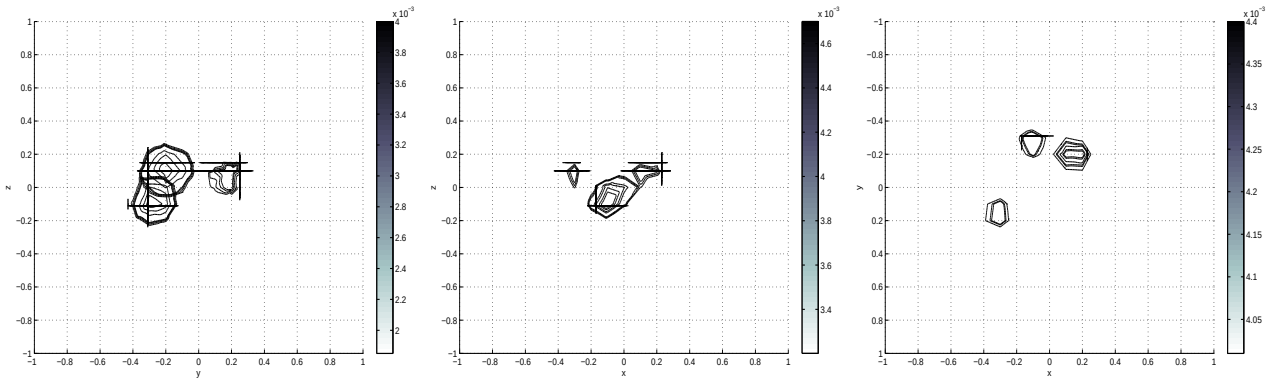

Figure 50: Contour-plot views respectively from the $x-$direction, the $y-$direction and the $z-$direction, based on the enriched sequence, deriving from one of the modules of the terms in (31). Here, $\mathcal{T}_\alpha^4$ is used, $\mu_j = 1$, $\varepsilon_j = 10$ $(1 \leq j \leq 3)$, $\tau = 2.34\,10^{-1}$, $\eta_{\max} = 10$, $n = 16$ and $\eta_\star = 4$.

By using the frequency and the values of the parameters fixed in the experiment associated with Figure 49, we obtain for the configuration $\mathcal{T}_\alpha^5$ the results represented in Figure 51. The accuracy of the localization is here similar to the one obtained from the configuration $\mathcal{T}_\alpha^4$.

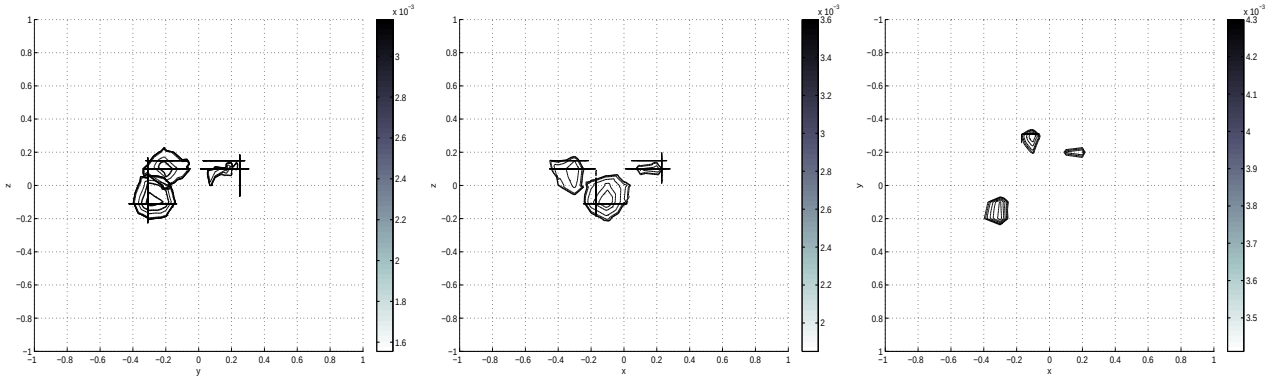

Figure 51: Contour-plot views respectively from the $x-$direction, the $y-$direction and the $z-$direction, based on the enriched sequence, deriving from one of the modules of the terms in (31). Here, $\mathcal{T}_\alpha^5$ is used, $\mu_j = 1$, $\varepsilon_j = 3$ $(1 \leq j \leq 3)$, $\tau = 2.47\,10^{-1}$, $\eta_{\max} = 10$, $n = 16$ and $\eta_\star = 4$.

We have also considered the localization in the electromagnetic case. Figure 52 shows the results obtained in this case and from the configuration $\mathcal{T}_\alpha^5$. Similar results have been obtained from experiments performed with other physical contrasts ($\mu_j = 5$, $\varepsilon_j = 3,5 + 0.1\mathrm{i}$ for example), by using $\mathcal{T}_\alpha^5$ and different frequencies.

The results of Figure 53 are obtained from $\mathcal{T}_\alpha^5$ by keeping the same physical contrast as in the experiment associated with Figure 51, but by using a higher frequency; it appears that the localization becomes now less accurate. In the same order of ideas, we have considered increasingly large values as well as very small values of the frequency in experiments and observed that the localization becomes highly inaccurate with such choices, as was the case for the procedure based on the MUSIC approach.

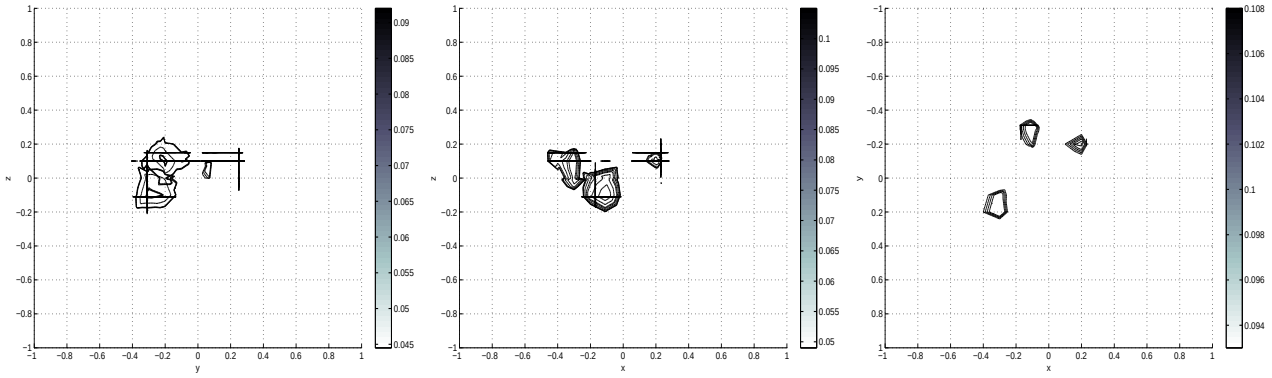

Figure 52: Contour-plot views respectively from the $x-$direction, the $y-$direction and the $z-$direction, based on the enriched sequence, deriving from one of the modules of the terms in (31). Here, $\mathcal{T}_{\alpha}^{5}$ is used, $\mu_j = 3$, $\varepsilon_j = 10$ $(1 \leq j \leq 3)$, $\tau = 2.09\,10^{-2}$, $\eta_{\max} = 10$, $n = 16$ and $\eta_{\star} = 4$.

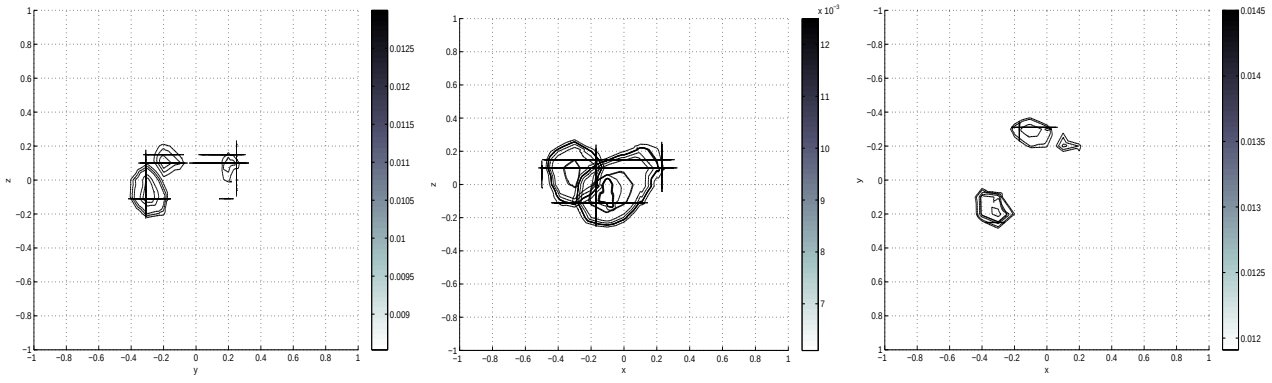

Figure 53: Contour-plot views respectively from the $x-$direction, the $y-$direction and the $z-$direction, based on the enriched sequence, deriving from one of the modules of the terms in (31). Here, $\mathcal{T}_{\alpha}^{5}$ is used, $\mu_j = 1$, $\varepsilon_j = 3$ $(1 \leq j \leq 3)$, $\tau = 6.27\,10^{-1}$, $\eta_{\max} = 10$, $n = 16$ and $\eta_{\star} = 3$.

An inspection of the results of Figures 46 - 53 shows that the localization from $\mathcal{T}_\alpha^3$, $\mathcal{T}_\alpha^4$ or $\mathcal{T}_\alpha^5$ is successfully achieved at frequencies which are not too high or too low. However, as before in the single imperfection case, the present procedure appears in the multiple imperfections case, with the choice made for $\eta_{\max}$, less efficient than the procedure based on the MUSIC approach. Of course, a large number of measurements is used here and moreover the obtained results (see Figures 46 - 53) are less accurate than those deriving from the MUSIC approach (see Figures 32 - 34, 37 - 38, 40 - 41).

To arrive at an accuracy similar to the one of the localization based on the MUSIC approach (or to the one based on the Current Projection method in the case of single imperfection), we must consider larger values for $\eta_{\max}$. However, too large a value of $\eta_{\max}$ will lead to a major disadvantage of the localization procedure: the exorbitant CPU time required by the localization. In fact, for too large a value of $\eta_{\max}$, we are concerned with a number of measurements which, despite the cutoff process of the Fourier domain, remains important. On the other hand, since the evaluation of each measurement, related to computations based on a full mesh of the domain, has a relatively important cost (average CPU time of about 21.637 s. on a "SGI Origin 3200" in the case of $\mathcal{T}_\alpha^5$ for example, without taking into account the CPU time for calculating the right-hand side of (19) associated with the measurement), it follows that the localization in such a case can only be achieved with an exorbitant CPU time. Even in the present situation, where too large a value of $\eta_{\max}$ has not been considered in experiments, this localization CPU time appears reasonable but remains expensive when compared with the one needed by the procedure based on the MUSIC approach (or on the Current Projection method in the single imperfection case) because of the important number of measurements.

It appears that the present procedure will be more helpful for simulations where each measurement is evaluated from integral equations techniques. In fact, such evaluations should allow us to achieve localizations with more reasonable CPU times; the full meshes of the domain Ω not being required.

In a same region of interest $[-K, K]^3$, we can consider the same number of measurements to locate, at a fixed order of resolution, the single imperfection ($m = 1$) as well as all the imperfections ($m > 1$) contained in this region. This has been the case for the settings defined from $\mathcal{T}_\alpha^1$, $\mathcal{T}_\alpha^2$ and $\mathcal{T}_\alpha^3$, associated with a same region of interest in the procedure. The CPU times taken by the procedure in these settings differ only in the step of evaluation of the measurements. Typically, the procedure appears more suitable for configurations with a large number of imperfections; unlike in the MUSIC approach, here, the number of measurements does not depend explicitly on m.

7 Conclusions and Perspectives

We have presented three procedures for the numerical localization of electromagnetic imperfections contained in a three-dimensional bounded domain. Each one of these procedures results from the combination of the asymptotic formula (17) with one of the following inversion algorithms: the Current Projection method, the MUSIC approach, and the inverse Fourier method. Extensive numerical simulations have been performed in different settings and the obtained results show the efficiency of the presented localization procedures. We also conclude that the procedure based on the MUSIC approach

appears well-suited for both the localization of a single imperfection and that of multiple imperfections. In the case of a single ball-shaped imperfection, electric or magnetic, the procedure based on the Current Projection method appears, for certain frequencies, more suitable for a full reconstruction (center and 'radius').

As observed, each one of the procedures requires a finite number of numerical boundary measurements, where each measurement, associated with a prescribed boundary electric current, is obtained by solving the discrete formulation (19) for this prescribed datum. The CPU time needed to solve (19) is relatively important in comparison with the time that could be required for solving the discrete "background" formulation in electric field. In fact, the usual triangulation process, applied here to Ω, generates a conforming mesh of Ω that takes into account the discretization of each imperfection and leads to an excessive number of degrees of freedom caused by the smallness of the imperfections — especially since this is a three-dimensional mesh and since mixed finite elements are considered. The discrete system resulting from (19) has then a very large number of unknowns and even by solving this system with an iterative preconditioned algorithm, as done here, the localization CPU time remains important. In the presence of a large number of imperfections, this localization CPU time should become quite expensive since the number of degrees of freedom resulting from the mesh of Ω as well as the number of needed numerical measurements (namely with the MUSIC approach) would be more important in that situation. In the presence of imperfections of smaller sizes than those considered here, the number of degrees of freedom associated with (19), deriving from a full conforming mesh of Ω, is simply exorbitant and forbids numerical investigations due to the excessive requirement of the memory storage in this case. Considering then a full conforming mesh of the domain when it contains multiple small imperfections leads to some drawbacks in numerical investigations as far as memory storage and CPU time are concerned. This has obliged us in particular to not consider slightly smaller or very small imperfections in the present work.

An immediate task should be the numerical localization of electromagnetic imperfections contained in a three-dimensional bounded domain, by making use of the localization procedures described here, where the stage of the numerical evaluation of boundary measurements will be achieved by integral equation techniques. In fact, we think that the use of integral equations in this stage will lead us to numerical localizations with much less memory storage and a greatly reduced CPU time, the full meshes of the domain not being required.

As a further perspective of the present work, it would be interesting to numerically study the localization of three-dimensional electromagnetic imperfections when these are not necessarily well-separated. This concerns the case where the bounded domain contains multiple imperfections and two of these are too close. Our present modeling does not consider this case, though it exists in practical applications.

A final perspective deals with the numerical localization of electromagnetic imperfections contained in a three-dimensional bounded domain, with at least one of these imperfections close to the boundary of the domain. This is also a case that can be found in practical applications and that has not been

treated in the present modeling.

Acknowledgements. The authors thank Professor H. Ammari for his comments and helpful suggestions throughout this work.

References

[1] H. Ammari, E. Iakovleva & D. Lesselier, "A MUSIC algorithm for locating small inclusions buried in a half-space from the scattering amplitude at a fixed frequency", *Multiscale Model. Simul.*, 3, (2005), 597–628.

[2] H. Ammari, E. Iakovleva, D. Lesselier & G. Perrusson, "MUSIC-type electromagnetic imaging of a collection of small three-dimensional bounded inclusions", *SIAM J. Sci. Comput.*, to appear.

[3] H. Ammari & H. Kang, *Reconstruction of small inhomogeneities from boundary measurements*, Lecture Notes in Mathematics, v. 1846, Springer-Verlag, Berlin, 2004.

[4] H. Ammari & A. Khelifi, "Electromagnetic scattering by small dielectric inhomogeneities", *J. Math. Pures Appl.*, 82, (2003), 749–842.

[5] H. Ammari, S. Moskow & M.S. Vogelius, "Boundary integral formulas for the reconstruction of electromagnetic imperfections of small diameter", *ESAIM Control Optim. Calc. Var.*, 9, (2003), 49–66.

[6] H. Ammari, M. Vogelius & D. Volkov, "Asymptotic formulas for perturbations in the electromagnetic fields due to the presence of imperfections of small diameter II. The full Maxwell equations", *J. Math. Pures Appl.*, 80, (2001), 769–814.

[7] H. Ammari & D. Volkov, "Asymptotic formulas for perturbations in the eigenfrequencies of the full Maxwell equations due to the presence of imperfections of small diameter", *Asymptot. Anal.*, 30, (2002), 331–350.

[8] M. Brühl & M. Hanke, "Numerical implementation of two noniterative methods for locating inclusions by impedance tomography", *Inverse Problems*, 16, (2000), 1029–1042.

[9] A.P. Calderón, "On an inverse boundary value problem", *Seminar on Numerical Analysis and its Applications to Continuum Physics, Soc. Brasileira de Matemática, Rio de Janeiro*, (1980), 65–73.

[10] D.J. Cedio-Fengya, S. Moskow and M.S. Vogelius, "Identification of conductivity imperfections of small diameter by boundary measurements. Continuous dependence and computational reconstruction", *Inverse Problems*, 14, (1998), 553–595.

[11] M. Cheney, "The Linear Sampling Method and the MUSIC Algorithm", *Inverse Problems*, 17, (2001), 591–595.

[12] D. Colton, J. Coyle & P. Monk, "Recent developments in inverse acoustic scattering theory", *SIAM Rev.*, 42, (2000), 369–414.

[13] D. Colton & R. Kress, *Integral equation methods in scattering theory*, Krieger Publ. Co., Malabar, Florida, 1992.

[14] D.C. Dobson & F. Santosa, "An image-enhancement technique for electrical impedance tomography", *Inverse Problems*, 10, (1994), 317–334.

[15] G.B. Folland, *Introduction to partial differential equations*, Princeton University Press, Princeton, 1976.

[16] E. Iakovleva, *Diffraction inverse par des petites inclusions*, Ph.D. Thesis, Ecole Polytechnique, Palaiseau, France, 2004.

[17] R.V. Kohn & A. McKenny, "Numerical implementation of a variational method for electrical impedance tomography", *Inverse Problems*, 6, (1990), 389–414.

[18] J. Laminie & S.M. Mefire, "Three-dimensional computation of a magnetic field by mixed finite elements and boundary elements", *Appl. Numer. Math.*, 35, (2000), 221–244.

[19] T.D. Mast, A. Nachman & R.C. Waag, "Focusing and imaging using eigenfunctions of the scattering operator", *J. Acoust. Soc. Am.*, 102, (1997), 715–725.

[20] J.-C. Nédélec, "Mixed finite elements in $\mathbb{R}^3$", *Numer. Math.*, 35, (1980), 315–341.

[21] F. Santosa & M.S. Vogelius, "A backprojection algorithm for electrical impedance imaging", *SIAM J. Appl. Math.*, 50, (1990), 216–243.

[22] E. Somersalo, M. Cheney, D. Isaacson & E. Isaacson, "Layer-stripping: a direct numerical method for impedance imaging", *Inverse Problems*, 7, (1991), 899–926.

[23] C.W. Therrien, *Discrete Random Signals and Statistical Signal Processing*, Englewood Cliffs, Prentice-Hall, NJ, 1992.

[24] D. Volkov, "Numerical methods for locating small dielectric inhomogeneities", *Wave Motion*, 38, (2003), 189–206.